Laser-Based Angle-Resolved Photoemission Spectroscopy of Topological Insulators

Citation

Wang, Yihua. 2012. Laser-Based Angle-Resolved Photoemission Spectroscopy of Topological Insulators. Doctoral dissertation, Harvard University.

Advisor: Prof. Nuh Gedik Yihua Wang

Laser-based Angle-resolved Photoemission Spectroscopy of Topological Insulators

Abstract

Topological insulators (TI) are a new phase of matter with very exotic electronic properties on their surface. As a direct consequence of the topological order, the surface electrons of TI form bands that cross the Fermi surface odd number of times and are guaranteed to be metallic. They also have a linear energy-momentum dispersion relationship that satisfies the Dirac equation and are therefore called Dirac fermions. The surface Dirac fermions of TI are spin-polarized with the direction of the spin locked to momentum and are immune from certain scatterings. These unique properties of surface electrons provide a platform for utilizing TI in future spin-based electronics and quantum computation.

The surface bands of 3D TI can be directly mapped by angle-resolved photoemission spectroscopy (ARPES) and the spin polarization can be determined by spin-resolved ARPES. These types of experiments are the first to establish the 3D topological order, which demonstrates the power of ARPES in probing the surface of strongly spin-orbit coupled materials. Extensive investigation of TI has ranged from understanding the fundamental electronic and lattice structure of various TI compounds to building TI-based devices in search of more exotic particles such as Majorana fermions and magnetic monopoles. Surface-sensitive techniques that can efficiently disentangle the charge and spin degrees of freedom have been crucially important in tackling the multi-faceted problems of TI.

In this thesis, I show that laser-based ARPES in combination with a time-of-flight spectrometer is a powerful tool to study the spin structure and charge dynamics of the Dirac fermions on the surface of

TI. Chapter 1 gives a brief introduction of TI. Chapter 2 describes the basic principles behind ARPES and time-resolved ARPES (TrARPES). Chapter 3 provides a detailed account of the experimental setup to perform laser-based ARPES and TrARPES. In Chapters 4 and 5, how these two techniques are effectively applied to investigate two unique electronic properties of TI is elaborated. Through these studies, I have obtained a complete mapping of the spin texture of several prototypical topological insulators and have uncovered the cooling mechanism governing the hot surface Dirac fermions.

Contents

Acknowledgement

This thesis would not have been possible without the help from many wonderful people I am fortunate enough to be surrounded by. First of all, I would like to thank my advisor Prof. Nuh Gedik at MIT. He took me as his first graduate student when I was three years into my study and has supported me since in every way he can. His trust and patience in me have guided me through all the challenging and exciting projects I have embarked on. I have enjoyed working with all the members of the Gedik group including Dr. Darius Torchinsky, Dr. David Hsieh, graduate students Dan Pilon, James McIver, Alex Frenzel, Fahad Mahmood, Edbert Sie and Changmin Lee, and undergraduate student Gus Downs. I am especially indebted to David because he is the first person to teach me about topological insulators and his sharp vision on almost every topic has given me lots of inspirations to carry on the research in this and related fields. I have also benefitted from the collaboration with other groups at MIT. Most notably, Prof. Young Lee's group and Prof. Pablo Jarillo-Herrero's group have both provided me with high quality samples. And I have also learned a lot from the frequent discussions with Prof. Liang Fu.

Everyone who has been through graduate school knows that it is a grueling process. But luckily I have made some valuable friends during my seven years of life here in Boston. They have made these years endurable, memorable and even enjoyable. Among them are my best friends Ou Chen and John Fei, whose mix of batter and encouragement keep me both grounded and afloat.

At last, I want to thank my parents Deqiang Wang and Qinpin Liu. Even though they did not teach me much physics, they have taught me a more important thing which is the right attitude to overcome any challenge throughout my life. Their unconditional love is what has been driving me through the ups-and-downs of my Phd. I regret not being able to be around them for such a long period of time. But I am constantly motivated by knowing that what I am doing makes them proud.

List of figures

Chapter 1

Introduction to topological insulators

1.1 Quantum Hall state and topological order

In Landau's paradigm, ordered phases are defined by broken symmetry. For example, crystalline order with a periodic lattice structure breaks continuous translational and rotational symmetry of space; in magnets, time-reversal symmetry is broken together with some rotational symmetry.

There is a completely different way of defining order which is through topology [8-9]. It is first exemplified by the quantum hall state that was discovered in the 1980s [10]. Consider non-interacting electron gas confined in two dimensions (2DEG) under a strong magnetic field as shown in Figure 1.1(a). The electrons in the 2DEG undergo cyclotron motion and therefore are insulating. However, the electrons at the edge of the 2DEG can skip along the edge and conduct. These metallic edge states are insensitive to disorder because of the absence of states for back scattering. The conductivity σ_{xy} of the edge is found to be very robustly quantized [10]:

$$\sigma_{xy} = n\frac{e^2}{h}$$

where *n* is an integer. Thouless, Kohmoto, Nightingale and den Nijs(TKNN) explained this in terms of the topology of the wavefunction [8], which is characterized by the phase factor of the wavefunction after it propagates through a closed path. This phase is an invariant under adiabatic change of the Hamiltonian for the wavefunction and it is called Berry's phase [11], which is equal to *n*.

In the picture of the quantum Hall state [Figure 1.1(a)], the wavefunction of the cyclotron motion of the 2DEG and the free electron wavefunction in the vacuum have different Berry's phases and therefore are topologically different. In the momentum space, the insulating 2DEG forms Landau levels with an energy gap of cyclotron frequency [Figure 1.1(b)]. When the wavefunction goes from 2DEG to the vacuum through its edge, somewhere along the way the band gap has to be closed in order for the topological invariant to change. This results in the linear dispersion of the edge states that cross the Fermi level. As later shown by Hatsugai, the edge states have a topological invariant of their own which is equal to the TKNN invariant of the bulk 2DEG.

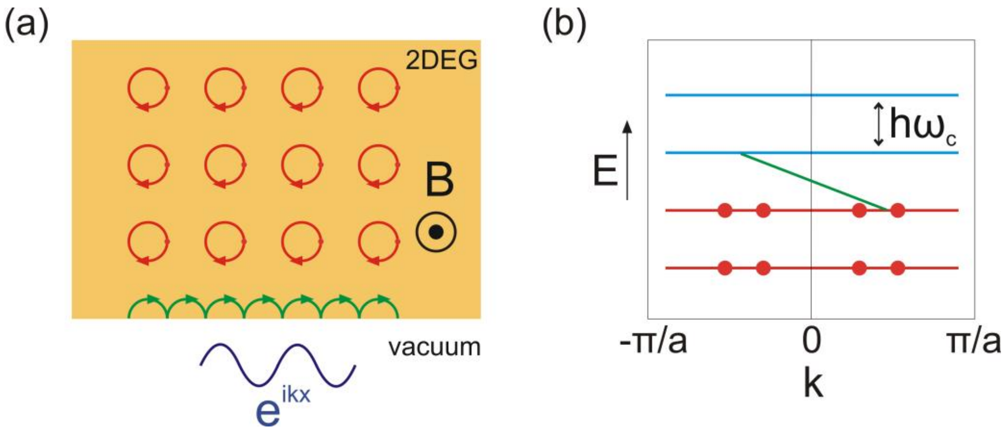

Figure 1.1 Quantum Hall state. (a) A two-dimensional electron gas (2DEG) under strong magnetic field is an insulating state. Its interface (edge) with vacuum or any other topologically trivial insulator is metallic because the skipping motion of the electrons along the edge can conduct current. (b) The insulating states (red) of the 2DEG form Landau levels while its edge states (green) cross the Fermi

1.2 Quantum spin Hall insulator and topological insulator

The above discussion of Quantum Hall state is only possible for a two-dimensional system under a magnetic field. Haldane showed that it is possible to realize a Quantum Hall insulator in electrons moving in a three dimensional lattice by applying a magnetic field that is zero on average but has a full lattice symmetry [12]. Recent developments that lead to the discovery of quantum spin Hall insulator (i.e., topological insulator) is based on Haldane's idea but utilizes the more realistic spin-orbit coupling instead of the periodic magnetic field. Spin-orbit coupling is a relativistic effect between the electron spin and its orbital motion. It lifts the spin degeneracy at a general crystal momentum *k* and favors the propagation of spin-up electrons along the edge [Figure 1.2(a) magenta]. Because of the time-reversal symmetry, which is conserved without a magnetic field, there is also a spin-down state propagating towards -*k*. Each spin polarized edge state carries charge conductivity $\sigma_{xy} = \frac{e^2}{2h}$ and the number of spin-up states is a TKNN invariant $n_\uparrow$. The TKNN invariant for spin-down states bears a negative sign as

$$n_\downarrow = -n_\uparrow$$

The total charge conductivity is given by:

$$\sigma_{xy} = (n_\downarrow + n_\uparrow)\frac{e^2}{2h} = 0$$

This is dictated by symmetry because the Hall conductivity is odd under time reversal, which is not broken by the spin-orbit coupling.

Even though the total charge conductivity of a quantum spin Hall insulator is zero, the total spin conductivity does not cancel. They add up to be:

$$\sigma_{xy}^s = (n_\downarrow - n_\uparrow)\frac{e}{4\pi}$$

It was conceivable to use the spin TKNN invariant $(n_\downarrow - n_\uparrow)$ as the topological invariant to characterize a spin Hall insulator. However, as pointed out by Kane and Mele [13], $(n_\downarrow - n_\uparrow)$ is invariant only when σ_z is conserved. This tends to break down in a real system due to the presence of interband mixing, disorder or interaction.

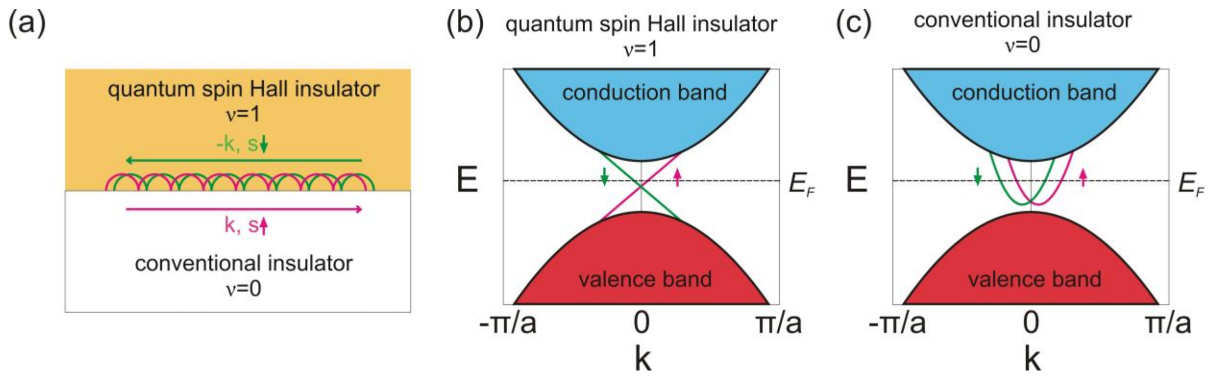

Figure 1.2 A quantum spin Hall insulator appears with spin-orbit coupling. (a) The interface between a conventional and quantum spin Hall insulator has edge states that propagate in the opposite direction and with opposite spin. In the momentum space (b) and (c), these states at the boundary are mirror image of each other about the time-reversal invariant momentum $k = 0$. For a quantum spin Hall insulator (b), the edge states enclose $k = 0$ once and cross the Fermi level with linear

Kane and Mele propose to use Z_2 invariant υ to characterize a quantum spin Hall insulator [13-14]. It is determined by if it is even ($\upsilon = 0$) or odd $\upsilon = 1$ number of times a time-reversal invariant momentum is enclosed by edge states Figure 1.2(b) and (c). It can be seen from Figure 1.2 that a continuous deformation of the conduction or valence band or any shift of the Fermi level will not change υ, which is a manifestation of its topological nature.

The gapless nature of the edge states is protected by time-reversal symmetry and is a signature of a quantum spin Hall insulator. Because any back scattering of state $(\boldsymbol{k}, \uparrow)$ is only allowed by time-reversal symmetry to enter the final state $(-\boldsymbol{k}, \downarrow)$, which is occupied, weak disorder will not localize electrons and the spin transport will be dissipationless.

The direct observation of quantum spin Hall states is facilitated by the generalization of Z_2 topological order to three-dimension [15-17]. This is because probing the surface states of a 3D topological insulator, as quantum spin Hall insulator is called in 3D, is experimentally more feasible than probing the edge states of the quantum spin Hall edge states because scattering probes can be utilized. Although an ingenious proposal by Bernevig *et al.* [18] has subsequently led to the observation of quantized charge conductance in a HgTe/(Hg,Cd)Te quantum well without applying a magnetic field [19], transport measurements cannot detect a single edge state in a spin-resolved manner. For scattering probes, the atomic spatial extension of the edge states wavefunction is too small for the micron level spot size. However, many scattering probes are very sensitive to surface states and the task of directly measuring the dispersion of surface states is made possible through angle-resolved photoemission spectroscopy (ARPES) [20]. The energy-momentum resolution combined with its surface sensitivity has led to the direct observation of the metallic surface states with linear energy-momentum dispersion in many materials including $Bi_{1-x}Sb_x$, Bi_2Te_3 and Bi_2Se_3 [21-25]. At the meantime, the topological invariant is directly identified by counting the surface states crossing the Fermi level [21]. Later using spin-resolved ARPES, Hsieh *et al.* has shown that the spin polarization of the surface states is locked to its momentum in a manner required by time-reversal symmetry [26] .

Chapter 2

Theoretical background for ARPES and TrARPES

2.1 ARPES

2.1.1 Basic principles

Photoemission spectroscopy is a photon-in electron-out type of experiment. It bases on a very simple physical phenomenon of solids: the photoelectric effect. Light with enough photon energy impinging on the surface of a material can liberate electrons from it. These free electrons are collected by an analyzer which then determines the kinetic energy E_{kin} of the electrons. Knowing the photon energy $h\nu$, the binding energy E_B of the electron is determined by the following equation:

$$E_{kin} = h\nu - \Phi - |E_B|$$

where Φ is the work function, which is the amount of energy needed for the electrons at the Fermi level to overcome the attractive potential of the material to become free electrons. The work function can be independently measured with other experimental techniques such as thermionic emission and is typically around 4.3 eV for metals.

Angle-resolved photoemission spectroscopy goes one step further to measure the outcoming angles of the photoelectrons as well as their kinetic energies. As illustrated in Fig. 2.2, after the determination of E_{kin} and the polar angle ϑ, the electron momentum parallel to the crystal surface $K_{//}$ can be known through the following equation:

$$K_{//} = \sqrt{\frac{2mE_{kin}}{\hbar^2}} \sin\vartheta$$

where m is the free electron mass and $\hbar$ is the Planck's constant. The coefficient $\sqrt{\frac{2m}{\hbar^2}} = 0.512\text{Å}^{-1}(eV)^{-1/2}$. The *x* and *y* components of the in-plane momentum can be easily obtained by knowing the azimuthal angle φ. Because the photoemission process does not break the translational symmetry along the crystal surface, in-plane momentum is conserved during the process. Therefore, the measured in-plane momentum of the free electrons in the vacuum $K_{//}$ is the same as the in-plane crystal momentum $k_{//}$ in the solid.

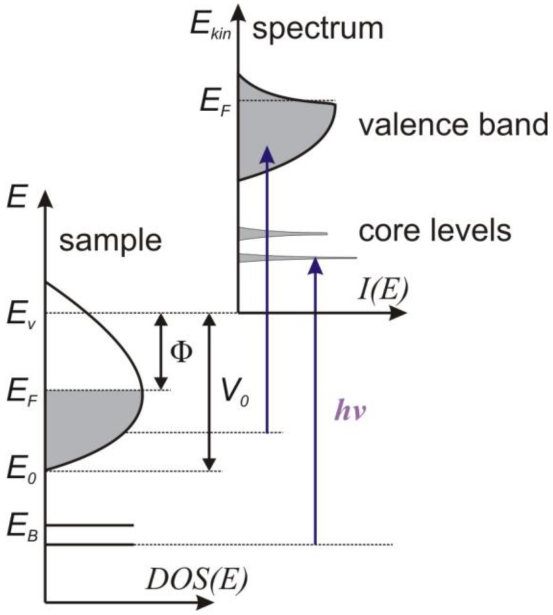

Figure 2.1 Energy diagram showing the bands inside a solid and its relation to the kinetic energy of photoelectrons.

The momentum perpendicular to the surface is not conserved during photoemission because the translational symmetry is broken across the surface in the process. We have the following equation for the perpendicular (*z*) component of the free electron K_z

$$K_z = \sqrt{\frac{2mE_k}{\hbar^2}}\cos\vartheta$$

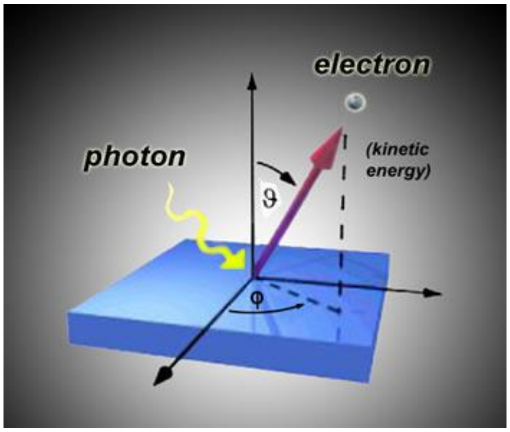

Figure 2.2 Schematics of the outcoming angle of photoelectrons with certain energy.

In general, how K_z relates to the out-of-plane crystal momentum k_z is quite complex and requires complementary experimental data. However, we can derive a much simpler relation by using a three-step model of the photoemission process. In this model, we assume that the final states of the photoemission process are nearly free-electron states on the same band as the valence band, as shown in Figure 2.3 in an extended zone scheme. The parabolic dispersion relation of electrons gives

$$\frac{(\hbar k)^2}{2m} = \frac{(\hbar k_{//})^2 + (\hbar k_z)^2}{2m} = E_f + |E_0|$$

where k is electron's total crystal momentum and the band bottom E_0 and the final state energy E_f are referenced to the Fermi level E_F. We can also see from Fig. 2.3(b) that

$$E_f = E_{kin} + \Phi$$

Defining the inner potential

$$V_o \equiv |E_0| + \Phi$$

We get

$$k_z = \sqrt{\frac{2m(E_k \cos\vartheta^2 + V_0)}{\hbar^2}}$$

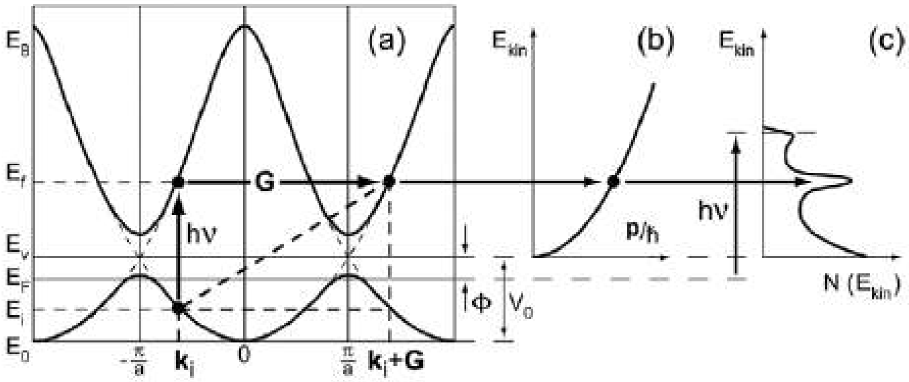

Figure 2.3 Three-step model of a photoemission process. Adapted from [5].

The most common way of determining V_0 and hence obtaining k_z in an ARPES experiment is by finding the periodicity of the dispersion $E(k_z)$. This is realized by detecting photoelectrons at surface normal so that $k_{//} = 0$ while varying the photo energy. In reduced dimensions, for example at the surface of a crystal, $E(k_z)$ is a constant and there will be no change in the energy of normally emitted electrons when photon energy is varied. This is particularly relevant for topological insulators in distinguishing surface states from the bulk bands.

In summary, the measured free electron kinetic energy and the angles are related to the crystal momentum in the following way:

$$k_x = \sqrt{\frac{2mE_k}{\hbar^2}} \sin\vartheta \cos\varphi$$

$$k_y = \sqrt{\frac{2mE_k}{\hbar^2}} \sin\vartheta \sin\varphi$$

$$k_z = \sqrt{\frac{2m(E_k \cos\vartheta^2 + V_0)}{\hbar^2}}$$

2.1.2 Spin-resolved ARPES with hemispherical analyzers

The working principle behind an electron energy analyzer involves converting energy and angle into spatial information so that they can be imaged by a position sensitive detector. The most popular type of electron energy analyzer is what is called a hemispherical analyzer, as shown in Figure 2.4(a). The entrance slit selects out electrons with a certain azimuthal angle. The electrons coming in with different angles along the slit are then projected as different momentum k onto the camera. Electrons with different energies are separated along the radial direction of the spheres as they traverse through the vacuum space between the two concentric spheres, which have a voltage difference appropriate for the kinetic energy of the electrons. As a result, the energy is resolved by the other dimension of the camera. To obtain a complete mapping of the in-plane momentum, typically the samples are continuously rotated relative to the detector for a scan.

When the spin polarization needs to be analyzed, electrons with certain energy and momentum are passed through a small hole next to the camera and enter what is called a Mott polarimeter [Figure 2.4(b)]. These electrons are then accelerated to high energy to bombard a gold foil (shown as yellow in Figure 2.4(b)). Based on a process known as Mott scattering, electrons with opposite spin polarization have different probabilities of scattering into the two detectors located in the opposite side. If more than one dimension of spin needs to be analyzed, more stages of Mott polarimeter can be installed. Such spin-resolved ARPES experiments have played an instrumental role in experimentally establishing the spin-momentum locking of topological insulators [22].

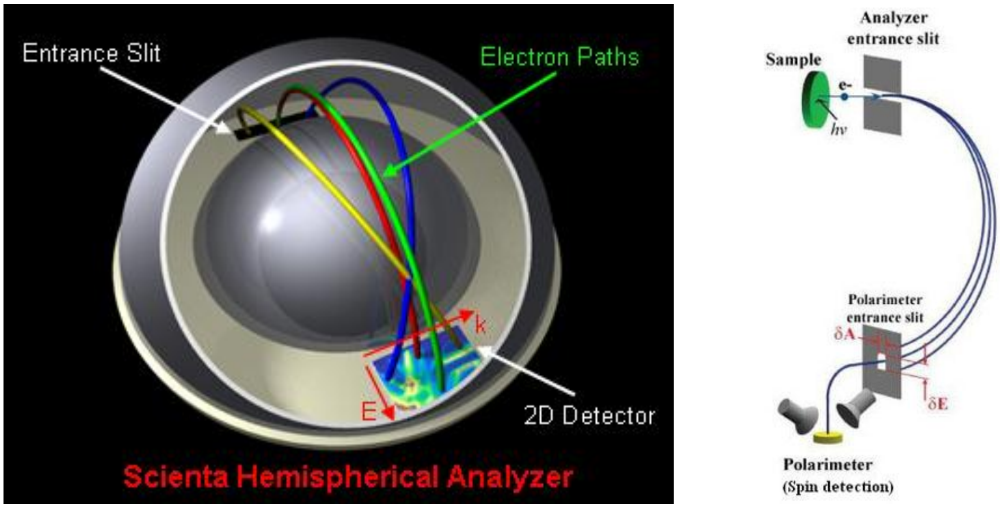

Figure 2.4 Left: A typical hemispherical electron energy analyzer. Electrons with different energies are separated by the voltage difference between the two hemispheres and the momenta of the electrons are mapped onto the other dimension of the 2D detector. Right panel shows a spin-resolved ARPES setup. Electrons with certain energy and momentum filtered by the hemispheres enter a hole and impinge on a gold foil with high energy. Electrons with different spins are scattered into different directions. Adapted from Z.-X. Shen lab website.

ARPES experiments are generally performed at large synchrotron radiation facilities around the world. The large photon energy tunability and high photon flux are instrumental in leading to many discoveries in condensed matter physics in recent years, including the discoveries of topological insulators. Alternatively, He lamp with photon energies of 21.2 eV is used. The new generation of He lamp can achieve sub meV bandwidth and sub mm spot size. Such light in the soft x-ray region is generated from the discharge of He gas with 10^{-6} Torr pressure, which has to be differentially pumped to maintain a UHV pressure in the measurement chamber.

2.2 Time-resolved ARPES

Time-resolved photoemission technique was first introduced in the 1980s to study the electron thermalization in metals [27-33]. In recent years, laser-based ARPES has developed quickly with the advancement in ultrafast lasers with femtosecond pulse width and multiple milijoules pulse energy and high resolution APRES apparatus [34-35]. Ultrafast laser based source further allows time-resolved ARPES experiments to study the dynamics of electronic, lattice and magnetic order in many strongly correlated electron systems [1, 36-42], carbon based novel materials [43-45] and many physical and chemical phenomena at metal surface and interfaces [46-50].

Time-resolved ARPES is performed based on the pump-probe scheme widely employed in the study of ultrafast dynamics. Under this scheme, a laser pulse is typically split into two parts. The pump part of the laser is used to excite the sample. As shown in Figure 2.5, the electrons undergo an optical transition into the empty states above the Fermi level. The probe part is in the ultraviolet frequency range so that it has enough energy to overcome the work function for photoemission. The UV pulse impinges the sample at certain time delay *t* after the excitation from the pump pulse and the photoemitted electrons are collected by an ARPES spectrometer to map out its entire spectrum both above and below the Fermi level. By continuously acquiring the APRES spectra at various *t*, we obtain an evolution of the energy-momentum resolved band structure and its occupation induced by the photoexcitation.

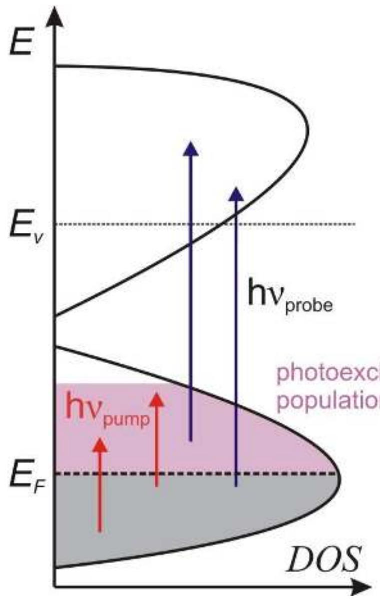

Figure 2.5 A time-resolved ARPES energy diagram. Infrared photons (red) moves electron population from the states below the Fermi level to occupy states above E_F. Upon the illumination of UV photons that arrive at certain delay from the pump pulse, all the states that have electron occupation undergo photoemission and are thus detected.

TrARPES is a powerful tool for the study of strongly correlated system because of its capability to disentangle the electronic, lattice and spin degrees of freedom [Figure 2.6]. Such capability roots in its simultaneous detection of electron's energy and momentum in a time-resolved way.

For the electronic system, the interaction can be learned from the thermalization process after photoexcitation as shown in Figure 2.7. The direct optical transition at $t = 0$ disrupts the thermal equilibruim and destroys the Fermi distribution of electrons. The electrons out of equilibruim inelastically scatter among themselves to return to a thermalized distribution. Using TrARPES, a distribution function as a function of t can be obtained from the intensity spectra [20]. By studying the evolution of the distribution function, electron-electron interaction can be inferred [27-29, 32-33, 43, 45, 51].

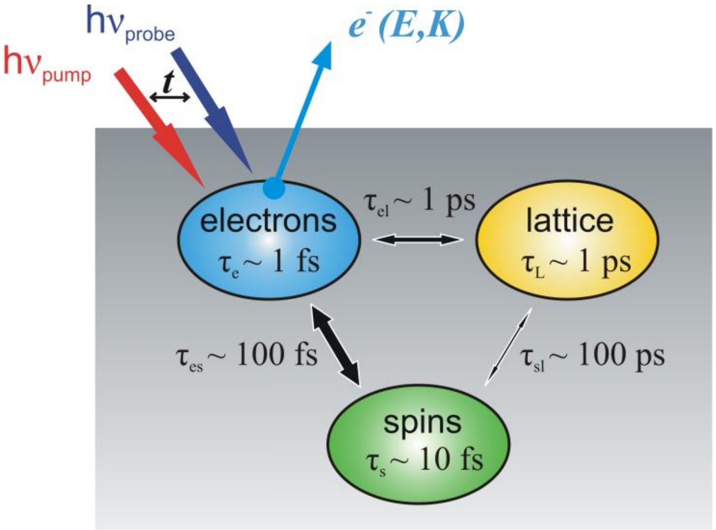

Figure 2.6 Coupling between the electron, spin and lattice degrees of freedom after an ultrafast laser excitation. The typical thermalization time scale is labelled inside the ellipse representing each subsystem. The magnitude of coupling between the subsystems are represented by the width of the arrow. Both the pump and probe pulses couple to the electronic degree of freedom.

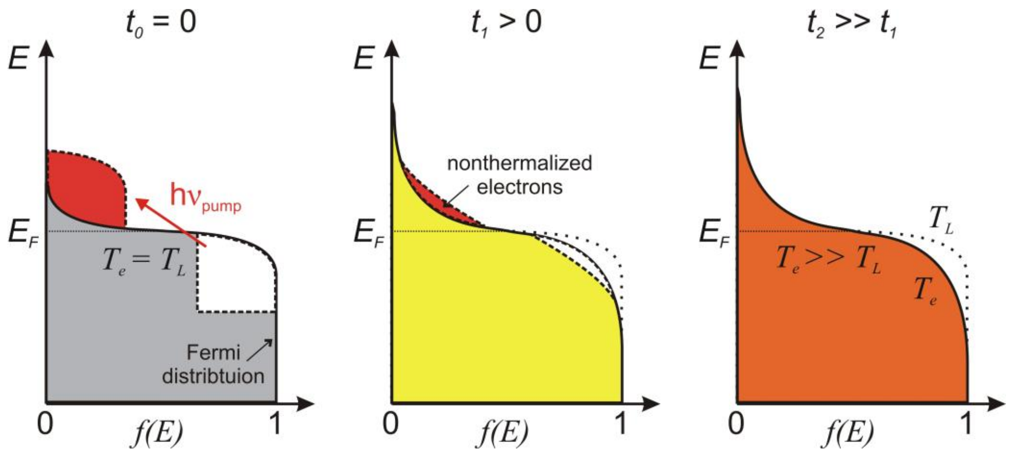

Figure 2.7 Ultrafast thermalization of electrons after photoexcitation. The electrons and lattice are under thermal equilibrium before the photoexcitation. The electrons have a Fermi distribution. At the momentum the pump laser pulse is absorbed by the electron system ($t = 0$), it removes the electrons with energies between the Fermi level and $h\nu_{\text{pump}}$ below. This makes a notch in the Fermi distribution and adds a block of electrons to above E_F. The electrons out of thermal equilibrium inelasticaly scatter and the distribution function relaxes towards a Fermi distribution ($t_1 > 0$). After a longer time t_2, the electrons are under thermal equilibrium among themselves and the distribution returns to a Fermi function with a much higher electronic temperature than the lattice.

Even though TrARPES only directly probes the electronic structure of the sample, the interaction between electrons and phonons causes change in electrons relaxation and therefore allows TrARPES to learn important information about the lattice as well. As shown in Figure 2.8, the electron system of a solid material first absorbs the light under radiation, electron-phonon coupling gives rise to excitation of the lattice degree of freedom. The excitation of phonons transfers energy from electrons to phonons and reduces the electronic temperature while raising phonons' until the electrons and phonons reach a quasi-thermal equilibrium. The electronic temperature $T_e(t)$ and lattice temperature $T_L(t)$ as a function of *t* can be described by the two-temperature model, which are two coupled differential equations [1, 52]. The coupling time constant gives us important information about the electron-phonon interaction. There are many variants of the two-temperature model used to describe different systems under photoexcitation. They typically consider a subsystem of phonons that strongly couple to and quickly remove energy from the electrons while this subsystem of phonons is simultaneously cooled by the entire lattice system. This involves describing the temperature dynamics of three coupled systems and is referred to as three-temperature model. The sensitivity of TrARPES to electron-phonon coupling is especially important for understanding the pairing mechanisms of high temperature superconductors [1, 38-39, 41-42, 52].

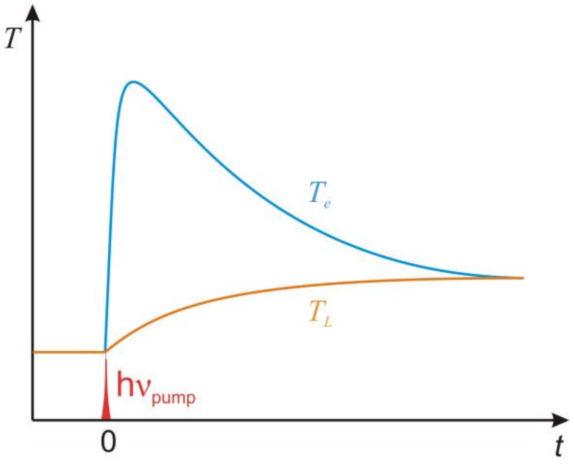

Figure 2.8 Ultrafast electron cooling by the lattice. The electronic temperature $\mathbf{T_e(t)}$ and lattice temperature $\mathbf{T_L(t)}$ as a function of t can be described by the two-temperature model. The heat deposited in the electron system transfers to the lattice through electron-phonon coupling, causing the electrons to cool and lattice temperature to increase. The big heat capacity of the lattice comparing with the electrons makes the lattice heating much smaller than that of the electrons.

There are many nonthermal processes that can be induced by photoexcitation. These processes are the results of the quantum mechanical nature of light-matter interaction and they have led to the observation of many unconventional photoinduced phenomena including metal-insulator transition [53], magnetic order [54-55] and superconductivity [56-57]. It has also been proposed that topological order can be induced from a trivial band insulator under circularly polarized light [58-60]. TrARPES provides the perfect opportunity to study these exciting laser induced phenomena in solid state systems.

Chapter 3

Experimental setup

3.1 Overview

We combine a Ti:Sapphire laser with an ARTOF for both static and time-resolved ARPES experiments. Fig. 3.1 shows the optical diagram of our laser-based TOF-ARPES setup. It has three major components: the laser source; the optics for generating UV and scanning time-delay; and a UHV chamber where the experiments are performed.

For the laser system, we use a Wyvern 500 regenerative amplifier from KMLabs. It features tunable repetition rate from 10 kHz to 200 kHz. The low repetition rate end (<50 kHz) has pulse energy > 250 uJ, which provides enough energy to pump an OPA, whereas the high repetition rate end has about 30 uJ, which is typically enough for time-resolved ARPES experiments. The details about the laser system will be described in Section 3.2.

To be able to continuously adjust the power in the pump and probe arm, we pass it through a half-waveplate and a thin film polarizer. The thin film polarizer passes horizontal polarization and reflects vertical polarization. The angle of the waveplate determines the ratio of the two orthogonal polarizations and thus distributes the transmission and reflection power.

The transmitted light from the thin film polarizer serves as the probe arm. It enters the Third Harmonic Generator (THG) and then Fourth Harmonic Generator (FHG) to produce 6 eV light suitable for ARPES. Our setup and the nonlinear physics involved will be described in Section 3.3. 6 eV light is then compressed by a pair of prisms, elevated by a periscope and focused into the ultra-high-vacuum (UHV) chamber onto the sample. The UHV system is described in Section 3.4.

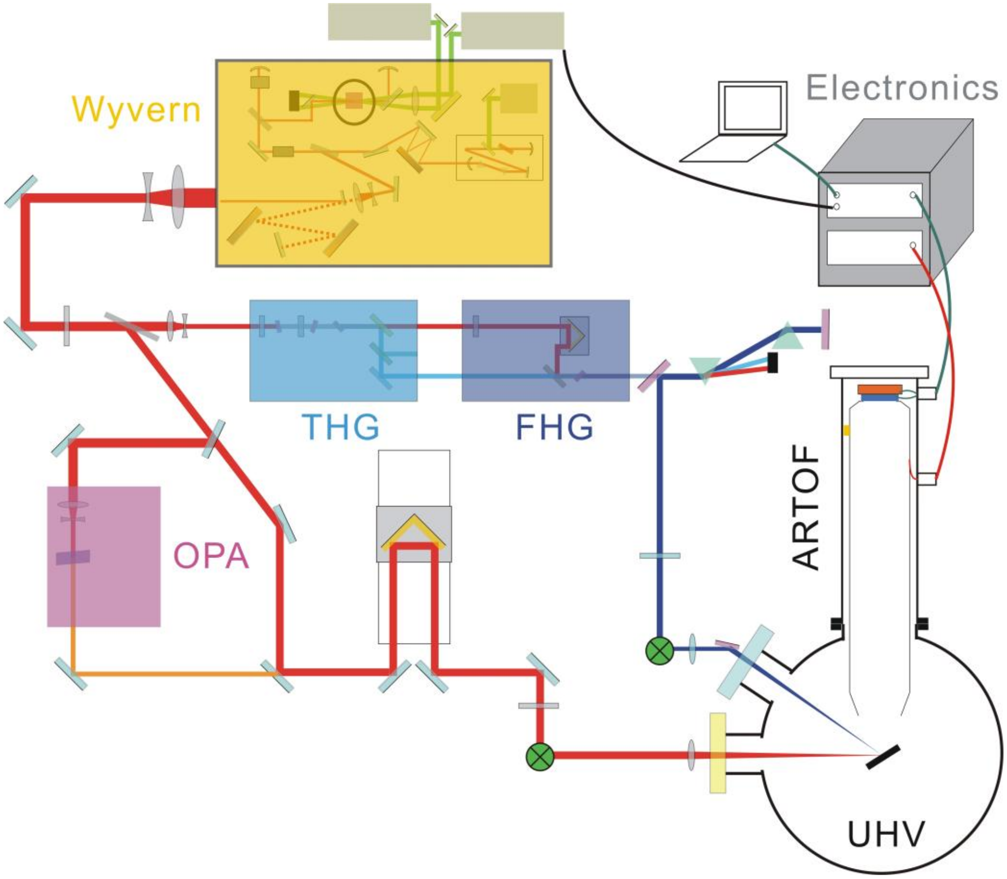

Figure 3.1 Schematics of the experimental setup for laser-based time-resolved ARPES with a time-of-flight electron spectrometer. See the text for the meaning of the acronyms.

The reflected light from the thin film polarizer serves as the pump arm. It either directly enters a delay stage or can be routed by a mirror on a flip mount into an Optical Parametric Amplifier (OPA) if wavelength other than 800 nm is needed for exciting the sample. The beam after the delay stage is attenuated by a neutral density filter and its polarization can be varied by a half waveplate. It is then elevated and focused onto the sample to be overlapped with the 6 eV focus spot.

Photoelectrons are collected by the angle-resolved time-of-flight (ARTOF) spectrometer, which will be elaborated in Section 3.5. The signals are read out by the electronics rack and then sent to the computer for analysis. A master clock in Wyvern generates the TTL signal to trigger the laser and synchronize the ARTOF.

3.2 Ultrafast laser for TrARPES

3.2.1 Generation of ultrashort laser pulses

The short laser pulses are generated from a continuous wave (CW) laser through a technique called mode-locking. As shown in Figure 3.2, such mode-locking is achieved in an oscillator. In the optical cavity defined by two end-mirrors, the allowed modes are those that form standing waves in the cavity with frequency separation equal to the inverse of the round-trip time of these modes in the cavity. The number of modes are determined by the bandwidth of the gain medium, which is the Ti:Sapphire crystal. Without mode-locking, the phases between different modes are random and therefore the total intensity of these modes is a constant after all the interference effects cancel out. An acoustic-optic modulator shakes the prism at a frequency equal to the round-trip time of these modes so that different modes are at the same phase in the cavity. This makes the peak of these oscillations constructively interfere and leads to a pulse in time.

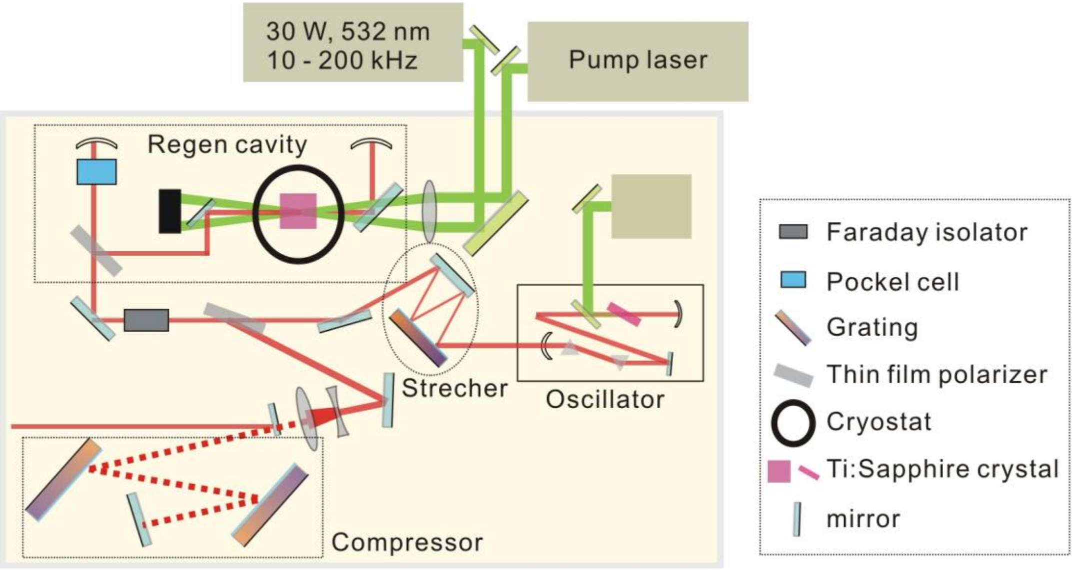

Figure 3.2 Regenerative amplifier optical diagram. The oscillator generates ultrafast laser pulses with 50 fs pulse width by mode-locking. These short pulses are sent to the stretcher to chirp the pulse to a longer pulse width. These broadened ‘seed’ pulses enter the regen cavity for amplification. The pump lasers (532 nm center wavelength) excites the Ti:Sapphire crystal and creates population inversion. The seed photons induce stimulated emission of identical photons as they go through the crystal and the amplification is achieved. The Pockel cell rotates the polarization of amplified pulses and couple them out of the cavity through a thin film polarizer. Another thin film polarizer prevents the amplified pulse from feeding back to the stretcher and instead deflects it to the compressor, where a pair of gratings compresses the pulse with to 50 fs.

We use a regenerative amplifier (KMLabs Wyvern 500) as the laser source for our ARPES and TrARPES experiments. The higher pulse energy (> 50 uJ) from the amplifier allows us to study the dynamics of phase transitions in many strongly correlated materials. The ultrafast laser pulses in a pulse train with 50 fs pulse width and 80 MHz repetition rate generated by the oscillator are sent to the stretcher to chirp the pulse to a longer pulse width. These broadened ‘seed’ pulses enter the regen cavity for amplification [Figure 3.2]. The reduced peak energy in a broadened pulse avoids damaging to the gain medium. The pump lasers (532 nm center wavelength) excites the Ti:Sapphire crystal and creates population inversion at a variable repetition rate adjustable from 10 kHz to 200 kHz. Low repetition rate provides a higher energy per pulse but high repetition rate provides better signal to noise in our TOF-based ARPES experiments, as will be discussed in Section 3.4. The seed photons induce stimulated emission of identical photons as they go through the crystal. As these photons travel back and forth in the cavity, it causes an avalanche effect and the amplification is achieved. The Pockel cell [Figure 3.2] is an electric-optic modulator that rotates the polarization of amplified pulses and couples them out of the cavity through a thin film polarizer. Such optical effect can be activated through a high voltage pulse with nano-second duration shorter than the period between pulses so that pulses that have gone through the right amount of round trips are coupled out of the cavity. Another thin film polarizer outside the cavity prevents the amplified pulse from feeding back to the stretcher and instead deflects it to the compressor, where a pair of gratings compresses the pulse width to 50 fs.

3.2.2 Relationship between pulse duration and spectral width

It can be shown that the pulse duration Δt and frequency width $\Delta \upsilon$ product has a minimum defined by

$$\Delta t \Delta \upsilon \geq 0.44$$

for a pulse with a Gaussian time-intensity profile. Knowing that the speed of light c, frequency υ and the wavelength λ of an electromagnetic wave is related by:

$$\lambda = \frac{c}{\nu}$$

By differentiating both sides and substituting for c, we get

$$\left|\frac{\Delta\lambda}{\lambda}\right| = \frac{\Delta\nu}{\nu}$$

Therefore we have the following relation for the time width and the spectral width:

$$\Delta t \Delta\lambda \geq 0.44 \frac{\lambda^2}{c}$$

Using $c \approx 300 nm/fs$, we can easily find the transform limited bandwidth for a 60 fs pulse at 800 nm is 15.6 nm.

3.2.3 Ultrafast pulse characterization

The spectrum of an ultrafast light pulse is measured by separating different frequencies spatially using a prism or a grating as shown in Figure 3.3.

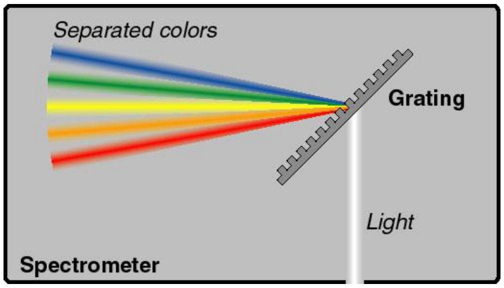

Figure 3.3 A grating spectrometer. An input light (white) diffracts off the grating and different wavelength are spatially separated and imaged onto a position-sensitive detector.

Because the response of electronics is typically more than hundreds of picoseconds long, the pulse duration of a femtosecond laser cannot be measured by a photodiode. The method of 'streaking' in measuring a femtosecond electron pulse by deflecting the electrons with a radiofrequency pulse does not work for light pulse. Therefore, the duration of a light pulse is usually measured based on the idea of autocorrelation, i.e., measuring the light using light itself.

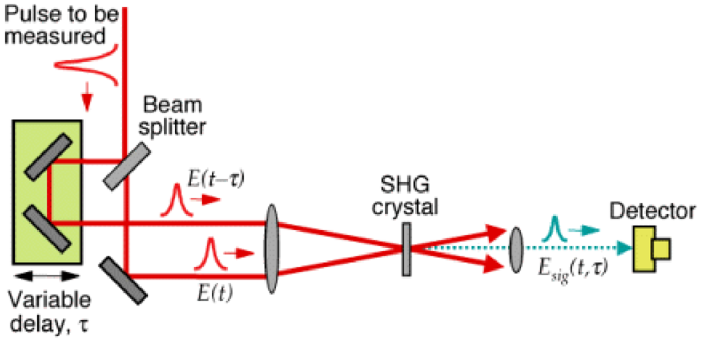

Figure 3.4 Optical diagram of an autocorrelator. The input pulse is split into two parts, one of which is sent into a delay stage. They are recombined onto a nonlinear crystal for second-harmonic generation. Scanning the time-delay of the two parts gives the SHG intensity as a function of delay, which corresponds to the time-domain profile of the input light.

By replacing the detector in an autocorrelator with a spectrometer, we have a useful device which measures the spectrum and the temporal profile simultaneously on a CCD camera. It is called a Frequency Resolved Optical Gratings (FROG).

3.2.4 Pulsewidth compression

Because of the presence of dispersion in any material, including air, a short pulse becomes broadened due to group velocity dispersion (GVD). GVD causes a frequency chirp [Fig. 3.6] in the pulse and it is possible to compress the pulsewidth when such chirp is present.

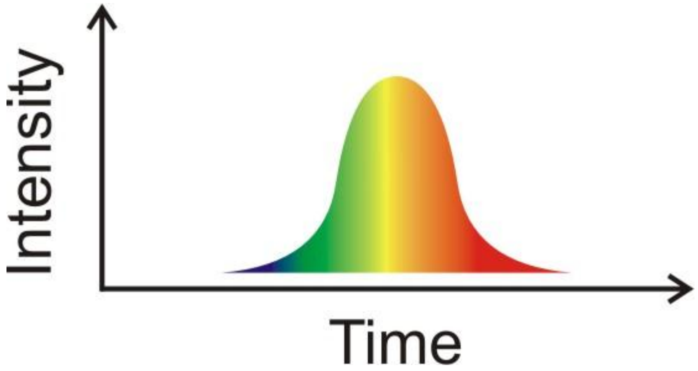

Figure 3.5 An example of temporally chirped pulse.

If the higher (lower) frequency is at the pulse front, it is called postively (negatively) chirped. This is best seen in the FROG spectrum in Figure 3.6. Passing through optical components usually induces positive chirp because the index of refraction of most materials decreases with increasing wavelength.

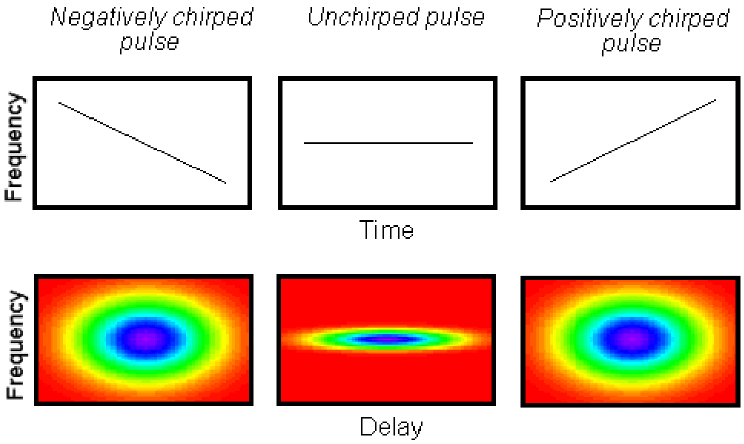

Figure 3.6 FROG images of ultrafast pulses. These pulses are chirped in the frequency domain.

Such kind of pulse can be compressed temporally by either using gratings or prisms to compensate for the chirp. This is because the spatial separation of different frequencies introduced by gratings and prisms can cause difference in path length of different frequencies and therefore induces a frequency dependent delay. We illustrate this idea by a prism pair compressor shown in Figure 3.7.

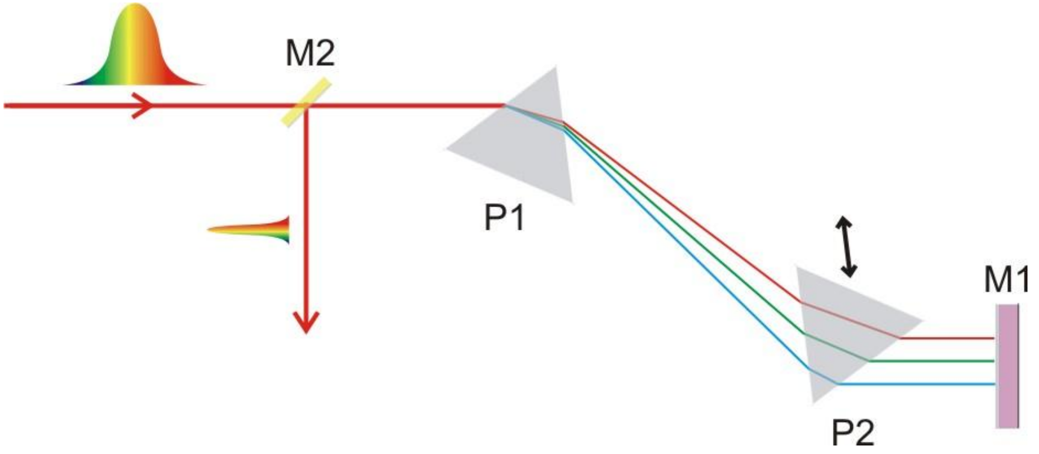

Figure 3.7 Schematics of a prism pair compressor. A time-chirped pulse goes through a pair of gratings P1 and P2 and is reflected by a roof mirror M1 to displace the reflected beam, which goes through the identical horizontal path in the prism pair and is picked up by a mirror M2.

The path length difference between different wavelengths introduced by the prisms is mainly determined by three parameters: the index of refraction of the prism; the distance between the prisms and the distances beams travel inside the second prism P2. Both positive and negative chirp is possible by adjusting all three parameters. For example, negative chirp from the prisms, which will compensate positive chirp, can be achieved by having a long distance between P1 and P2, while moving P2 in the direction of the black arrow so that only the tip of P2 is used. The path length difference is doubled by using a folding mirror M1, which can also be a roof mirror to elevate the beam so that the returning beam can hit M2. The distance between M1 and P2 does not change the path length difference. In general, all three parameters have to be in balance. A useful software program to simulate the pulse broadening and finding the right parameters for pulse compression can be found at http://www.lab2.de/.

We use a prism pair made of fused silica to compress 6 eV light for TrARPES. Besides being transparent to UV, fused silica has a bigger dispersion comparing with BK7 glass typically used for visible light. At short wavelength, the dispersion of the material is bigger and therefore the prism compressor is more effective for UV. The compressor in our amplifier laser utilizes a grating pair instead which allows much bigger path length difference for the same amount of distance. However, gratings have a much bigger intensity loss compared with prisms.

3.3 Higher harmonics generation and optical parametric amplification

3.3.1 Higher harmonics generation for photoemission

Since the laser light generated from a Ti:Sapphire regenerative amplifier or oscillator is only 1.5 eV, much less than the 4 ~ 5 eV work function of most materials, higher harmonics of these light are needed for the photoemission process. This is realized through the nonlinear optical processes in the gain medium under a very intense electromagnetic field, which can only be achieved by ultrafast laser pulses.

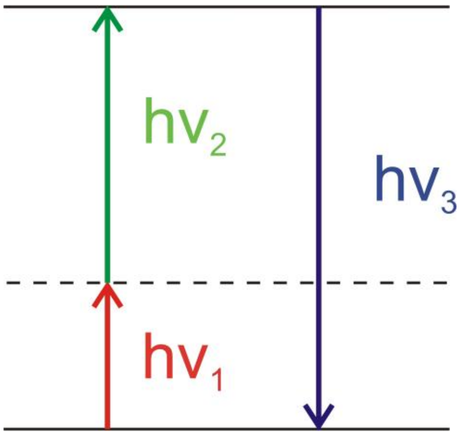

Figure 3.8 Frequency mixing process

To satisfy the conservation of energy [Fig. 3.8], only photons with energies satisfying the sum of the incoming photon energies can be generated. That is

$$\boldsymbol{h v_1} + \boldsymbol{h v_2} = \boldsymbol{h v_3}$$

where $\boldsymbol{h}$ is the Planck constant. $\boldsymbol{v_1}$, $\boldsymbol{v_2}$ and $\boldsymbol{v_3}$ are the frequencies of the photons. When $\boldsymbol{v_1} = \boldsymbol{v_2}$, it becomes second harmonic generation. The criteria for efficient frequency mixing is phase matching. It is described by the following equation:

$$\boldsymbol{k_1} + \boldsymbol{k_2} = \boldsymbol{k_3}$$

where $\boldsymbol{k_1}$, $\boldsymbol{k_2}$ and $\boldsymbol{k_3}$ are the wavevectors. The wavenumber is related to the frequency by:

$$k = \frac{v}{v_p} = n\frac{\nu}{c}$$

where v_p is the phase velocity, n is the index of refraction and c is the speed of light in vacuum. For plane waves, the phase matching condition is to satisfy the constructive interference of all three waves throughout the length of propagation in the medium so that the output intensity is maximized [Fig. 3.8].

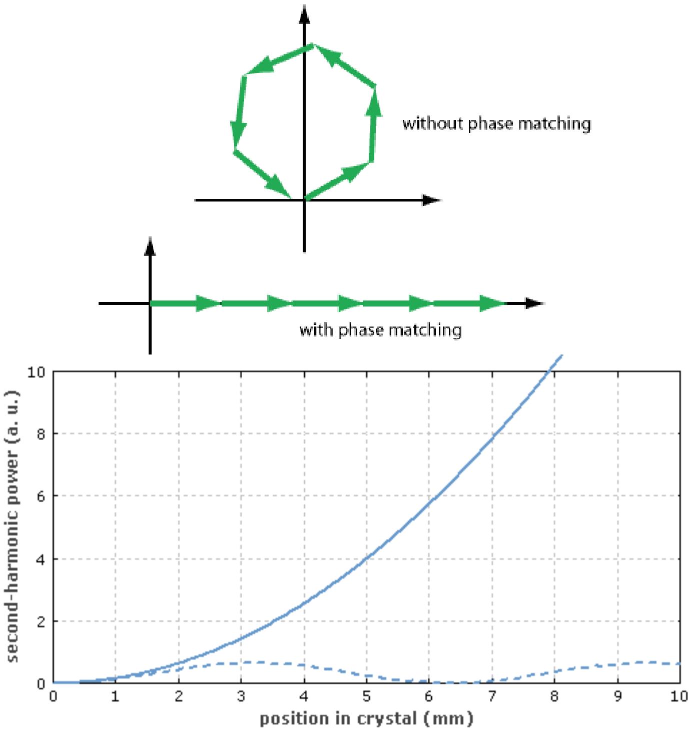

Figure 3.9 The electric field and the intensity of a mixed frequency wave as it propagates through the crystal. The top figure shows the interference of the electric field of the higher-order light as it is generated along the nonlinear medium. The lower figure shows the intensity as a function of distance in the crystal.

Due to the dispersion of any nonlinear medium, the phase matching condition cannot be satisfied in general. However, many materials we use for nonlinear optics are also birefringent, i.e., the index of refraction depends on the polarization of light. By exploiting the birefringence at certain angle of the crystal, it is then possible to achieve good phase matching. For two-wave mixing, Type I (II) phase matching means the two incoming waves have parallel (perpendicular) polarization.

For second harmonic generation with Type I phase matching, for example, the polarization of the fundamental light must be perpendicular to that of the second harmonic light to achieve phase matching with birefringence. This is indeed the case in our THG setup where SHG is generated at the first β-Barium Borate (BBO) crystal [Figure 3.10].

There are two ways to reach the fourth harmonic of a Ti:Sapphire laser for photoemission using BBO crystals. The first is frequency-doubling (SHG) twice and the second is mixing the fundamental with doubled light for third harmonic (THG) and mixing fundamental and third again to get to the fourth harmonic (FHG). All these higher harmonic generation processes can be achieved by BBO crystals with different cuts of crystal angle. Since the phase matching condition for SHG can only be achieved down to 409 nm, the latter one is chosen for our setup.

The optical diagram of our THG and FHG setup is shown in Figure 3.10. Horizontally polarized fundamental light with center wavelength at 780 nm enters the tripler after being telescoped down to about 3 mm in diameter [Figure 3.1]. A half-wave plate rotates the polarization to vertical for Type I SHG. Second harmonic light with horizontal polarization is generated. Due to the presence of GVD, the second harmonic pulse is delayed with respect to the fundamental when both leave the first BBO crystal. This time difference can reach 100 fs for a 1 mm thick crystal and has to be compensated in order to generate the third harmonic. Conventionally, an optical delay line with a delay stage is used for such compensation. However, a delay stage is bulky and hard to align. This drawback can be overcome with a birefringent crystal, such as a BBO, to delay pulses with different frequencies and perpendicular polarization, such as the fundamental and second harmonic light after the Type I SHG [Figure 3.10]. Instead of tuning the angle of the crystal for phase matching condition in nonlinear processes, the angle is tuned to perfectly compensate the delay of fundamental and second harmonic light so that they overlap in time when they reach another BBO crystal for THG. A second half-wave plate is used for rotating the fundamental light back to horizontal polarization for Type I phase matching in THG. THG is generated with vertical polarization. Different harmonics are separated with dichroic mirrors.

Fundamental and THG pulses are sent into the quadrupler. Another half-wave plate rotates the fundamental light to vertical polarization for Type I phase matching. A delay stage is used to compensate the delay between fundamental and THG because a time plate as used in the tripler is not enough for the delay in these two pulses. Fundamental, third and fourth harmonic are sent into a prism pair compressor where different harmonics are separated. The FHG has photon energy of 6.3 eV (195 nm) and can reach miliwatts of power. After compression, the pulsewidth is typically 150 fs.

BBO has many superior qualities making it crucial for nonlinear optics. Its wide phase-matchable range (190 nm ~ 1750 nm) and transmission range (190 nm ~ 3500 nm) makes it applicable for different nonlinear processes. Its high damage threshold (10 GW/cm^2) allows higher energy density and thus higher efficiency in harmonics generation. It is also easy to machine due to its good mechanical and physical properties and therefore can be manufactured into less than 10 um thickness to reduce pulse broadening for femtosecond laser pulses.

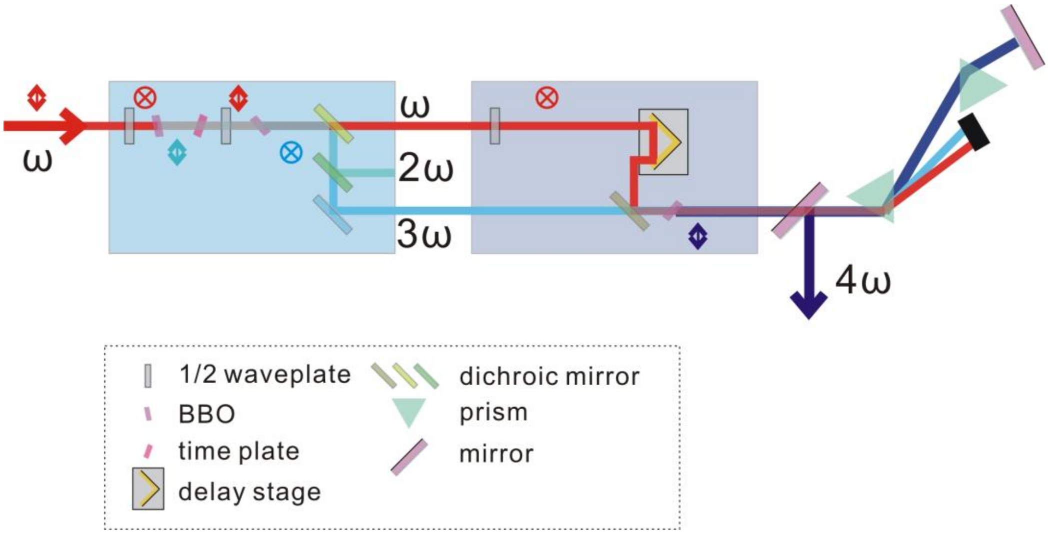

Figure 3.10 SHG and THG generation with prism-pair pulse compression.

The pulsewidth in the higher harmonic generation is mainly determined by the pulsewidth of the incoming pulses. To minimize the pulse broadening in the frequency mixing processes, thin crystals must be used. This is because the group velocity mismatch (GVM) in the crystal causes temporal walk-off among frequencies which causes broadening in the nonlinear processes that cannot be compressed back. This detrimental effect is more severe for generating DUV as the dispersion increases dramatically at short wavelength [Figure 3.11].

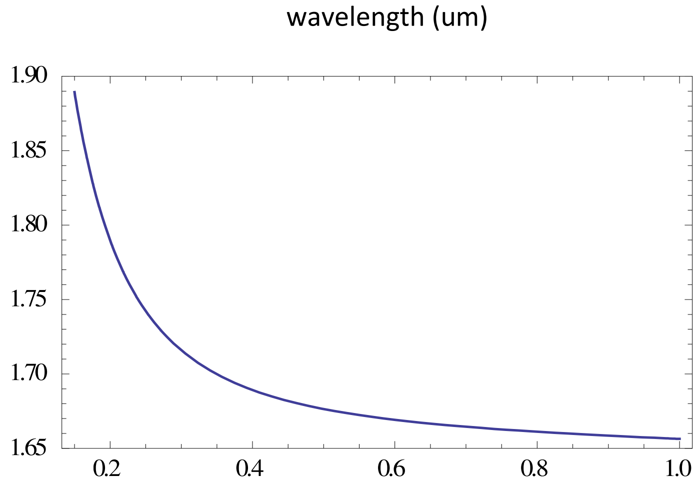

Figure 3.11 Index of refraction of BBO

GVM is fundamentally due to the difference between the phase velocity and group velocity of an ultrafast pulse propagating in a dispersive material. Phase velocity depends on the index of refraction and is always matched between waves under phase matching condition. Group velocity depends on the derivative of the index of refraction. Using

$$V_g \equiv \frac{dv}{dk}$$

$$k = \frac{2\pi}{\lambda} = \frac{2\pi n}{\lambda_0}$$

and

$$\frac{\nu}{k} = \frac{c}{n}$$

where λ and λ_0 are the wavelength in the medium and vacuum respectively, we get

$$V_g = \frac{c/n(\lambda_0)}{1 - \lambda_0 n'(\lambda_0)/n(\lambda_0)}$$

When there is no dispersion in the medium, i.e., $n'(\lambda_0) = 0$, the group velocity equals the phase velocity. Since $n'(\lambda_0) < 0$ for most nonlinear materials [Figure 3.11], group velocity is smaller than the phase velocity. Also because the dispersion increases in UV [Figure 3.11], higher harmonics lags behind fundamental light, which is illustrated in Figure 3.12 for the SHG. Frequency mixing will be similarly affected by GVM when the group velocities are different among all three pulses.

The time delay caused by GVM after passing through medium with length L is:

$$\delta t = \frac{L}{V_g(\lambda_1)} - \frac{L}{V_g(\lambda_2)}$$

We would like $\delta t \ll \Delta t$, the pulsewidth of the incoming pulse. Knowing the dispersion of the material, the critical crystal thickness can be obtained in order to satisfy this condition. We use 200 um, 100 um and 50 um BBO for SHG, THG and FHG respectively.

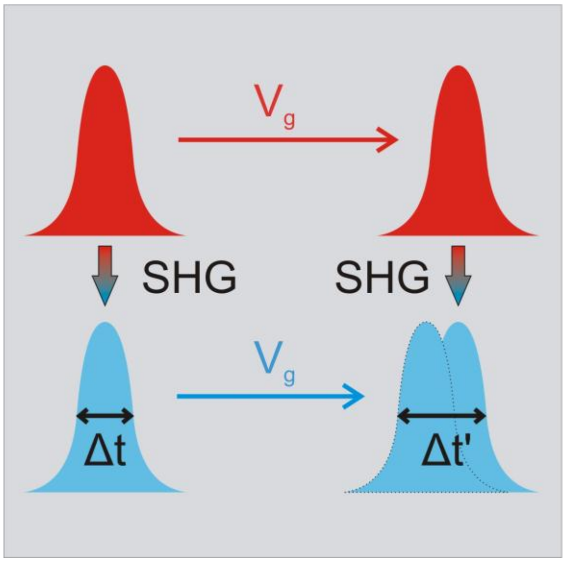

Figure 3.12 GVM in SHG broadens the pulsewidth. Due to the difference in group velocity of fundamental and second harmonic light, the SHG generated at a different position do not overlap with the SHG generated earlier. Such broadening cannot be compressed.

From the viewpoint of frequency domain, GVM limits the bandwidth that can satisfy the phase matching condition. This reduced bandwidth, called phase-matching bandwidth, broadens the pulse width due to the transform limit. The phase matching bandwidth can be obtained from the pulse width bandwidth product:

$$\delta\lambda = \frac{0.44\lambda_0^2/c}{\delta t}$$

A continuously tunable DUV laser source for ARPES can also be achieved through the optical-parametric process. It is based on the difference frequency generation of ultrafast light, which is detailed later in this chapter. The difference frequency signal, called signal and idler, typically lies in the infrared region, is continuously tunable. Tunable DUV is subsequently generated from the signal and idler by different frequency mixing processes in the BBO as described above.

Wavelength shorter than the 190 nm transmission cut-off of BBO can be generated from the newly discovered $KBe_2BO_3F_2$ (KBBF) crystal, which transmits down to 155 nm. 7 eV (177 nm) light has been successfully generated by SHG of the THG of Nd:YAG laser. However, because water absorption of wavelength shorter than 190 nm is quite strong, 7 eV DUV needs to be generated in a vacuum or nitrogen filled chamber.

The extra 1 eV produced by KBBF crystals is quite significant for covering a larger momentum space.

To cover the entire Brillouin zone of most of the crystals, photon energies above 10 eV is required. This is possible with ultrafast lasers by creating a very intense laser field in some noble gases such as Ar or Xe. Here the physical process that governs such higher order light generation is quite different from the harmonics generation in solid state materials.

3.3.2 OPA

In order to achieve tunable wavelength, optical parametric processes can be employed for both pump and probe light in TrARPES. While the sum frequency generation described in Section 3.3.1 mainly concerns obtaining light with higher frequencies than the input light, the output in optical parametric generation is smaller than the excitation frequency. One example is the difference frequency generation (DFG) as shown in the left panel of Figure 3.13. Lower frequency photons ν_2 and ν_3 are generated from spontaneous emission when a nonlinear material is excited by ν_1.

DFG is typically the first stage in an optical parametric amplifier (OPA). The generated signal (ν_2) and idler (ν_3) are then fed into the second stage as the seed for amplification [Figure 3.13 right panel].

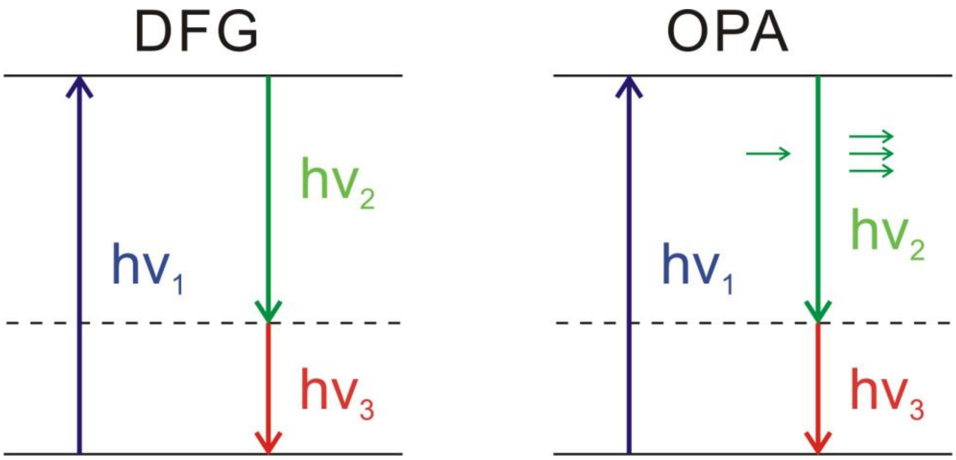

Figure 3.13 DFG and OPA energy diagram

3.4 ARTOF

3.4.1 Basic principles

An angle-resolved time-of-flight (ARTOF) electron spectrometer works a little differently from a hemispherical one. As shown in Figure 3.14, instead of having a slit, the entrance of the spectrometer is a big circle, which allows all electrons within certain angle ($\pm 22°$ in our setup) to enter. The magenta tube represents the electrostatic lenses which accelerate and focus the electrons and image it onto a 2D position-sensitive detector (PSD), which will be elaborated on in the next section. The spatial position on the 2D PSD corresponds to k_x and k_y of the electrons.

The energy of the electrons is determined from the flight-time they need to traverse the meter long lens tube. The electrons arriving at the detector at the same time have the same kinetic energy. Since there is no filtering at the entrance and the flight-time is recorded as an extra dimension, mapping of the (E, k_x, k_y) space does not involve any sample or detector rotation. As far as the material of this thesis is concerned, such energy-momentum space covers the entire surface Dirac cone of the prototypical topological insulator Bi_2Se_3.

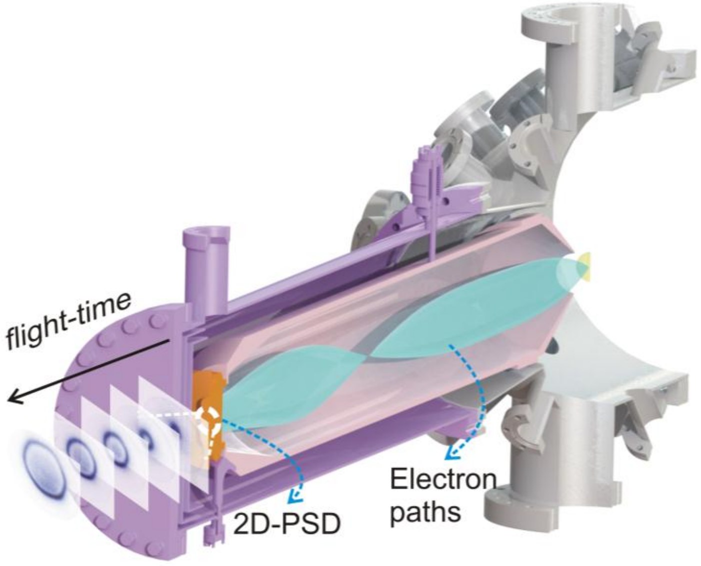

Figure 3.14 A time-of-flight electron spectrometer for ARPES. The photoemitted electrons are collected into a flight tube with electrostatic lenses. These lenses collimate and focus the electrons onto a 2D position-sensitive detector. The flight-time through the tube determined the energies of the electrons and the momentum is determined by the position on the detector.

The instrumental energy resolution is less than 0.15 meV at 2 eV kinetic energy and the angular resolution is $0.08°$ at $\pm 7°$ angular range mode. Such high resolution comparing with a hemispherical analyzer is owing to its unique detector.

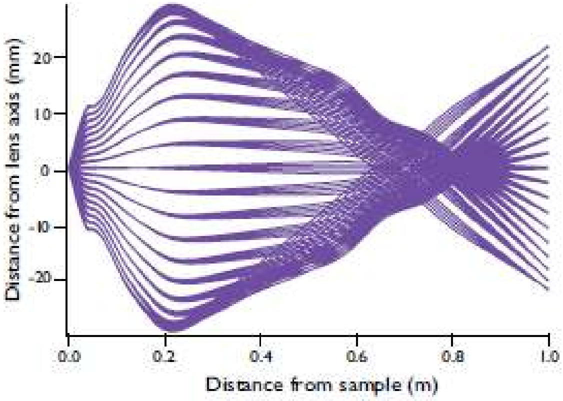

Figure 3.15 Electron trajectory in the flight tube

3.4.2 The detector

The position and timing sensitive detector of a TOF spectrometer is composed of two major components: a multi-channel plate (MCP) stack and a delay-line-detector (DLD). The MCP stack serves as a pre-amplification of single electron hits and converts them into a short intense electrical pulse. The MCP plate itself is a silicon wafer with many channels at a certain angle with the plate normal. When applying a big voltage difference across the plate (typically about 1000 V), an electron entering the front of the MCP bombards the wall of a channel and generates more electrons. This effect is avalanched through the thickness of the wafer to achieve current amplification. Two MCP plates stacked together in a so-called chevron configuration with opposite channel orientation for optimal amplification.

MCP is a fragile but expensive part of the detector and thus care must be taken in handling it. Because of the high gain ratio, MCPs can be easily damaged if the incoming electron flux is too high. It is therefore recommended to always start from the lowest possible flux to protect the MCP. MCP is also very hydroscopic. It is recommended to limit its exposure to air to less than 1 hour. MCP should not be operated at any pressure higher than 10^{-6} Torr because the high voltage applied to it can cause arcing.

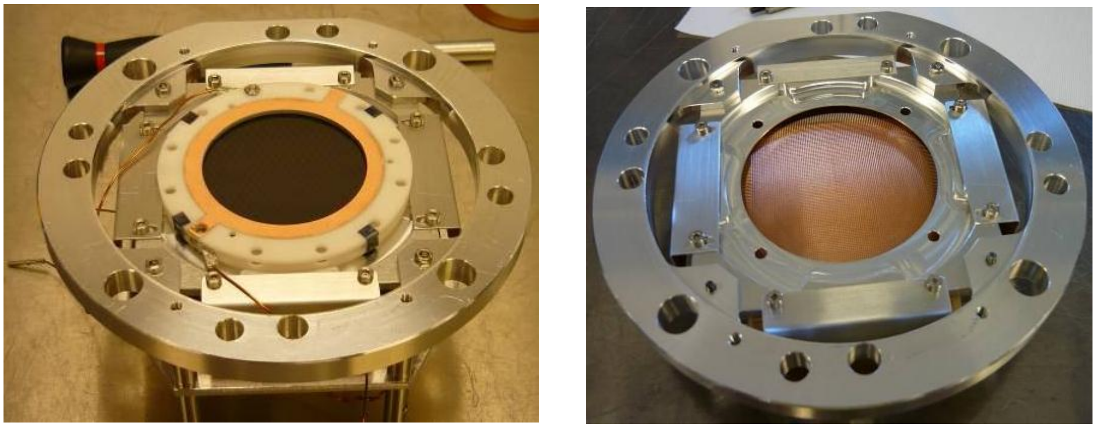

Figure 3.16 TOF detector with (a) the mounted MCP chevron stack and (b) the DLD exposed when the MCP is removed from the front.

The leading edge timing of the MCP event is used to determine the electron flight-time and eventually its energy. The electronics of our setup have a 100 ps time resolution, which enable sub-meV energy resolution. The flight-time is the time difference of electrons leaving the sample and hitting the MCP. Since the former time is hard to determine, the time at which photons hit the sample is used instead, which is a good approximation given the time resolution of the electronics. When photons impinge the sample, part of them are scattered into the flight tube and impact the MCP, which will cause cascade just like electrons do. This photon event will be registered on the MCP as a single peak in time, which precedes all electron events. The timing of photons incident on the sample is derived from the MCP photon event timing subtracting the photon flight-time in the lens tube. Because of the importance of timing in the determination of the electron energy, a pulsed photon source either from an ultrafast laser or a synchrotron with less than 20 ps pulse duration is required for a TOF spectrometer.

Situated right after the MCP stack, the DLD resolved the position of the electron hits and empowers the TOF spectrometer with angular-resolution. As shown in Figure 3.17, it looks like a mesh and is comprised of two perpendicularly-oriented meandering thin copper wires one on top of the other. Each wire is responsible for measuring one spatial dimension.

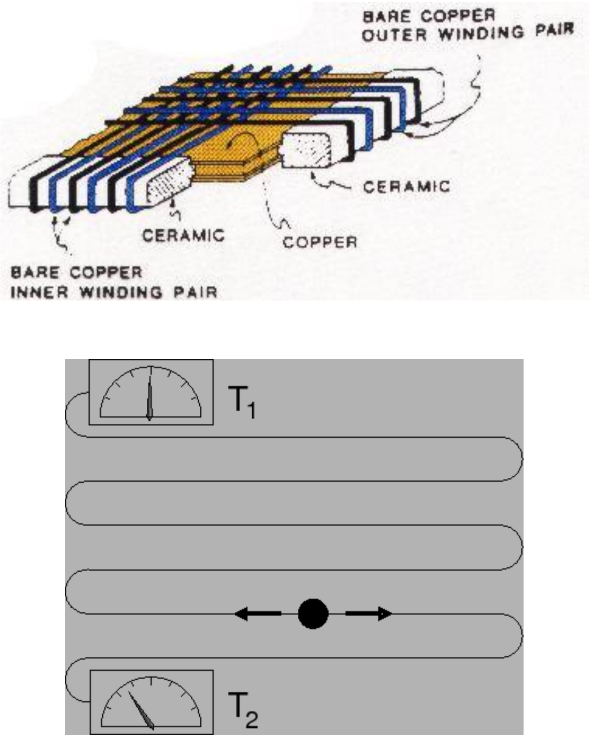

Figure 3.17 Schematics of delay-line detector. A delay-line detector is composed of two copper wires wound around a ceramic block perpendicular to each other into a mesh. When an electron pulse hits the detector, it generates two counter-propagating pulses along both wires. The time these pulses take to travel to the end of the wires are registered so that the position on the wire of the electron hit is known by the difference of the time.

The operation principle of a DLD is illustrated in Figure 3.17. When an electron pulse impinges on the DLD, it generates a pulse in both x and y wires. In each wire, the pulse propagates towards both ends of the wire and reaches the ends at times T_1 and T_2. Because the speed at which the pulse travels is fixed, the time difference $T_1 - T_2$ gives the position of the electron hit on the wire. x and y wires have the same known length. Therefore, the hit position on the DLD is determined by finding out the time difference for both wires.

The backend electronics perform these calculations and convert the timing into an (E, k_x, k_y) image. Due to the presence of the dark current from the MCP, not all hits are from the photoelectrons. To see if an event is really a signal, the backend electronics of the DLD also performs a sum-check $T_1 + T_2$, which would be a constant determined by the length of the wire for a real signal.

This way of determining the position of electron hit by the timing difference means that DLD cannot distinguish two electron hits arriving at about the same time. The backend electronics relies on the triggers from the photon source to separate hits from different triggering. If two or more hits arrive during one triggering period, all these events are discarded, which is another reason to use low photon flux. This also means the signal acquisition rate cannot exceed the photon source repetition rate and therefore a higher repetition rate will speed up the data acquisition. However, the space charge effect resulted from having too many electrons in one pulse will not be a concern under such condition.

3.4.3 Software

The software of ARTOF is both responsible for controlling the hardware of ARTOF and handling the conversion of (t, x, y) data from the DLD to the $I(E, k_x, k_y)$ spectra. As shown in Figure 3.18, SES libraries deal with the hardware to control the high voltage supply for the electrostatic lenses and the

MCP. The SES software is used to manually apply the voltages and to develop new lens table suitable for different applications. ARTOF Studio Console (ASC) is the primary user interface for controlling ARTOF with the preset lens table and data acquisition.

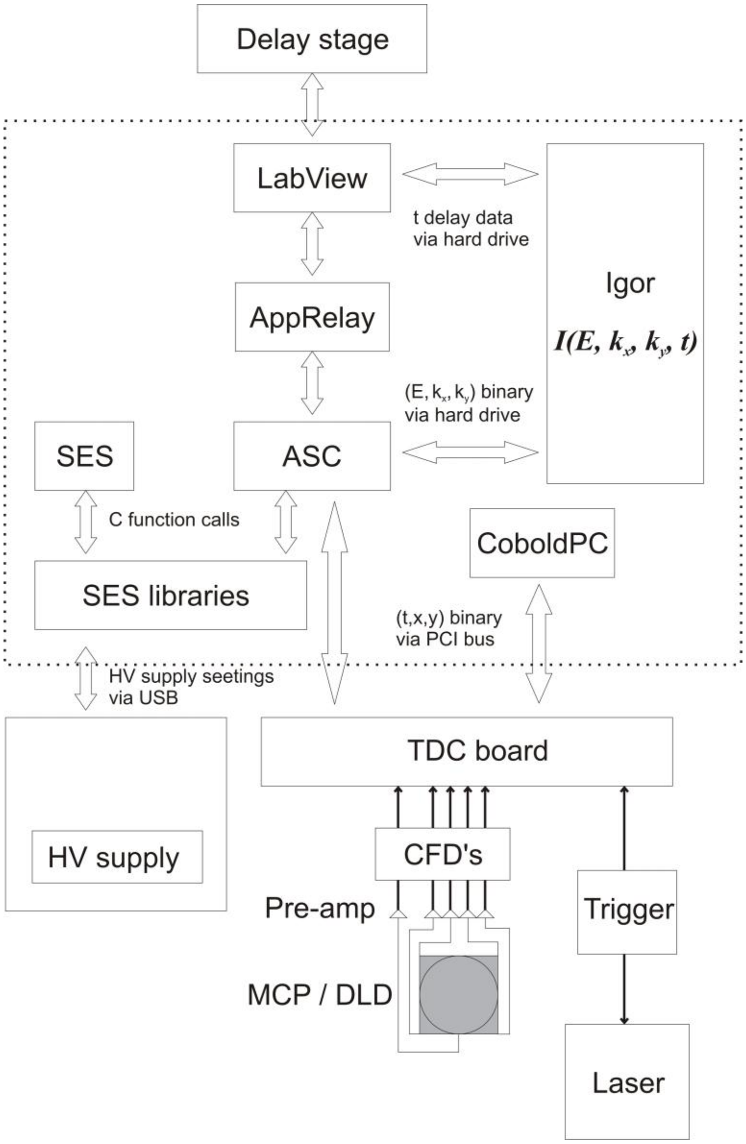

Figure 3.18 Hardware-Software interface. See text for details.

The TDC card plugged into the computer receives the NIM signal from all five channels from the CFD cards. These binary data are acquired by the ASC software (or alternatively CoboldPC for diagnostic purposes.) The ASC converts each hit into a vector that stores the (t, x, y) coordinate of the hit and put it into a file with other hits. By knowing the lens table used for these data, it also converts it into a (E, k_x, k_y) coordinate binary data and stores both on the hard drive. These data files occupy disk space proportional to the amount of hits, which is dependent on the number of repetitions and the acquisition time of each repetition. Both of these parameters, the lens table to run and the center electron energy can all be adjusted through the script file that ASC reads for commands of operations. To convert these binary data into an intensity spectrum, programs written in Igor is used. This program allows the user to select the resolution, which is the bin size to combine the binary hits into intensity.

For time-resolved experiments, an interface called AppRelay that links between LabView, which controls the delay stage, and ASC, which controls ARTOF is used. LabView also stores the time trace on the hard drive for the Igor program to read. Combining the intensity spectra at each time point, we obtain a 4D intensity matrix $I\left(E, k_x, k_y, t\right)$. This is the movie of the bandstructure dynamics we set after.

3.5 UHV system

3.5.1 UHV for surface science

The UHV system is the environment in which the TrARPES experiments are performed [Figure 3.19]. UHV conventionally means pressure less than 10^{-9} Torr. In our system, the pressure is typically $< 10^{-10}$

Torr and reaches 5×10^{-11} Torr during measurement. The reason to keep the pressure as low as this is because the stringent requirement of ARPES on surface cleanness.

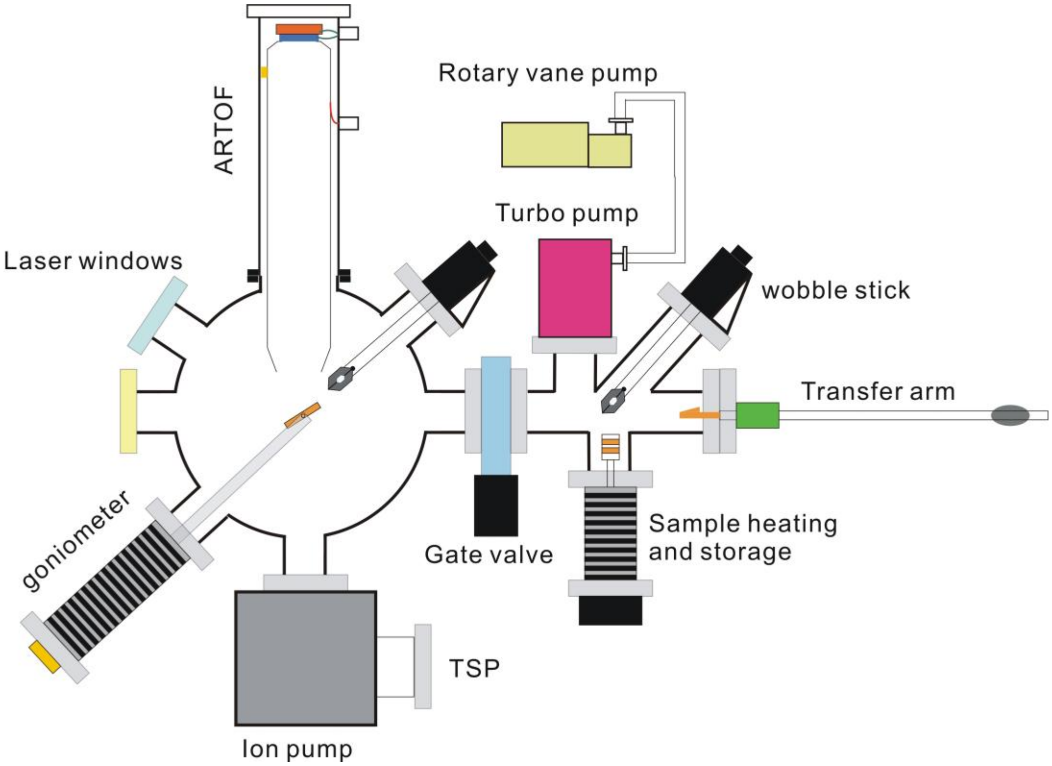

Figure 3.19 UHV system diagram

This requirement of surface cleanness is because of the short mean free path of electrons in the crystal. Any residual gas in the chamber can deposit layers of impurities on the surface which inelastically scatter photoemitted electrons and prevented them from reaching the detector with the original energy and momentum they carry in the crystal. Figure 3.20 shows a universal curve of the mean free path of electrons in common materials in the energy range relevant for photoemission. We can see that at around 50 eV, the mean free path is about one atomic layer and only goes up to several monolayers in the photon energies commonly used in sychrotron-based ARPES. Therefore, ARPES in general is a very surface sensitive technique. With the low photon energy of the laser source, the mean free path can reach 50 Å at 6 eV. Therefore, Laser-based ARPES is more bulk sensitive comparing with synchrotron-based ARPES.

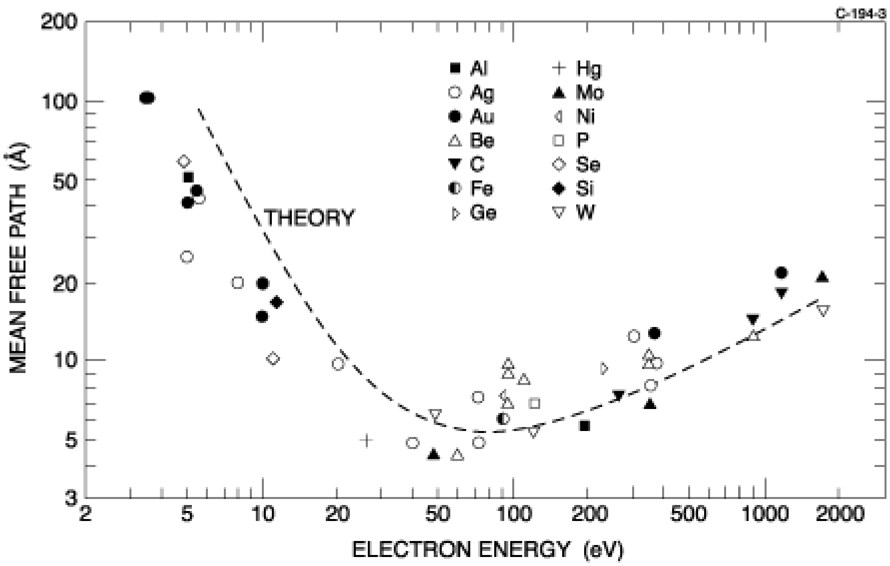

Figure 3.20 Universal curve of electron mean free path in metals. This curve shows that ARPES with synchrotron light sources are usually surface sensitive and laser-based ARPES is more bulk sensitive. From Hoffman website.

3.5.2 Generation of UHV

Our UHV generation from ambient pressure follow the followpwing routine. The chambers are sealed with conflat flanges and copper gaskets. With the gate valve open, the rotary vane pump starts and pulling pressure through the turbo pump mounted on the preparation chamber. It reaches its base pressure of 10^{-2} Torr in about 30 minutes. The turbo pump is turned on to further reduce the pressure to 10^{-8} Torr in couple hours. The outgassing from the chamber wall starts to reach the pumping speed of the turbo pump and the pressure reduces very slowly. With all the electronics detached, a bakeout at 110 °C is performed for about a week. A relatively low bake-out pressure is to protect the detector from overheating-caused damage. The pressure first increases at the start of the bake-out due to the increase of outgassing rate but reduces to 10^{-8} Torr towards the end of the bake-out due to the thorough desorption of water molecules from the chamber wall. After the chamber cools down to ambient temperature, the pressure drops to 10^{-10} Torr due to the lower outgassing rate at lower temperature. The dominant gas species left in the chamber at this stage is hydrogen molecules because turbo pumps have very small pumping speed for the light atoms and molecules. The ion pump and the titanium sublimation (TSP) pump are turned on and the pressure drops to 5×10^{-11} Torr due to the increased pumping speed. TSP is turned off after a 7-minute sublimation and only needs to be turned on once every month. The gate valve can be closed to separate the preparation chamber for loading or heating the samples while the ion pump is left on to maintain UHV in the measurement chamber [Figure 3.19].

Beside UHV, a successful ARPES experiment also requires absence of static electric or magnetic fields. Charging from photoemission or electron bombardment is a main source of electric field. To avoid that, the materials used in the analsis chamber are conductive or coated with graphite or silver paste. To expel the magnetic field, including the geomagnetic field that is strong enough to affect the electron trajectories of 2 eV electrons, the analysis chamber is shielded by two layers of μ-metal jackets inside the vacuum. μ-metal is a stainless steel alloy that has very high magnetic suseceptibility. The optical ports have small openings to allow less magnetic field penetration. The residual magnetic field at the sample position is less than 0.1 μT.

3.5.3 Sample loading

The samples are mounted onto a 10×10 mm^2 sample puck made of oxygen free high thermal conductivity copper (OFHC). The puck has a knob that has threads at the front which allows it to be screwed into holders with matching threaded holes [Figure 3.22]. A wobble stick with a mechanical pincer to grab onto the knob of the sample holder is mounted on the side that can reach the knob. The pucks can be loaded into the preparation chamber onto the storage cassette three at a time [Figure 3.19], where they can be stored under 10^{-9} Torr vacuum. In the preparation chamber, there is a heating stage with a puck holder made of molybdenum that can withstand 1000 °C and wired with resistive heaters. Heating can energize and evaporate certain surface adsorption so that cleaner surface of the sample can be exposed for ARPES measurement. There is also an electron-beam evaporator that allows evoporative deposition of noble metals such as gold and silver or magnetic metals like iron. Surface deposition with magnetic materials is particulalry relevant for topological insulators to induce time-reversal symmetry breaking on the surface.

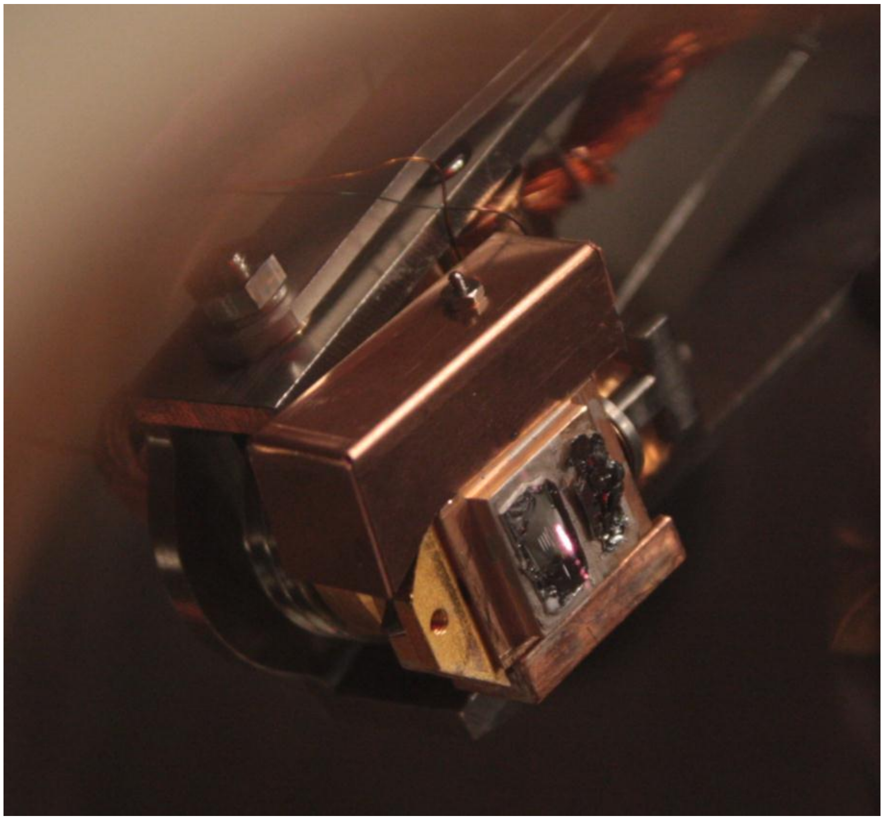

Figure 3.21 Sample holder with a Bi_2Se_3 sample under photoexcitation

The sample pucks can be loaded into the main chamber by the transfer arm. This involves the following steps in the preparation chamber: unscrewing the puck from the storage cassette or the heating stage with the wobble stick; pulling it out from the holder while holding it with the pincer; retracting the storage cassette to make space for the transfer arm; moving the transfer arm to the preperation chamber focal point and screwing the puck onto the arm. Once the sample puck is on the transfer arm, the pneumatically operated gate valve is opened and the transfer arm is sent into the focal point of the measurement chamber. The wobble stick in the measurement chamber picks up the puck from the transfer arm, which is then retracted back into the preparation chamber. The puck is then screwed onto the sample holder on the goniometer, which features motorized three-axis translation and three-axis rotational motion. It can also be cooled to 10 K by connecting with a copper braid to the cold finger of an open-cycle liquid helium cryostat. It can be cooled down to the base temperature within one hour and the helium consumption rate is about 2 L/hour at 10 K.

3.6 Sample preparation and characterization

3.6.1 Sample growth

Proper sample preparation is especially important for ARPES because of the stringent requirement on surface cleanness and homogeneity. Photoelectrons are difficult to escape a dirty surface as discussed earlier. Because the angular resolution depends on the laser spot size, the DUV laser has to be focused down to 100 µm. Inhomogeneity caused by domains or surface roughness smaller than this length scale blurs the measured bandstructure. To this end, sample with good single crystal quality has to be prepared and a clean surface exposed at the time of measurement.

Data presented in Chapter 4 and Chapter 5 of this manuscript is acquired on single crystal Bi_2Se_3 samples grown by the floating zone method. For the high doping level samples where the Dirac point is 0.28 eV below the Fermi level, stoichiometric mixture of Bi and Se are used. And for the low doping level samples where the Dirac point is 0.06 eV below the Fermi level, the initial mixture of Bi:Se = 2:4.06 are used. Both types are slightly doped with As to improve its cleaving properties and was grown by melting a 10 g mixture of Bi and Se shot with trace amounts of As powder (x=0.00129) in an evacuated quartz tube at 850 °C. After 12 hours at this temperature, the mixture was cooled to 720 °C over 2 hours, then slowly cooled to 650 °C over 2 days. The batch was annealed at 650 °C for 2 days then furnace cooled to room temperature. Samples were checked to be single phase with X-ray diffraction using a Bruker D8 diffractometer with Cu Kα radiation (λ = 1.54 Å) and a two-dimensional area detector.

3.6.2 Sample cleaving

To be able to expose fresh surfaces in UHV, a method called cleaving is performed *in situ*. To be able to do that, a ceramic post (or a stainless steel screw) is glued to the top surface with silver epoxy or Torr-Seal [Figure 3.22]. The bottom surface of the sample is similarly glued to the sample holder. To avoid charging during photoemission, exposed surfaces have to be conductive. If ceramic posts or Torr-Seal is used, they have to be coated with graphite liquid solution. If silver epoxy is used, the holder has to be heated to 80 °C for more than 5 hours to harden it.

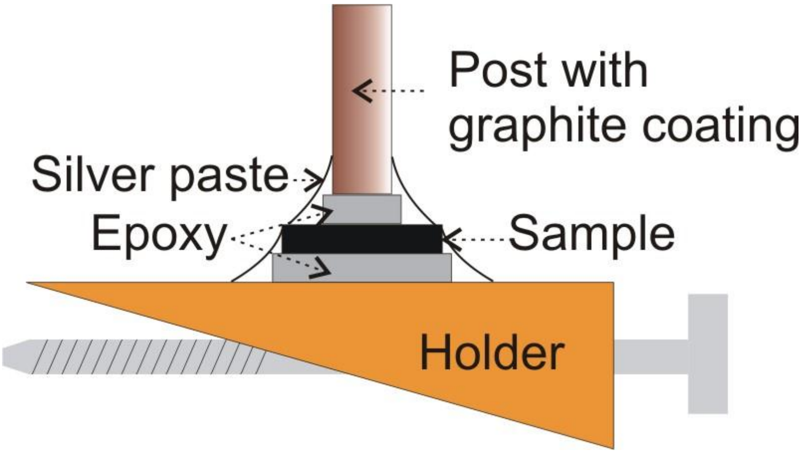

Figure 3.22 Sample prepared for cleaving. The sample is sandwiched in between the holder and the post by silver-epoxy. If the post is hit with mechanical force, it detaches with the top layer of the sample and exposes a fresh surface.

Because the bonding force of epoxy is stronger than the van der Waals force among quintuple layers of Bi_2Se_3, the sample will be cleaved when a mechanical force hit the post. This is performed with the wobble stick in our UHV system. For samples that have very strong bonding, e.g., ionic crystals, cleaving will not work very well. That is why ARPES is most effective to study layered single crystals.

For single crystal samples that are not cleavable, they have to be prepared to have a mirror-like surface finish in air first. After they are loaded into vacuum, they can be cleaned by heating or by ion bombardment (plasma cleaning). The quality of the surface is typically checked by low-energy electron diffraction (LEED). Because of the small mean free path of low energy electrons, LEED is a sensitive probe of the surface cleanness and homogeneity.

Besides the single crystals grown with the floating zone method, samples can be grown epitaxially *in situ* by molecule-beam epitaxy or using Knudson cell evaporation.

Chapter 4

CD-ARPES on topological materials

4.1 Introduction

4.1.1 Motivation

Topological insulators have been recently predicted to exhibit spin-dependent absorption of circularly polarized light [61-63]. Such momentum dependent light absorption will enable the generation of highly spin-polarized surface electrical currents whose direction can be switched by the light helicity [64]. However, conventional probes such as transport and optics have not been able to demonstrate spin-dependent differential absorption of left- versus right-circularly polarized light, i.e., circular dichroism (CD), from the surface states (SS) because of the combined need for energy-momentum resolution and surface sensitivity. TOF-ARPES is very suited for investigating CD of topological insulators because it can map out the energy-momentum space and distinguish between surface and bulk states simultaneously without sample rotation.

4.1.2 Concurrent work

There are many concurrent experimental and theoretical studies of the momentum-dependent circular dichroism effect from ARPES of topological materials. Consistent with our work [65], which is presented in Section 4.4, the CD spectra in Bi_2Se_3 have also been observed by Park *et al.* [66-67] and Sholtz *et al.* [68] using hemispherical electron spectrometers and synchrotron radiation source. Ishida *et al.* [69] observed CD in the ARPES spectra of $Cu_xBi_2Se_3$, a topological superconductor at low temperature.

Besides the surface states of topological insulators, momentum dependent CD-ARPES spectra have also been observed in other spin-orbited coupled systems. Bahramy *et al.* [70] have shown that the quantum well states in Bi_2Se_3 also exhibit CD patterns that are consistent with an origin due to spin polarization. Similar effects are observed in both the surface states and quantum well states of Bi thin films by Bian *et al.* [71].

First principle calculations performed by Mirhosseini *et al.* [72] and Henk *et al.* [73] on pure and doped Bi_2Te_3 support all these observations and provide computational evidence that the momentum dependent CD ARPES spectra are the direct consequence of the spin-orbit coupling of these materials.

4.2 Theory of photoemission on spin-orbit coupled materials

The microscopic Hamiltonian of an electron in a solid is given by:

$$H = \frac{\boldsymbol{P}^2}{2m} + V(\boldsymbol{r}) + \frac{\hbar}{4m^2c^2}(\boldsymbol{P} \times \boldsymbol{\nabla} V(\boldsymbol{r})) \cdot \boldsymbol{s} \qquad \textbf{4.1}$$

Where $\boldsymbol{P}$ is the momentum operator, $V(\boldsymbol{r})$ is crystal potential due to ions and $\boldsymbol{s}$ is the electron spin. The last term in the equation is the spin-orbit coupling term which comes from relativistic corrections and $\boldsymbol{\nabla} V(\boldsymbol{r})$ is not just the macroscopic electric field near the surface. Coupling of an electron to an electro-magnetic field is through the substitution of

$$\boldsymbol{P} \rightarrow \boldsymbol{P} - \boldsymbol{eA}$$

where $\boldsymbol{A}$ is the vector potential of the electro-magnetic field. To the first order in $\boldsymbol{A}$:

$$H(\boldsymbol{A}) = H - \frac{e}{m}\boldsymbol{P} \cdot \boldsymbol{A} - \frac{\hbar e}{4m^2c^2}(\boldsymbol{\nabla} V \times \boldsymbol{s}) \cdot \boldsymbol{A} \equiv H - \boldsymbol{\mathcal{P}} \cdot \boldsymbol{A} \qquad \textbf{4.2}$$

Besides the standard dipole term, $\boldsymbol{\mathcal{P}}$ also includes a spin-dependent term arising from spin-orbit coupling. The photoemission matrix element between the initial surface states and the final states is given by

$$M(\boldsymbol{k}, f) = \langle f_{\boldsymbol{k}} | \boldsymbol{\mathcal{P}} \cdot \boldsymbol{\mathcal{A}} | \boldsymbol{k} \rangle \qquad \textbf{4.3}$$

where $|\boldsymbol{k}\rangle$ is the 2D surface state at momentum $\boldsymbol{k} = (k_x, k_y)$, which is non-degenerate and has a definite spin polarization; $|f_{\boldsymbol{k}}\rangle$ labels a final state which must have the same $\boldsymbol{k}$ as the initial state and an energy $\hbar\omega$ greater than the initial state in order to conserve momentum and energy due to the small momentum of photons. $\boldsymbol{\mathcal{A}}$ is a complex quantity $\boldsymbol{\mathcal{A}} \equiv \int dt\boldsymbol{A}(t)e^{-i\omega t}$ and is responsible for photon absorption processes.

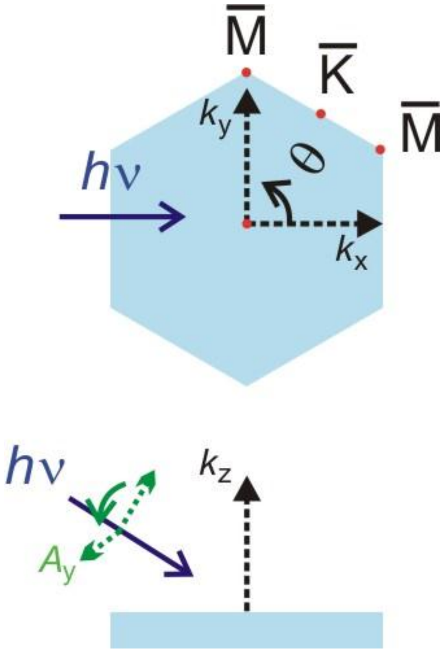

Figure 4.1 Photon incident geometry with reference to the sample

Consider a circularly polarized light incident onto the surface with wavevector in the xz plane [Figure 4.1], where x is along the ΓK direction and z is the surface normal direction. The corresponding vector potential is given by

$$\boldsymbol{A} = (A_x \sin\omega t, A_y \cos\omega t, A_z \sin\omega t)$$

$$\boldsymbol{\mathcal{A}} = (-iA_x, A_y, -iA_z)$$

To calculate the matrix element $M(\boldsymbol{k}, f)$ quantitatively, it requires knowing the microscopic electron wavefunctions and crystal potential near the surface. However, we will show that the momentum dependence of $M(\boldsymbol{k}, f)$ near $\boldsymbol{k} = 0$ can be obtained analytically without such details. This is because in the limit of $\boldsymbol{k} \to 0$, only the spin polarization $\boldsymbol{s}$ depends on momentum $\boldsymbol{k}$ in a singular way, whereas all other quantities in the matrix element are smooth functions of $\boldsymbol{k}$ and can therefore be replaced by their values at $\boldsymbol{k} = 0$. In particular, the initial state $|\boldsymbol{k}\rangle$ is given by

$$|\boldsymbol{k}\rangle = u_{\boldsymbol{k}}|\phi_{+}^{i}\rangle + v_{\boldsymbol{k}}|\phi_{-}^{i}\rangle \tag{4.4}$$

where $|\phi_{\pm}^{i}\rangle$ denotes the two degenerate surface states at $\boldsymbol{k} = 0$ with total angular momentum z component $J^z = L^z + s^z = \pm\frac{1}{2}$. Note that we do not need to assume $|\phi_{\pm}\rangle$ are the eigenstates of s^z with 100% spin polarization. In fact, they are pseudospin (total angular momentum) eigenstates because spin and orbital degrees of freedom are not independently conserved in a spin-orbit coupled system. As a result, the two component spinor $(u_{\boldsymbol{k}}, v_{\boldsymbol{k}})$ in reality specifies the spin polarization at momentum $\boldsymbol{k}$. The only assumption we make is that the final states $|f_{\boldsymbol{k}}\rangle$ have negligible spin splitting at small $\boldsymbol{k}$ so that they can be approximated by the two spin degenerate states at $\boldsymbol{k} = 0$ as $|\phi_{+}^{f}\rangle$ and $|\phi_{-}^{f}\rangle$. This is a very valid assumption because the final states have energies around 6 eV above the surface states so that they are well within the spin-degenerate bulk band continuum. We do not need to assume that final states are free electron like plane waves nor do they have zero spin-orbit coupling.

We can calculate the matrix elements between initial states $|\phi_{\pm}^{i}\rangle$ and final states $|\phi_{\pm}^{f}\rangle$. Because $|\phi_{+}^{i,f}\rangle$ and $|\phi_{-}^{i,f}\rangle$ are time-reversal partners, it follows from time-reversal symmetry that

$$\langle\phi_{+}^{f}|\mathcal{P}_x + i\mathcal{P}_y|\phi_{-}^{i}\rangle = \langle\phi_{-}^{f}|\mathcal{P}_x - i\mathcal{P}_y|\phi_{+}^{i}\rangle^*$$

$$\langle\phi_{+}^{f}|\mathcal{P}_z|\phi_{+}^{i}\rangle = -\langle\phi_{-}^{f}|\mathcal{P}_z|\phi_{-}^{i}\rangle^*$$

Under mirror reflection operation about yz plane

$$M_x: x \to -x$$

We have

$$|\phi_+\rangle \to i|\phi_-^{\boldsymbol{i}}\rangle$$

$$|\phi_-^f\rangle \to i|\phi_f, \downarrow\rangle$$

Since the crystal has mirror symmetry about yz plane, we find

$$\langle \phi_+^f | \mathcal{P}_x + i\mathcal{P}_y | \phi_-^i \rangle = -\langle \phi_-^f | \mathcal{P}_x - i\mathcal{P}_y | \phi_+^i \rangle$$

$$\langle \phi_+^f | \mathcal{P}_z | \phi_+^i \rangle = \langle \phi_-^f | \mathcal{P}_z | \phi_-^i \rangle$$

It follows from three-fold rotational symmetry that all other matrix elements of $\mathcal{P}_x + i\mathcal{P}_y$ and $\mathcal{P}_z$ vanish. Define

$$-\langle \phi_-^f | \mathcal{P}_x - i\mathcal{P}_y | \phi_+^i \rangle \equiv ia$$

$$\langle \phi_-^f | \mathcal{P}_z | \phi_-^i \rangle \equiv ib \qquad \textbf{4.5}$$

where a and b are real constants. Substituting Eq. 4.3 and Eq. 4.4 into Eq. 4.5, we obtain the photoemission transition rate from the matrix element

$$\sum_s |M(\boldsymbol{k}, s)|^2 = a^2 \left(|\mathcal{A}_x|^2 + \left|\mathcal{A}_y\right|^2 \right) + b^2 |\mathcal{A}_z|^2 + a^2 \mathrm{Im}\left(\mathcal{A}_x \mathcal{A}_y^*\right)(|u_{\boldsymbol{k}}|^2 - |v_{\boldsymbol{k}}|^2)$$

$$+ 2ab\mathrm{Im}\left[\mathcal{A}_z \mathcal{A}_x^* (iu_{\boldsymbol{k}} v_{\boldsymbol{k}}^* - iv_{\boldsymbol{k}} u_{\boldsymbol{k}}^*) - \mathcal{A}_z \mathcal{A}_y^* (u_{\boldsymbol{k}} v_{\boldsymbol{k}}^* + v_{\boldsymbol{k}} u_{\boldsymbol{k}}^*)\right]$$

where we have summed over the two degenerate final states $s = \uparrow, \downarrow$. To simplify the above expression, we now introduce a pseudospin Pauli matrix $\sigma^z = \pm 1$ to denote the Kramers doublet $|\phi_\pm^{\boldsymbol{i}}\rangle$. Using the identity

$$|u_{\boldsymbol{k}}|^2 - |v_{\boldsymbol{k}}|^2 = \langle \sigma^z \rangle_{\boldsymbol{k}}$$

$$u_{\boldsymbol{k}} v_{\boldsymbol{k}}^* + v_{\boldsymbol{k}} u_{\boldsymbol{k}}^* = \langle \sigma^x \rangle_{\boldsymbol{k}}$$

$$i u_{\boldsymbol{k}} v_{\boldsymbol{k}}^* - i v_{\boldsymbol{k}} u_{\boldsymbol{k}}^* = \langle \sigma^y \rangle_{\boldsymbol{k}}$$

we find

$$\sum_s |M(\boldsymbol{k}, s)|^2 = I_0 + a^2 \mathrm{Im}\left(\mathcal{A}_x \mathcal{A}_y^*\right) \langle \sigma^z \rangle_{\boldsymbol{k}} + 2ab\,\mathrm{Im}\left[\mathcal{A}_z \mathcal{A}_x^* \langle \sigma^y \rangle_{\boldsymbol{k}} - \mathcal{A}_z \mathcal{A}_y^* \langle \sigma^x \rangle_{\boldsymbol{k}}\right] \qquad \mathbf{4.6}$$

where

$$I_0 \equiv a^2 \left(|\mathcal{A}_x|^2 + \left|\mathcal{A}_y\right|^2 \right) + b^2 |\mathcal{A}_z|^2$$

is a $\boldsymbol{k}$ independent contribution. Eq. 4.6 is our main result as it directly relates the photoemission transition rate to the spin polarization of surface states. Note that our derivation is entirely based on symmetry analysis. The right hand side of Eq. 4.6 is the only combination of the vector potential and the spin polarization which is invariant under the time-reversal and C_{3v} crystal symmetry. If we change the helicity of light, it is equivalent of changing $A_y \rightarrow -A_y$. So the momentum dependent difference in ARPES intensity taken with left and right circularly polarized light is given by

$$\Delta I = a^2 \mathrm{Im}\left(\mathcal{A}_x \mathcal{A}_y^*\right) \langle s^z \rangle_{\boldsymbol{k}} - 4ab\,\mathrm{Im}\left[\mathcal{A}_z \mathcal{A}_y^* \langle s^x \rangle_{\boldsymbol{k}}\right] \qquad \mathbf{4.7}$$

We can see only $\langle \sigma^x \rangle_{\boldsymbol{k}}$ and $\langle \sigma^z \rangle_{\boldsymbol{k}}$ are left in the equation because both terms are odd under reversing the helicity. To obtain $\langle s^y \rangle_{\boldsymbol{k}}$ we can use the sum of the ARPES spectra obtained with left and right helicity:

$$\sum I = 2I_0 + 4ab\,\mathrm{Im}\left[\mathcal{A}_z \mathcal{A}_x^* \langle s^y \rangle_{\boldsymbol{k}}\right] \qquad \mathbf{4.8}$$

Unlike the difference spectra, the sum spectra has a momentum independent term as an offset to the term proportional to $\langle s^y \rangle_{\boldsymbol{k}}$. However, because the spin texture wind around the Dirac point, the line integral over a closed path encircling the Dirac point will have zero contribution from $\langle s^y \rangle_{\boldsymbol{k}}$. Therefore, we can subtract the constant term from the sum intensity spectra after performing such integration in order to obtain $\langle s^y \rangle_{\boldsymbol{k}}$. Alternatively, $\langle s^y \rangle_{\boldsymbol{k}}$ can be obtained by extracting the $\langle s^x \rangle_{\boldsymbol{k}}$ component when sample is rotated by 90°.

We note that these matrix elements we calculate for photoemission intensity hold perfectly well in a non-interacting electron picture where the sudden approximation is valid. These conditions are fully met in our experiment because the band structure of Bi_2Se_3 is well modeled neglecting electron correlations and the sudden approximation has been shown to be valid when using 6 eV photons. It can be generally applied to materials with spin-orbit coupling.

4.3 TOF-ARPES on Bi_2Se_3

In this section, I present data obtained with a TOF-ARPES electron spectrometer. Different from a hemispherical electron spectrometer, the $I(E, k_x, k_y)$ spectra [65] is obtained simultaneously without any rotation of the sample or the detector as explained in Section 3.4.

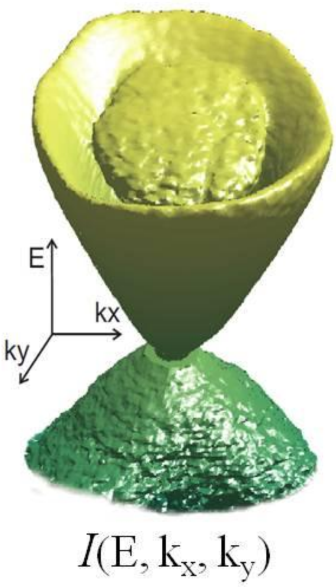

Figure 4.2 Energy-momentum intensity spectra obtained from TOF-ARPES. Plotted is the constant intensity contour.

Such intensity spectrum for Bi_2Se_3 is shown in Figure 4.2. The vertical axis is energy and the horizontal axes are the momentum k_x and k_y. The cone on the outside is from the surface states and is called the Dirac cone. The point where the upper cone and lower cone touches is called the Dirac point. The blob 'floating' inside is the bulk conduction band. It does not touch the surface states above the Dirac point, which means surface and bulk states do not hybrid. However, this is not the case below the Dirac point. This can be well seen in the energy-momentum cut through the $I(E, k_x, k_y)$ spectra [Figure 4.3]. The dispersion below the Dirac point blurs, which suggests that surface and bulk states hybridize. We can extract the Fermi velocity to be $v_F = 3.5eV\text{Å}^{-1}$, consistent with earlier ARPES study on Bi_2Se_3 [25].

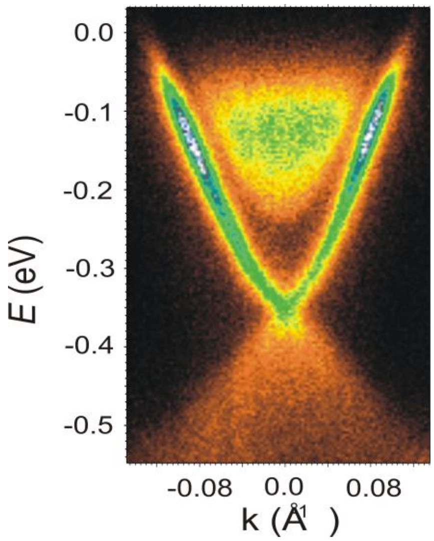

Figure 4.3 Energy-momentum cuts through the intensity spectra along ΓK direction.

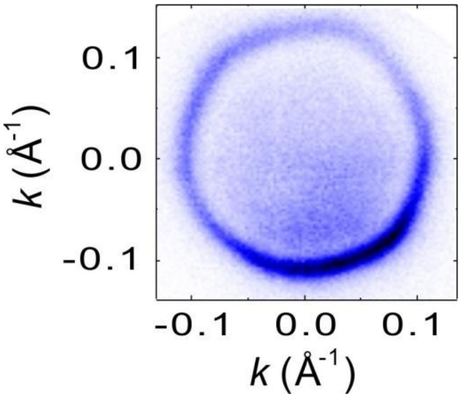

Figure 4.4 Constant energy slice of the intensity spectra of Bi_2Se_3 showing hexagonal warping effect.

We can also see the hexagonal shape on the Dirac cone, especially above the Dirac point. Such shape can be seen more clearly from the constant energy cut across the $I(E, k_x, k_y)$ spectra [Figure 4.3]. This is due to the higher order terms in the $\boldsymbol{k} \cdot \boldsymbol{p}$ Hamiltonian and is called hexagonal warping effect as proposed by Fu [4]. It has been observed in Bi_2Te_3 earlier [7] and Bi_2Se_3 only recently [74] using hemispherical analyzer earlier.

Bi_2Te_3 has a more warped Fermi surface than Bi_2Se_3 as can be seen from its concave shape [Figure 4.4]. The following Hamiltonian can be derived from the symmetry properties of the crystal:

$$H = E_0(k) + v_{\boldsymbol{k}}\left(k_x\sigma_y - k_y\sigma_x\right) + \frac{\lambda}{2}({k_+}^3 + {k_-}^3)\sigma_z \qquad \textbf{4.9}$$

where $k_\pm = k_x \pm ik_y$. The first term $E_0(k) = \frac{k^2}{2m^*}$ generates particle-hole asymmetry. The second term is the $\boldsymbol{k} \cdot \boldsymbol{p}$ Hamiltonian that gives the linear dispersion of the Dirac cone. The third term is the higher order term responsible for the warping effect of the energy contour.

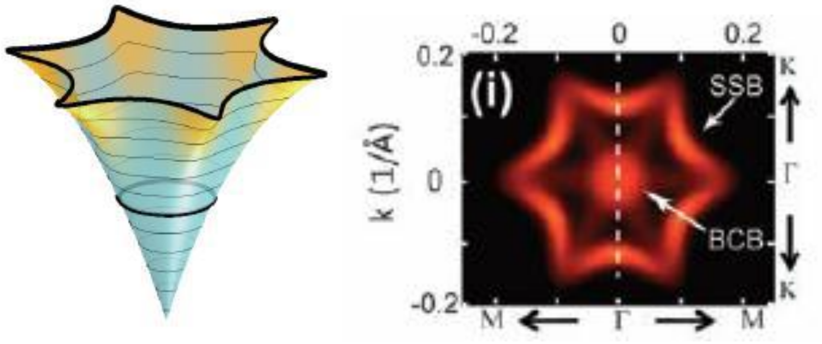

Figure 4.5 Hexagonal warping effect in Bi_2Te_3. Left: constant energy contour of the hexagonally warped surface states from first principle calculation [4]. Right: constant energy cuts of the Fermi surface of Bi_2Te_3. Adapted from [7].

The solution to this Hamiltonian yields the following dispersion for surface states:

$$E_\pm(\boldsymbol{k}) = E_0(k) \pm \sqrt{{v_{\boldsymbol{k}}}^2k^2 + \lambda^2k^6\cos^2 3\theta} \qquad \textbf{4.10}$$

where λ characterizes the magnitude of the warping of the energy contour. For Bi_2Te_3 $\lambda = 260eV \cdot \text{Å}^3$ [4] and for Bi_2Se_3 $\lambda = 128eV \cdot \text{Å}^3$ [74].

The warping effect not only changes the energy contour but also modulates the spin texture. This can be seen from the coupling of momentum to the spin operator in the warping Hamiltonian Eq. 4.9. Since it couples to σ_z, the spin polarization of the surface states should have an out-of-plane component, which does not exist in the ideal regime where the lowest order in the $\boldsymbol{k} \cdot \boldsymbol{p}$ theory is needed. Because it has been shown that the surface states at Γ are almost 100% spin-polarized, $S_z \approx \langle \sigma_z \rangle$. Therefore S_z can be calculated from the eigenstates of the warping Hamiltonian to be

$$S_z = \frac{\cos 3\theta}{\sqrt{\cos^2 3\theta + 1/(ka)^4}} \tag{4.11}$$

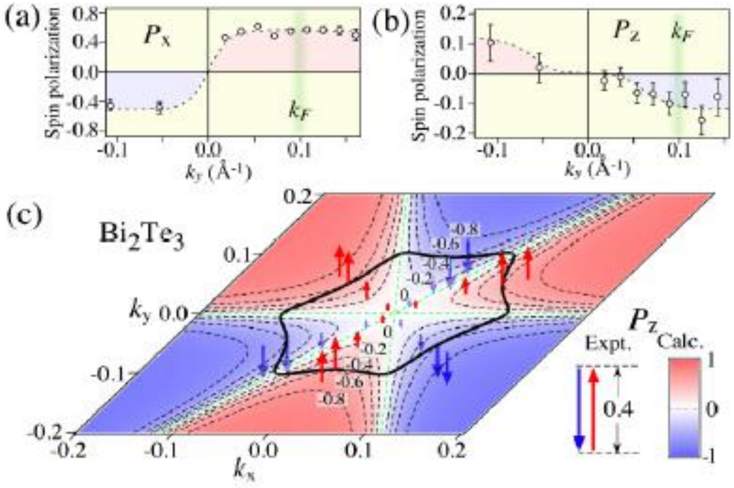

Figure 4.6 Out-of-plane spin component in Bi2Te3 measured by spin-ARPES. Adapted from [6].

The out-of-plane spin-component has been measured by spin-ARPES in Bi_2Te_3 [Figure 4.6] but not in Bi_2Se_3 because of the small warping factor in this material.

4.4 CD-ARPES spectra

The data that are acquired using left and right circularly polarized light are shown in Figure 4.7. In order to see the difference of the two, vertical energy-momentum slices are presented. For the surface states above the Dirac point, the intensity of left circularly polarized light is stronger at negative momenta and weaker at positive momenta than that of right circularly polarized light. Such momentum dependence is reversed below the Dirac point although the difference is less obvious than that above the Dirac point. Furthermore, it is difficult to see any difference in the conduction bulk band.

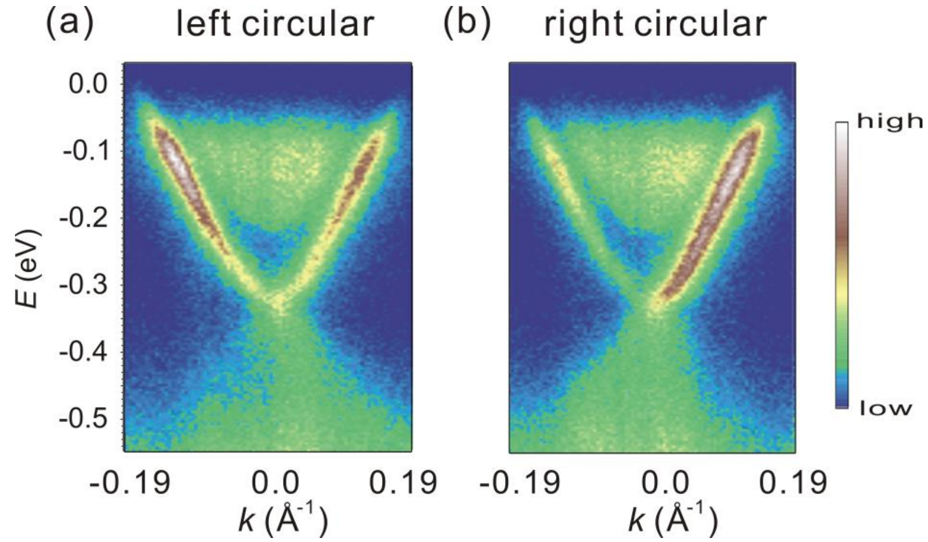

Figure 4.7 Energy-momentum cut from the intensity spectra along ΓK obtained by light with opposite helicity. (a) and (b) are obtained with left and right circularly polarized light respectively.

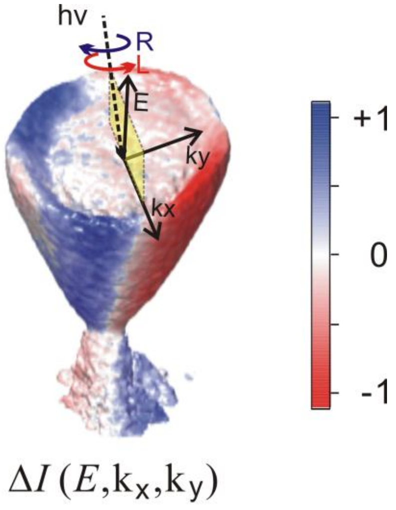

Figure 4.8 Difference spectra obtained by taking the difference between spectra taken with left and right circularly polarized light.

These differences can be seen more globally in the difference intensity spectra $\Delta I(E, k_x, k_y)$ that is obtained by taking the difference between the intensity spectra of left and right helicity light. We can see from Figure 4.8 that the difference is zero along the photon incidence plane, which is aligned to the crystal mirror plane ΓM of Bi_2Se_3. The difference spectrum is antisymmetric about the photon incident plane and the difference reverses sign across the Dirac point. The bulk states give no difference as we have seen in the intensity spectra in Figure 4.8. Furthermore, at energies above and away from the Dirac point, there is a patch of negative difference on the positive difference side and vice versa.

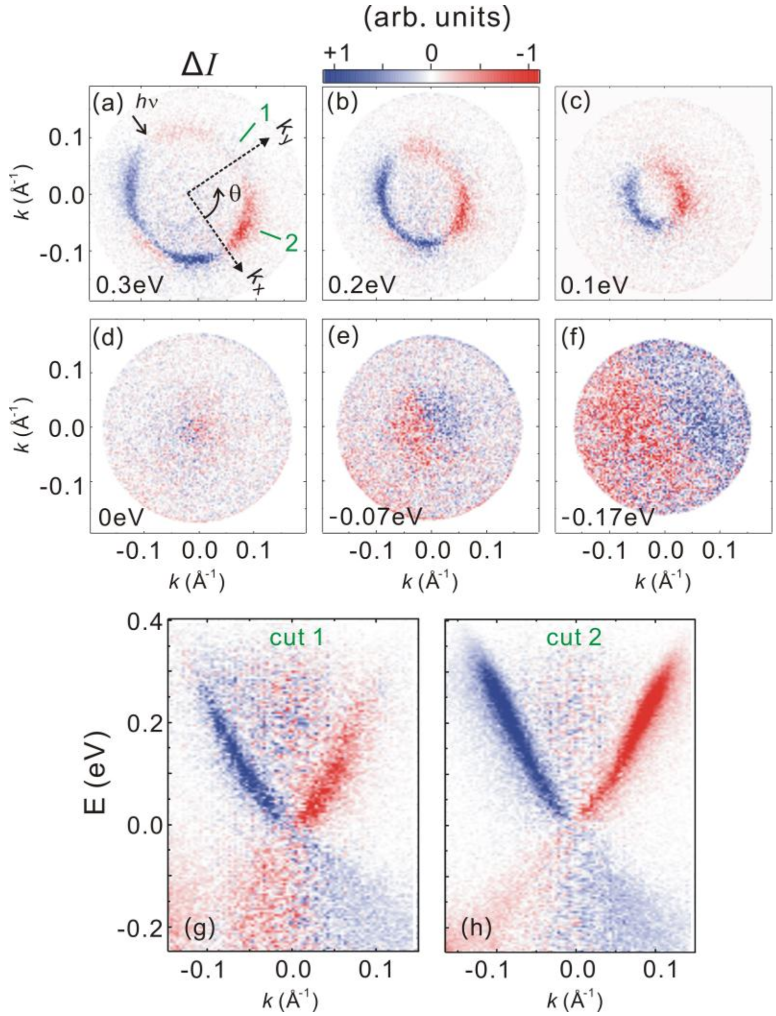

Figure 4.9 Cuts through the difference intensity spectra. (a)-(f) are constant energy cuts at various energies. (g) and (h) are energy-momentum cuts along the direction labeled by the green lines in (a).

To see how such patterns develop with energy, we take constant energy slices through the difference intensity spectrum. As shown in Figure 4.9, the difference is quite uniform within 0.1 eV above and below [Figure 4.9 (c) and (e)] the Dirac point [Figure 4.9 (d)]. For above the Dirac point, the difference starts to diminish along k_y beyond this energy range [Figure 4.9 (b)] and develops into the opposite sign at 0.3 eV above the Dirac point [Figure 4.9 (a)]. These trends are confirmed in the energy-momentum cuts [Figure 4.9 (g) and (h)] along cut 1 and cut 2 labeled in [Figure 4.9 (a)]. However, below the Dirac point such pattern does not appear [Figure 4.9 (f)]. Rather, the difference fills up the momentum space occupied by the bands that have both surface and bulk character.

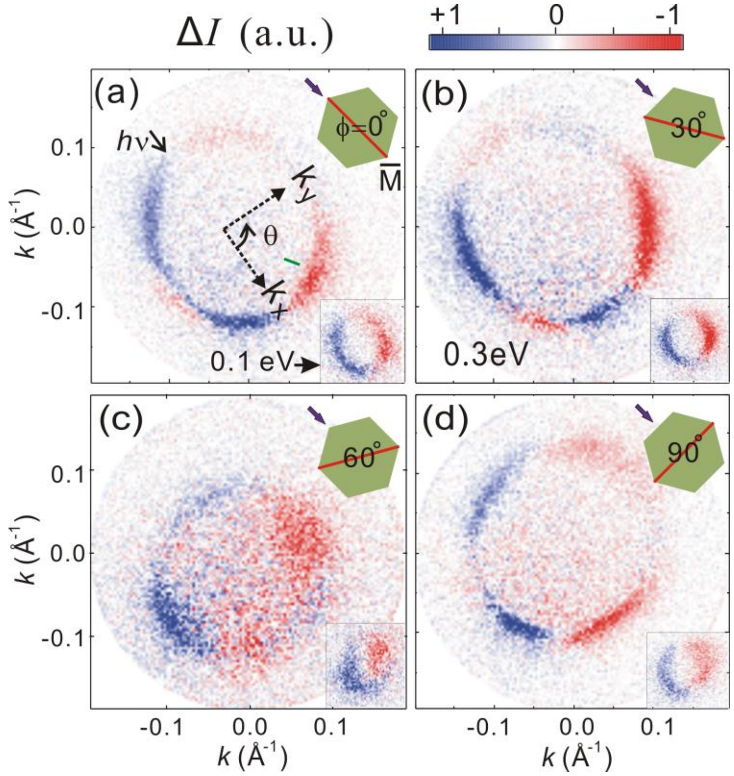

Figure 4.10 Constant energy slices of the difference spectra at various sample rotation angle at 0.3 eV above the Dirac point. The insets show the cuts at 0.1 eV for the same set of angles.

To investigate where the circular-dichroism patterns come from, we compare data taken at various sample in-plane rotation angle ϕ with respect to the photon incident plane. As can be seen from Figure 4.10, such pattern changes depending on angle ϕ. At 0.1 eV above the Dirac point, the CD difference spectra does not change as the sample is rotated and the difference always vanishes at the photon incident plane [Figure 4.10 insets]. However, at 0.3 eV above the Dirac point, the difference spectra changes dramatically with ϕ. The difference only vanishes along the photon incidence plane when the mirror symmetry plane of the crystal ΓM is aligned with it [Figure 4.10(a) and (c)]. There is some periodic modulation as a function of angle θ around the energy contour, which is reminiscent of the predicted out-of-plane spin component in the presence of hexagonal warping because it has a three-fold symmetry [Eq. 4.11].

The connection between the CD spectra and the spin texture can be further seen from Eq. 4.7. The CD spectra is a linear combination of both the in-plane x component $\langle s^x \rangle_{\boldsymbol{k}}$ and the out-of-plane component $\langle s^z \rangle_{\boldsymbol{k}}$. Since they have different rotational symmetry, their linear combination changes as the sample is rotated, explaining the different difference spectra at various ϕ.

4.5 Extracting spin texture from CD-ARPES

In order to extract the spin components $\langle s^x \rangle_{\boldsymbol{k}}$ and $\langle s^z \rangle_{\boldsymbol{k}}$ independently from the CD-ARPES spectra, we consider the symmetry property of the trigonal lattice of Bi_2Se_3, as can be seen from Figure 4.11. Considering both the three-fold rotational symmetry and the time-reversal symmetry, $\langle s^z \rangle_{\boldsymbol{k}}$ changes sign upon 60 degree rotation. Whereas for $\langle s^x \rangle_{\boldsymbol{k}}$, it is even under 60 degree rotation because it is isotropic. As a result we can use the linear combination of the difference spectra at $\phi = 0°$ and $\phi = 60°$ to obtain $\langle s^x \rangle_{\boldsymbol{k}}$ and $\langle s^z \rangle_{\boldsymbol{k}}$ independently. And we can use the difference spectra at $\phi = 30°$ and $\phi = 90°$ to obtain $\langle s^y \rangle_{\boldsymbol{k}}$. These are summarized as

$$\begin{gathered}\langle s^x \rangle_{\boldsymbol{k}} = \Delta I_{\boldsymbol{k}}(\phi = 0) + \Delta I_{\boldsymbol{k}}(\phi = 60) \\ \langle s^y \rangle_{\boldsymbol{k}} = \Delta I_{\boldsymbol{k}}(\phi = 30) + \Delta I_{\boldsymbol{k}}(\phi = 90)\end{gathered} \qquad \textbf{4.12}$$

$$\langle s^z \rangle_{\boldsymbol{k}} = \Delta I_{\boldsymbol{k}}(\phi = 0) - \Delta I_{\boldsymbol{k}}(\phi = 60)$$

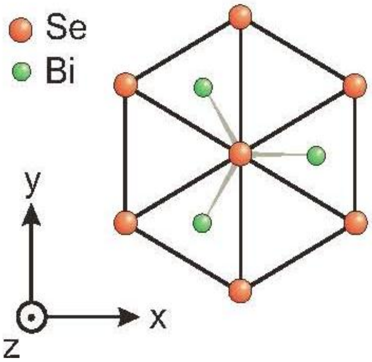

Figure 4.11 Trigonal crystal structure of Bi_2Se_3

Using Eq. 4.12, we obtain all three spin components as shown in Figure 4.12 Three spin components from the circular-dichroism difference spectra. All three spin components reverse sign across the Dirac point. Furthermore, at going from any $\boldsymbol{k}$ to $-\boldsymbol{k}$, the sign is also reversed, in observance of time-reversal symmetry. The in-plane spin polarization show more features whereas the out-of-plane component gets stronger as energy increases away from the Dirac point.

To better investigate such energy dependence, we take slices through the radial-integrated spin maps at $\pm 0.1\ eV$ from the Dirac point. As shown in Figure 4.13(a) and (b), the in-plane components $\langle s^x \rangle_{\boldsymbol{k}}$ and $\langle s^y \rangle_{\boldsymbol{k}}$ have a sinusoidal form close to the Dirac point and the phases shift by π for above and below the Dirac point. In contrast, $\langle s^z \rangle_{\boldsymbol{k}}$ is very weak at the energies close to the Dirac point so that its periodicity cannot be determined [Figure 4.13(c)].

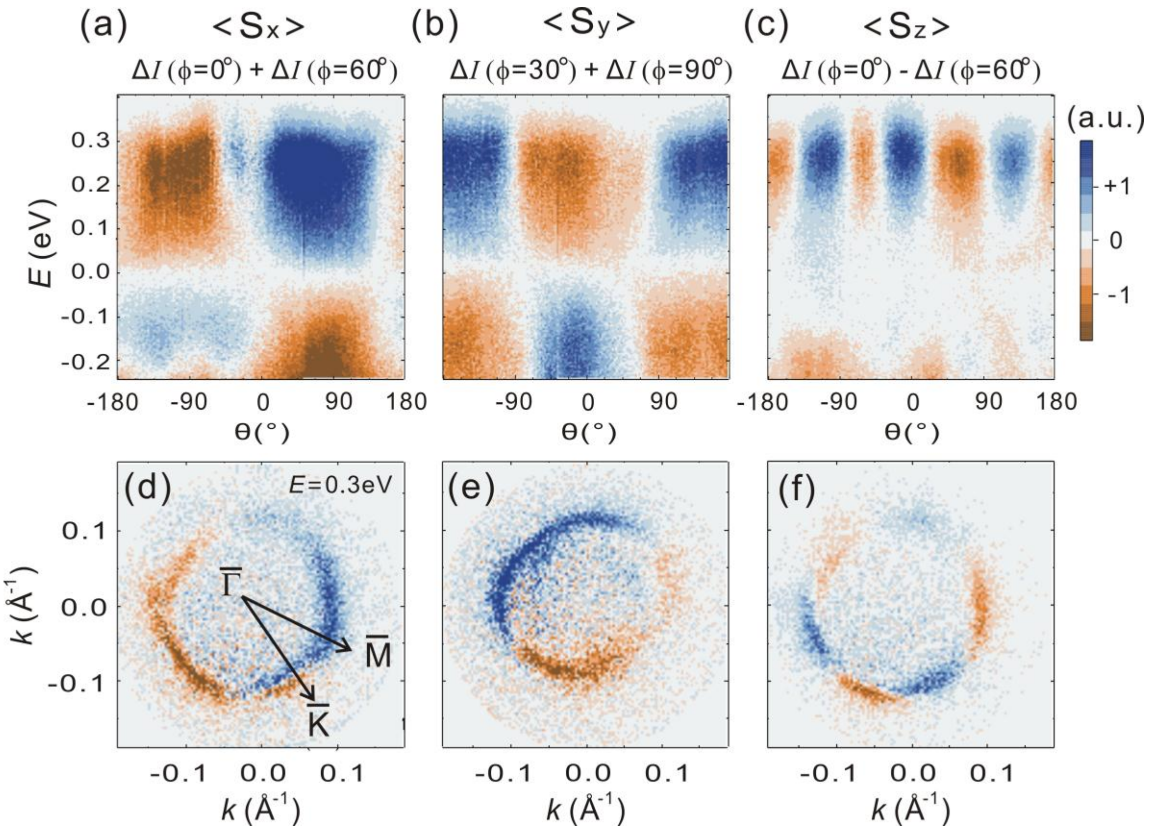

Figure 4.12 Three spin components from the circular-dichroism difference spectra. (a)-(c) are the maps of the spin polarization integrated radially over the surface states as a function of energy and in-plane angle θ. (d)-(f) show the constant energy cuts 0.3 eV above the Dirac point through the obtained $\langle s^x \rangle_{\boldsymbol{k}}$, $\langle s^y \rangle_{\boldsymbol{k}}$ and $\langle s^z \rangle_{\boldsymbol{k}}$ components.

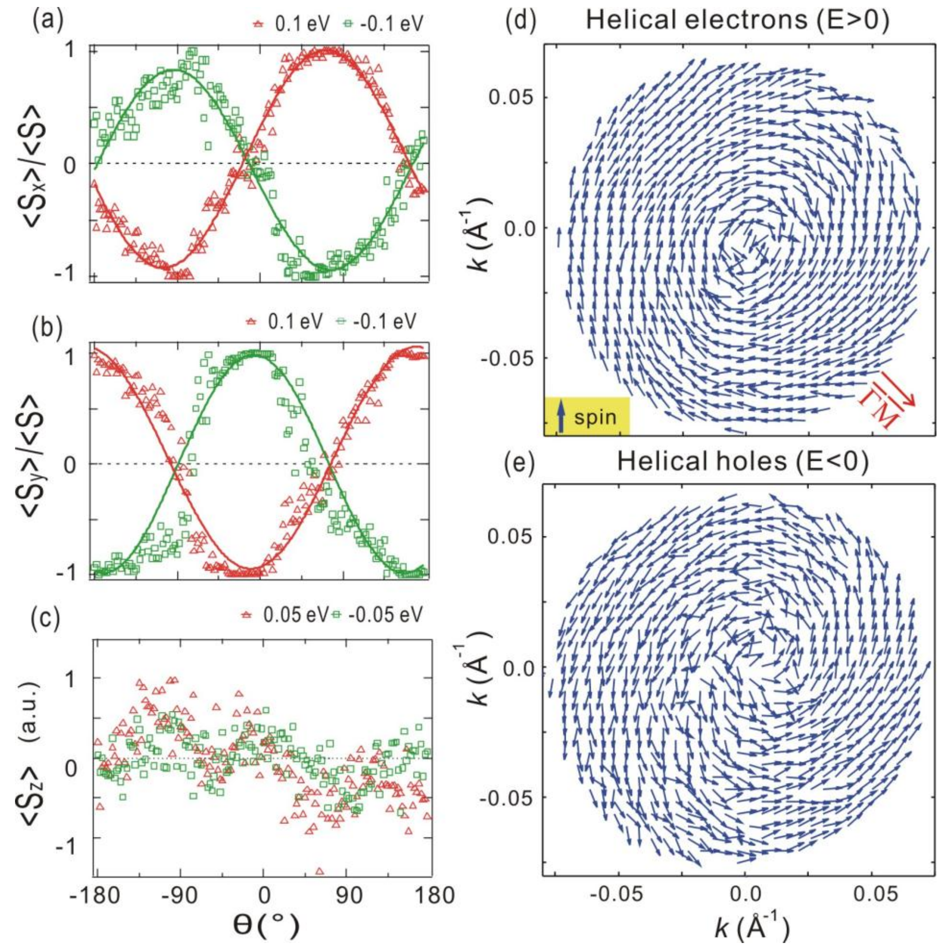

Figure 4.13 Spin polarization in the ideal helical regime. (a)-(c) Spin polarization as a function of angle around the constant energy contour radially integrated over the surface states at ± 0.1 eV. (d) and (e) are the projections of spin vectors in the range of ± 0.1 eV from the Dirac point. Positive and negative energies are separated into (d) and (e) to show the helical spin texture of topological insulators.

In order to visualize the in-plane spin texture close to the Dirac point, we combine the in-plane spin vector ($\langle s^x \rangle_{\boldsymbol{k}}, \langle s^y \rangle_{\boldsymbol{k}}$) within $\pm 0.1\ eV$ from the Dirac point but separate the positive energy (electron) from the negative energy (hole), as shown in Figure 4.13(d) and (e). We can see for the electrons, the spin vectors form a helical structure in the momentum space with a clockwise sense of rotation. Combining with the negligible $\langle s^z \rangle_{\boldsymbol{k}}$ magnitude in this regime, these observations are consistent with the perpendicular spin-momentum locking under the $\boldsymbol{k} \cdot \boldsymbol{p}$ theory. The sense of rotation is reversed in the hole side, in consistent with time-reversal symmetry. Furthermore the alignment of the spins is not as ordered as the electron side [Figure 4.13(e)], suggesting strong surface-bulk interaction below the Dirac point.

The spin polarization farther away from the Dirac point is quite different from the ideal helical picture as shown in Figure 4.13. At 0.3 eV above the Dirac point [Figure 4.14(a)], we can see the $\langle \mathrm{s}^{\mathrm{z}} \rangle_{\mathrm{k}}$ component shows a clear three-fold symmetry as predicted by Eq. 4.11. By comparing with the Fermi surface, we can see that $\langle \mathrm{s}^{\mathrm{z}} \rangle_{\mathrm{k}} = 0$ at six M points and reaches maximum or minimum at the Γ points, which is consistent with the spin-ARPES result on Bi_2Te_3.

In order to see how $\langle \mathrm{s}^{\mathrm{z}} \rangle$ evolves as a function of energy, we obtain the magnitude of $\langle \mathrm{s}^{\mathrm{z}} \rangle$ by fitting $\langle \mathrm{s}^{\mathrm{z}} \rangle(\theta)$ to Eq. 4.11 at all the energies. The magnitude $\langle \mathrm{s}^{\mathrm{z}} \rangle^0$ is plotted as a function of energy as the green trace in Figure 4.14 Deformed spin texture. Then we fit $\langle \mathrm{s}^{\mathrm{z}} \rangle^0(E)$ using the following equation:

$$\langle \mathrm{s}^{\mathrm{z}} \rangle^0(E) = \frac{1}{\sqrt{1 + [k(E)\beta]^{-4}}} \qquad \textbf{4.13}$$

where $\beta \equiv \sqrt{\lambda/\mathrm{v}}$. For Bi_2Se_3, the hexagonal distortion of the dispersion is relatively small, so we approximate the dispersion as $\mathrm{k(E)} \sim \mathrm{E}/\mathrm{v_F}$ over the energy range of 0 ~ 0.3 eV. $\langle \mathrm{s}^{\mathrm{z}} \rangle^0(E)$ can then be fitted with one free parameter $\mathrm{b} \equiv \beta/\mathrm{v_F}$. The fit [Figure 4.14(c) solid green] can very well capture the energy dependence of $\langle \mathrm{s}^{\mathrm{z}} \rangle^0(E)$. We subsequently extract λ by fitting Eq. 4.10 to the shape of the constant energy contour at the Fermi energy, which is shown in Figure 4.14(c) inset to overlap with the constant energy contour.

Because the combination of fits to $\langle \mathrm{s}^{\mathrm{z}} \rangle^{0}(E)$ and to $E_F(\theta)$ allows us to extract both v and $\mathrm{v_F}$, we can also solve for the correction to the Fermi velocity α that is also given by $\boldsymbol{k} \cdot \boldsymbol{p}$ theory as

$$\mathrm{v_F} = v(1 + \alpha k^2) \tag{4.14}$$

The obtained values for these parameters are listed in the following table.

E_F	0.3 eV
$\mathrm{v_F}$	$0.3\ \mathrm{eV \cdot Å}$
v	$0.47\ \mathrm{eV \cdot Å}$
λ	$125\ \mathrm{eV \cdot Å^3}$
α	$743\ \mathrm{Å^2}$

The in-plane component does not follow a simple sinusoidal form but develops some modulation as can be seen in Figure 4.14(b). There are two possible effects that can explain the origin of such modulation to the sinusoidal form of $\langle \mathrm{s}^{\mathrm{x}} \rangle$. The first is that there is a non-uniform out-of-plane canting of the spins around the Fermi contour that modulates the magnitude of the in-plane spin component. And the second is that the angle between the in-plane spin component and the momentum direction is modulated around the Fermi contour.

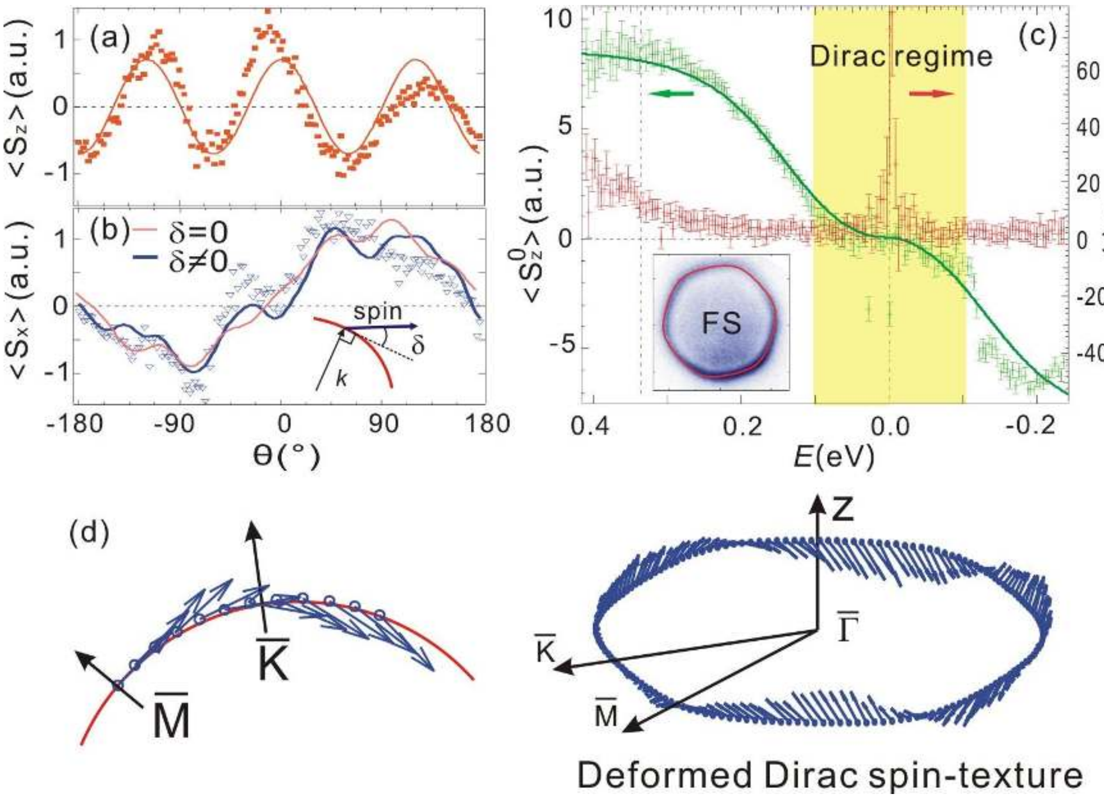

Figure 4.14 Deformed spin texture. (a) and (b) are out-of-plane and in-plane spin components respectively as a function of angle θ around the constant energy contour 0.3 eV above the Dirac point. The fittings to the data are described in the text. (c) shows the energy dependence of the out-of-plane spin magnitude and the in-plane deviation angle. (d) shows the spin vectors at 0.3 eV constructed from all three spin components.

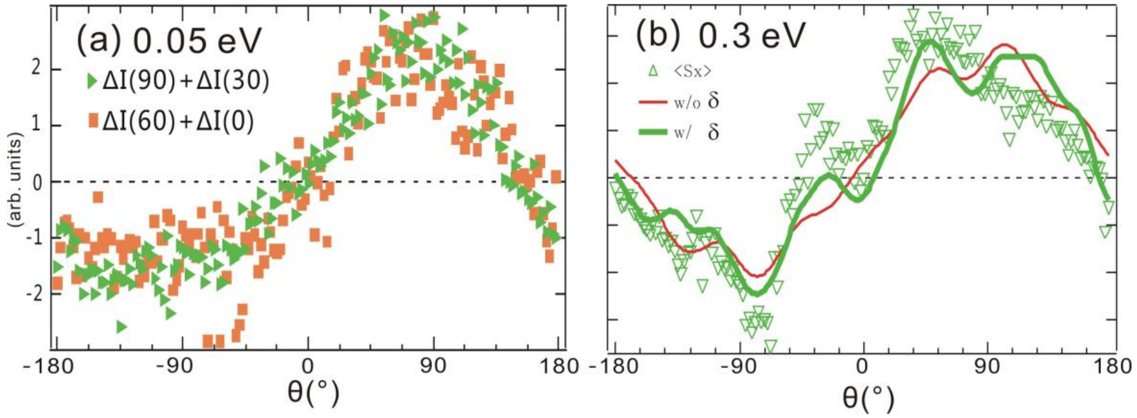

Figure 4.15 Fitting of the in-plane spin modulation. (a) shows the in-plane component as a function of angle θ taken 30° sample rotations apart at 0.05 eV above the Dirac point. (b) shows the in-plane component (green triangles) as a function of angle θ at 0.3 eV and two different fits with (green solid line) and without (red) considering the in-plane deviation angle δ.

To figure out which effect is relevant in Bi_2Se3, we study the symmetry properties of these two effects. The combination of C_{3v} crystal symmetry and time-reversal symmetry impose a six-fold rotational symmetry of the in-plane spin component and a three-fold rotational symmetry of the out-of-plane component. Mirror symmetry along the ΓM line dictates that whenever θ is along ΓM (namely at integer multiples of 60° then the total spin polarization $\langle \mathbf{S} \rangle$ must be perpendicular to the momentum. Taking these constraints into account allows us to write a general symmetry allowed expression for how $\langle \mathrm{s}^{\mathrm{x}} \rangle$ varies with θ:

$$\langle \mathrm{s}^{\mathrm{x}} \rangle(\theta) = s_0\sqrt{1-[\gamma\sin(3\theta+3\phi)]^2} \times \sin[\theta + \delta\sin(6\theta+6\phi)] \qquad \textbf{4.15}$$

where s_0 is the total spin, $\gamma \equiv s^z/s_0$, ϕ is the angle between ΓM and the in-plane wave vector of the incident photon and the sin 3θ dependence of $\langle \mathrm{s}^{\mathrm{z}} \rangle$ is confirmed in Figure 4.14(a). It is clear from this equation that even though the presence of $\langle \mathrm{s}^{\mathrm{z}} \rangle$ does modulate the magnitude of $\langle \mathrm{s}^{\mathrm{x}} \rangle$, it can only impose an envelope rather than create sharp kinks in the θ dependence of $\langle s^x \rangle$ near θ = 0◦ as observed by the poor fit to the ΔI(90◦) + ΔI(30◦) trace [Figure 4.15] when δ is set to zero. Another argument against an $\langle s^z \rangle$ origin is that if somehow $\langle s^z \rangle$ were the sole contribution, the fit would imply an out-of-plane canting angle of nearly 45◦ at E_F , which far exceeds theoretical predictions of around 10◦ [27]. Instead, letting δ be finite is the only way to explain these kinks. By fitting Eq. 4.15 to ΔI(90◦) + ΔI(30◦) at each energy over the entire Dirac cone, we obtain δ as a function of energy as well as the ratio γ. Our result shows that the maximum magnitude of $\langle s^z \rangle$ is less than 30% of s_0 at 0.4 eV, which corresponds to a much more realistic canting angle of less than 17◦.

4.6 Characterizing and eliminating false instrumental circular dichroism

It is known that ultra-high-vacuum chamber windows under stress and after bake-out are birefringent and can change the polarization of light. Other optics like mirrors can also cause change in the polarization of light. We characterize the effect of our vacuum chamber window and other optics after the variable wave-plate by following the same procedure that we use for checking the purity of circularly polarized light immediately after the quarter wave-plate. As shown in Figure 4.16, we shine the circularly polarized light through the window and normally onto the sample. We then reflect the light back through the window and the variable wave plate and check the polarization through a polarizer.

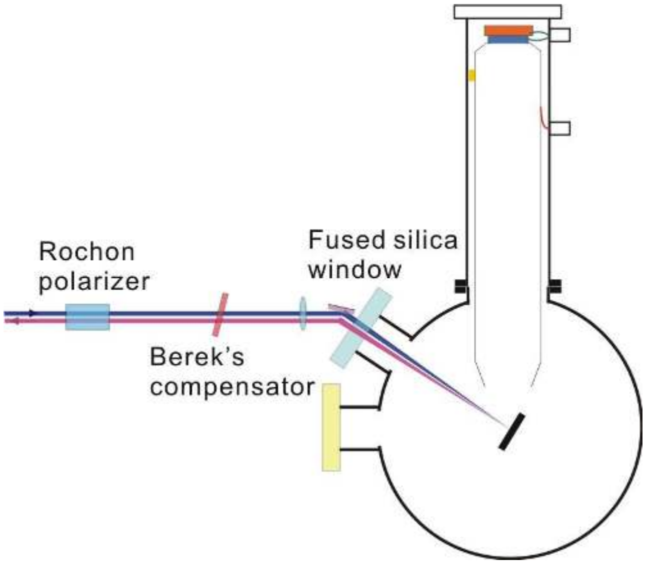

Figure 4.16 Optical diagram to use a Rochon polarizer and Berek compensator to compensate for the window birefringence.

We find that when the window is birefringent or any mirror causes Kerr rotation and/or ellipticity of light, it leads to a false CD pattern containing a $\sin(2\theta)$ component as shown in Figure 4.17. We compensate for the change of the polarization induced by the window by changing the variable wave plate until the reflected light is perpendicularly polarized with respect to the incident light. Only after this compensation is performed do we observe the correct CD patterns under various experimental configurations as is shown in the main text.

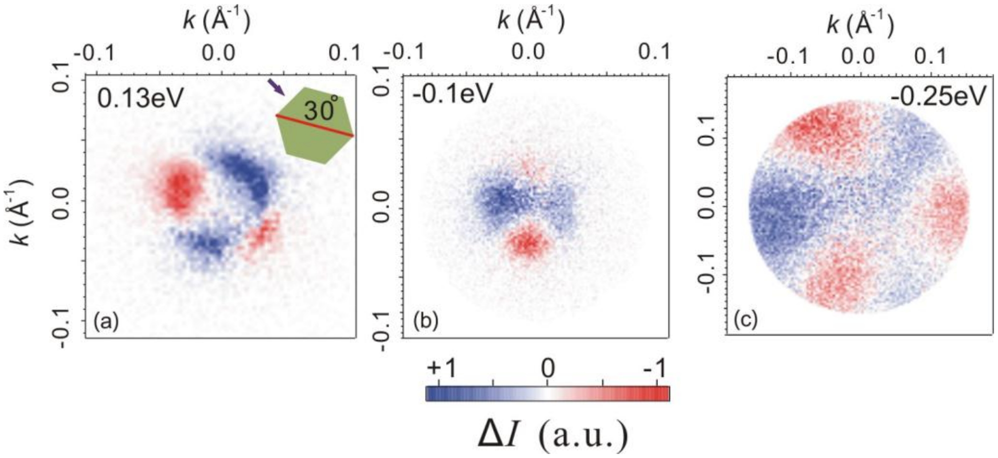

Figure 4.17 CD difference spectra when the birefringence from the vacuum window is not corrected. (a)-(c) show constant energy cuts at various energies above and below the Dirac point.

Chapter 5

TrARPES on topological insulators

5.1 Introduction

5.1.1 Motivation

As discussed in Chapter 1, electrons on the surface of a three-dimensional topological insulator are massless Dirac fermions with linear energy-momentum dispersion [23, 75-76]. Besides being a new class of materials, these electronic systems are promising for novel applications ranging from spin-based field effect transistors [77-80], ultrafast opto-spintronic devices [64] to high-speed quantum information processors [81-82], whose performance depends critically on the dynamics of hot carriers. Unlike the case in graphene [83-84], helical Dirac fermions in a TI interact not only with phonons but also with an underlying bulk reservoir of electrons [23]. Therefore it is important to understand separately their coupling mechanisms to each of these degrees of freedom. However, high frequency optical conductivity [85-86] and ultrafast optical experiments [87-88] do not directly separate bulk and surface signals nor do they distinguish different relaxation channels.

Time- and angle-resolved photoemission spectroscopy (TrARPES) is a powerful technique to study carrier dynamics with energy and momentum resolution. A recent TrARPES study has shown that persistent surface carrier population in a TI can be induced by photo-excitation [89]. In the following sections, we focus on disentangling different relaxation channels following photo-excitation over a range of electron doping suitable for device applications. Analysis of the TrARPES spectra enables us to separately obtain temperature and chemical potential relaxation of both surface and bulk. Our data reveal that interband inelastic electron-electron (e-e) scattering is suppressed and surface-to-bulk coupling is mediated entirely by phonons. At low lattice temperature, this latter scattering channel turns off and we observe that the surface temperature decay rate scales as a power law with doping indicating acoustic phonon assisted cooling of 2D Dirac fermions.

5.1.2 Concurrent work

The previous work on using TrARPES to study the prototypical topological insulator Bi_2Se_3 [89] has focused on the p-doped samples where the surface states are not occupied prior to photoexcitation. This work focuses on the photoexcitation pathway of the pump-probe process. It has identified the first image potential state, which may be of interest because of the proposed surface image magnetic monopoles in TI. It has also found a persistent bulk and surface carrier population.

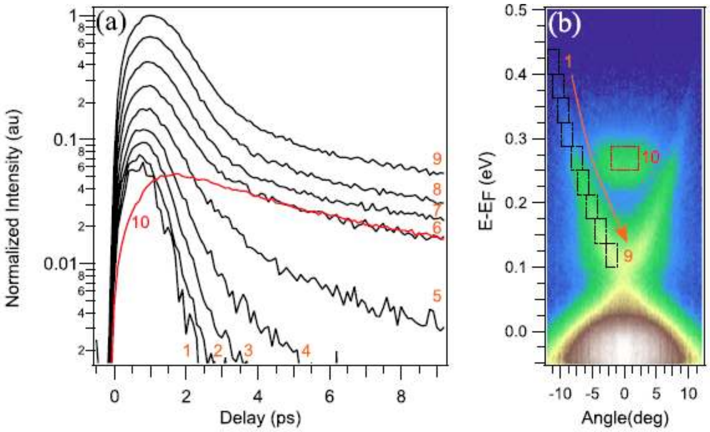

Figure 5.1 TrARPES on p-doped Bi2Se3 studied by Sobota *et al.* has focused on p-doped materials.

Hajlaoui et al. [90] have also performed a study on another prototypical topological insulator Bi_2Te_3 using TrARPES . They find that the thermalization of the surface states is initially determined by interband scattering from the bulk conduction band, lasting for about 0.5 ps; subsequently, few picoseconds are necessary for the Dirac cone nonequilibrium electrons to recover a Fermi-Dirac distribution, while their relaxation extends over more than 10 ps.

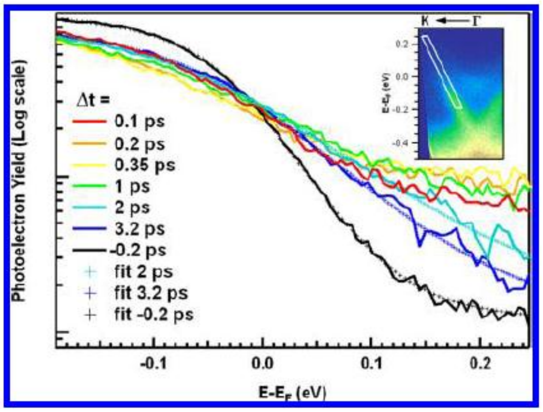

Figure 5.2 TrARPES on Bi$_2$Te$_3$ studied by Hajlaoui *et al.* has focused on the thermalization process of the photoexcited electrons.

5.2 TrARPES spectra

In our time-resolved ARPES study of topological insulators, we focus on the carrier relaxation of electron doped samples. These samples are more suitable for device applications because the presence of surface states without photoexcitation. After photoexcitation with a 1.5 eV pulse, we use our TOF-ARPES setup to obtain intensity spectra $I(E, k_x, k_x, t)$ over the 3D data volume are obtained simultaneously at certain time delay *t* as described in Chapter 3.

We first investigate the spectra very high above the Fermi level to see the photoexcitation pathway. Because at energies very far away from the Fermi level, the electron lifetime is much shorter according to Fermi liquid theory, we focus on the spectra at $t = 0$ [Figure 5.3]. Energy-momentum cuts obtained at 300 K and 15 K are both shown in Figure 5.3(a)-(c). Surprisingly, the spectrum taken at 300 K [Figure 5.3(a)] looks very different from that taken at 15 K [Figure 5.3(b) and (c)]. There is electron population in a band from 0.5 eV to 0.8 eV [PB in Figure 5.3(a)] at 300 K but such population is absent in 15 K [Figure

5.3(b) and (c)]. Because all these spectra are taken at $t = 0$ and the electrons with higher energies have not decayed [Figure 5.3(b) and (c)], such behavior between two lattice temperatures suggests that the optical excitation is assisted by phonons, which is commonly seen in photoexcitation of semiconductors. As we will show later, phonons play an important role in the relaxation pathways of photoexcited electrons in topological insulators.

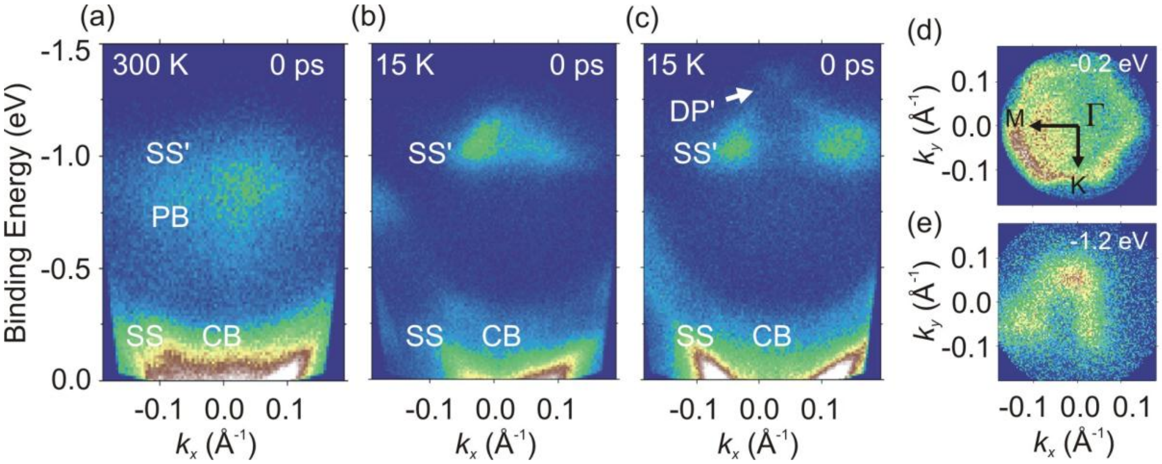

Figure 5.3 TrARPES spectra at time delay t = 0 ps. (a) - (c) Energy-momentum cuts of the spectra from the Fermi level to 1.5 eV above. (a) is obtained at 300 K whereas (b) and (c) are two perpendicular cuts taken at 15 K. (d) and (e) show constant energy cuts taken at 15 K at two different energies.

Furthermore, we can see from the spectra between 1 eV to 1.5 eV above the Fermi level, this band is very similar to the surface Dirac cone with a singular point [DP' in Figure 5.3(b) and (c)] at 1.3 eV, exactly 1.5 eV above where the Dirac point is. Constant energy cuts 0.2 eV above the Fermi level shows more hexagonally distorted surface contour. But the trigonal symmetry is more clearly seen in the photoexcited SS' state below DP' [Figure 5.3(e)]. The presence of a band reminiscent of the surface Dirac cone 1.5 eV above the original Dirac cone suggests that SS' is a virtual state in the pump-probe process.

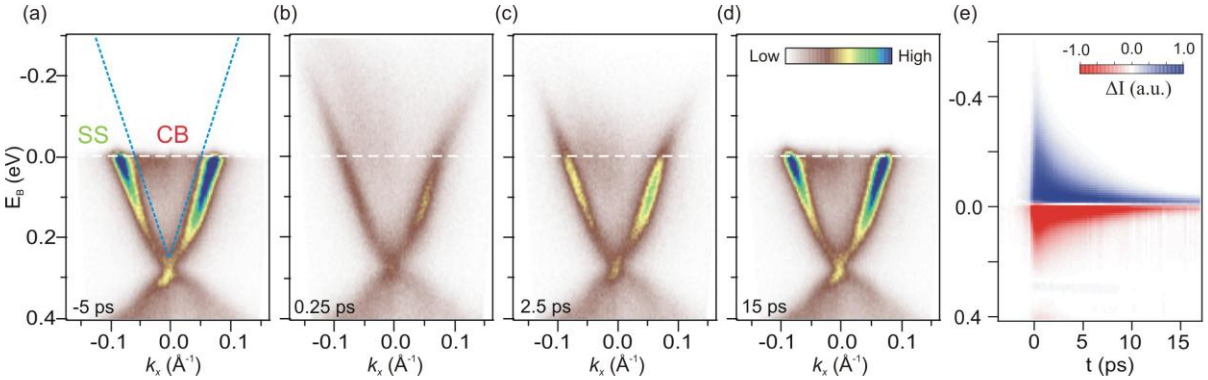

Figure 5.4 TrARPES spectra of Bi_2Se_3. (a)-(d) Energy-momentum spectra sliced through 3D data volume along $\mathbf{\Gamma M}$ direction at -5 ps (a), 0.25 ps (b), 2.5 ps (c) and 15 ps (d) taken at 15 K on an ED = 0.28 eV sample. (e) Momentum integrated difference spectra subtracting the spectrum at t = -5 ps. The blue dashed lines in (a) define the boundary between conduction bulk band (CB) and surface state (SS) for the analysis performed in the text.

To understand the relaxation dynamics of the states near the Fermi level, we show low energy ARPES spectra along the ΓM direction of the surface Brillouin zone at several time delays Figure 5.4(a)-(d). Figure 5.4(a) shows the surface states (SS) and conduction bulk (CB) band of a Bi_2Se_3 sample with the Dirac point E_D = 0.28 eV below E_F before the pump pulse arrives (t = -5 ps). The measured bandstructure is consistent with prior studies [25]. The ARPES spectra taken immediately after the pump excitation [Figure 5.4(b)] resemble a thermalized electron distribution at elevated temperature for both SS and CB. This hot distribution cools down progressively at longer time delays [Figure 5.4(c) and (d)]. However, it can be seen from the difference of momentum integrated spectra $\Delta I(E,t) = I(E,t) - I(E,t = -5\text{ ps})$ that the equilibrium has not been reached within the measurement time window [Figure 5.4 (e)].

5.3 Fitting of TrARPES spectra

In order to quantitatively describe the relaxation dynamics of the hot bulk and surface populations in Figure 5.4, we separately analyze the spectral intensities for the surface and the bulk. Figure 5.5(a) shows $I(E, t)$ for SS and CB at t = 0.25 ps obtained in their respective energy-momentum region [Figure 5.4(a)].

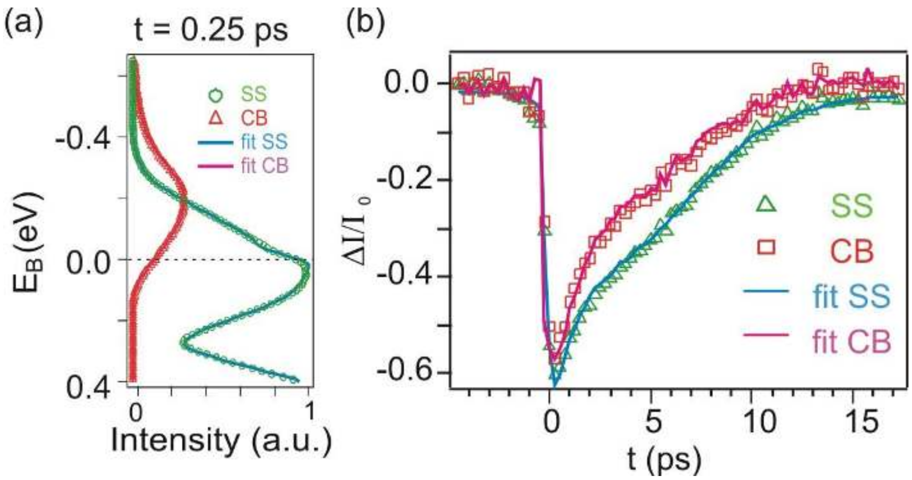

Figure 5.5 Momentum integrated spectra for surface and bulk states. (a) Momentum integrated spectra for SS (green) and CB (red) and their respective fits (purple and orange lines) at t = 0.25 ps for the data shown in Figure 5.4(b) Constant energy slices of the difference spectra as a function of t at 0.1 eV for the same data and fit. The spectra are normalized over the pre-pump intensity $\mathbf{I_0} = \mathbf{I}(\mathbf{t} = -\mathbf{5\ ps})$.

We fit $I(E, t)$ for both SS and CB with the following equation [28, 43] to extract their respective electronic temperatures $T_e(t)$ and chemical potentials $\mu(t)$ as a function of time:

$$I(E, t) = \int_{-\infty}^{\infty} d\epsilon\, [f_{FD}(E, T_e(t), \mu(t)) \times D(E)] G(E - \epsilon, w(t)) \qquad \mathbf{5.1}$$

Here $A(t)$ is a scaling factor [28, 43], f_{FD} is the Fermi-Dirac distribution, $G(E,w)$ is a Gaussian function with energy independent width w that includes the instrumental resolution and time-dependent broadening due to increased scattering rate after photo-excitation [33, 91-92]. The time independent D is a product of density of states (DOS) and photoemission matrix element [20].

The reason to use Eq. 5.1 to fit the momentum integrated spectra is because it is a standard equation to describe the momentum-integrated photoemission spectrum that is proportional to the product of the Fermi-Dirac distribution and the density of states, convolved with a broadening term $G(E,w)$ [20]. There are four essential fitting parameters at each time point. $A(t)$ is to account for the photocurrent fluctuation and reduced spectral weight in the observed energy-momentum volume after photoexcitation. $T_e(t)$ and $\mu(t)$ determines the width and the position of the Fermi edge. $w(t)$ is the parameter to account for the energy resolution and spectral broadening due to increased scattering rate after photoexcitation [43]. In general, such broadening might be energy dependent. Here we are only interested in the temperature and chemical potential so we approximate by a constant $w$for all energy and do not separate the resolution part and broadening part. Note that w is independent of $T_e(t)$ because it is mainly determined by the spectral broadening away from the Fermi level. Such broadening gives rise to the intensity at the Dirac point where DOS is zero.

$D(E)$ is obtained through a global best fit for all *t*. It is not a function of *t* and is chosen to be linear (parabolic) for SS (CB) initially and then iteratively optimized by minimizing χ^2 for all *t* [28-29, 43] $D(E)$ for SS at E_D and $D(E)$ for CB below the conduction band minimum are fixed to be 0. $D(E)$ typically converges in less than four iterations.

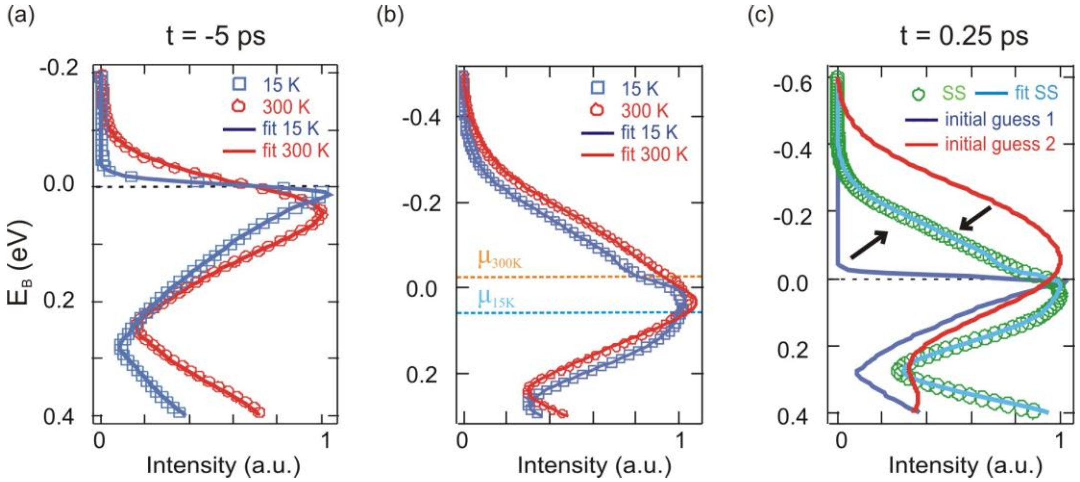

Figure 5.6 Surface state spectra with different sets of parameters. (a) is the data (markers) and fit (lines) at t = -5 ps. (b) shows the spectra of SS at 0.25 ps and CB at 0.75 ps. (c) shows the t = 0.25 ps spectra of SS. The purple and the red traces show the completely different initial guesses used to obtain the best fit (cyan).

To further prove that the parameters are not interdependent, we show two different fits of the SS spectra at 15 K and 300 K before [Figure 5.6(a)] and after [Figure 5.6(b)] photoexcitation. The delay times in (b) are 0.25 ps for SS and 0.75 ps for CB, when their electronic temperatures are roughly the same. It is chosen because their chemical potentials can be compared directly [Figure 5.6(b) dashed lines]. The parameters yielded by the fittings are tabulated below in Table 5.1. We can see that the obtained electronic temperatures in (a) are very close to the lattice temperatures which are 20 times different; whereas the values of E_F are similar and clearly do not depend on the values of T_e. On the other hand, the temperatures in (b) are similar because they are mostly determined by the excitation laser fluence; whereas the difference in chemical potentials captures the clear shift in the leading edge in [Figure 5.6(b)].

	(a) 15 K	(a) 300 K	(b) 15 K	(b) 300 K
T_e	18.3 ± 4.5 K	289 ± 1.6 K	1006.5 ± 3.2 K	1056.3 ± 6.2 K
E_F	-1 ± 0.01 meV	4 ± 0.4 meV	61.1 ± 1.8 meV	-23.2 ± 2.5 meV
w	14.9 ± 4.6 meV	24.2 ± 1.8 meV	40.2 ± 2.2 meV	29.1 ± 1.9 meV

Table 5.1

In Figure 5.6(c), we show two different sets of initial guesses we use for obtaining the fits. The best fits always converge to the same set of parameters regardless of the distinctively different initial parameters used, suggesting that the best fits do not locate in a local minimum and therefore the solution is unique.

Both the SS and CB fittings agree very well with data for all t as shown in Figure 5.5 and Figure 5.6. They have successfully captured the different dynamics of SS and CB into $T_e(t)$ and $\mu(t)$, which will be the basis for the discussion in the rest of the chapter.

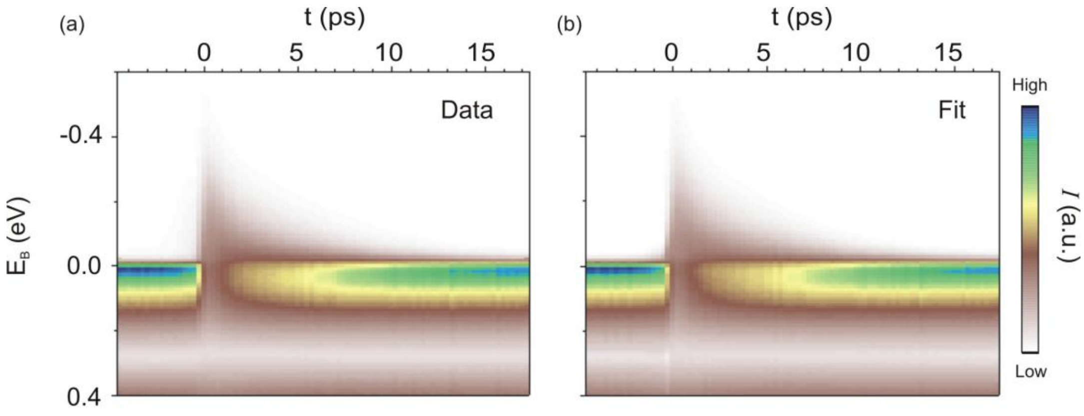

Figure 5.7 Agreement between data and fit of the momentum integrated intensity spectra. (a) and (b) show the color map of the data and fit spectra with SS and CB spectra combined. The data is obtained for ED = 0.28 eV sample at 15 K and the fit is performed on the same data set.

The fits are obtained for both SS and CB momentum integrated intensity spectra [Figure 5.5] and summed to get the total intensity spectrum at each *t* point. They are then merged together into a time-resolved intensity spectra as shown in Figure 5.7(b). We can see that the fit looks almost identical to the data except in the region -2 ps < *t* < 0, when the 6.2 eV probe pulse precedes the 1.55 eV pump pulse and excites the system into an image-potential state [3].

The fact that both SS and CB populations can be described by Fermi-Dirac distributions at *t* = 0.25 ps [Figure 5.5(a)] suggests that intraband thermalization of SS and CB electrons is established within the instrumental resolution time (~ 200 fs). Earlier work [89] using TrARPES to study Bi_2Se_3 surface electron dynamics also find them thermalized on the picosecond time scale of our study.

5.4 Electronic temperature and chemical potential dynamics

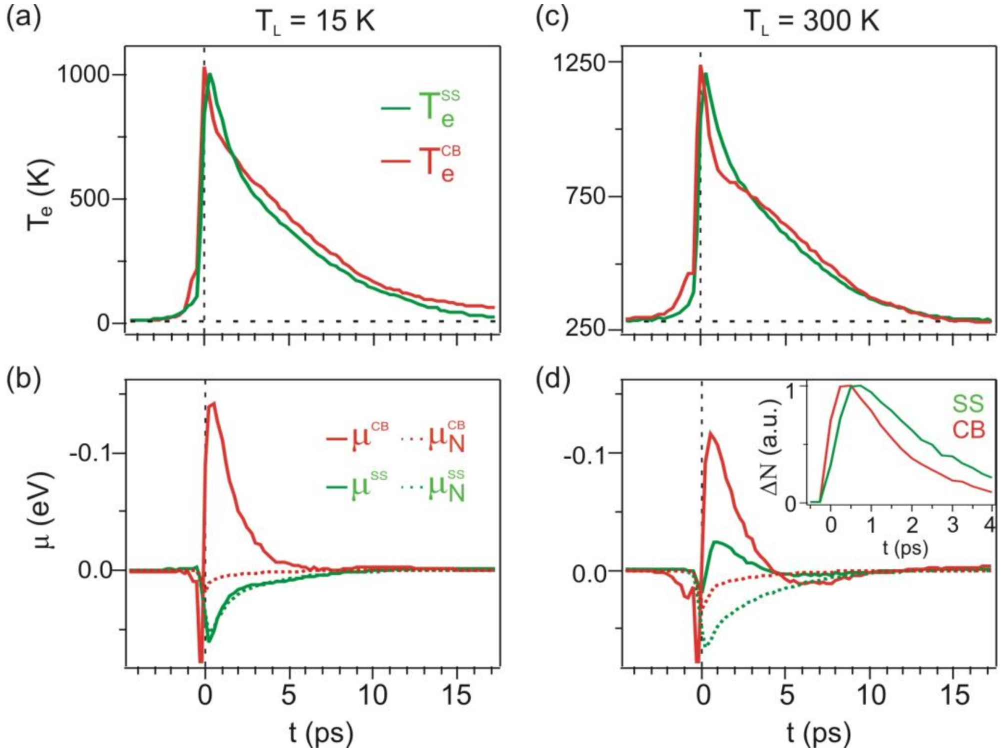

Figure 5.8 Electronic temperature and chemical potential dynamics for high doping sample. (a) Electronic temperature $\mathrm{T_e}$ and (b) chemical potential μ for SS (green) and CB (red) at lattice temperature $\mathrm{T_L}$ = 15 K. (c) and (d) are at $\mathrm{T_L}$ = 300 K. The green dashed traces $\mu_{\mathrm{ss}}^{\mathrm{N}}$ are the SS chemical potential as a function of $\mathrm{T_e^{ss}}$ under constant particle number. The red dashed traces are $\mu_{\mathrm{CB}}^{\mathrm{N}}$ for CB. The change of particle number is shown in (d) inset. (The features before t = 0 are due to the processes where the roles of pump and probe are reversed, which is commonly seen in TrARPES [1-3].)

Figure 5.8 shows the obtained electronic temperatures and chemical potentials for both the SS and CB. We focus on the temperature first. As shown in Figure 5.8(a), SS (CB) temperature T_e^{SS} (T_e^{CB}) starts at the lattice temperature T_L = 15 K at t = -5 ps. The maximum temperature increase of ~ 1100K at t = 0 ps allows us to estimate an electron specific-heat coefficient γ of 2 mJ/mol·K^2 (assuming 50 nm penetration depth of the pump pulse [89]). The electronic temperature dynamics agrees very well with previous nonlinear optical studies of Bi_2Se_3 [87], as can be seen in Figure 5.9.

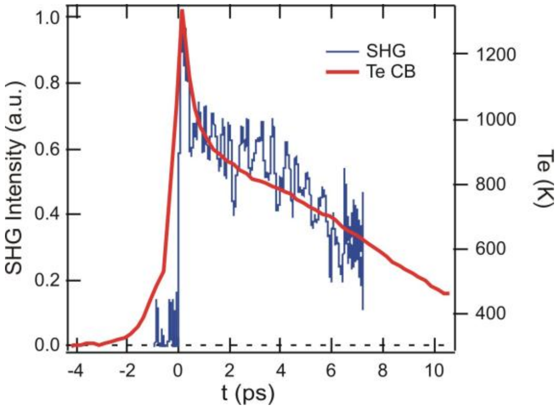

Figure 5.9 Electronic temperature and second harmonic generation time dependence of Bi_2Se_3. These two independent studies show that the bulk electron dynamics agree very well.

The analysis of the time dependence of the chemical potential reveals carrier population dynamics both within and between the bands. In general, chemical potential is a function of both temperature and particle number *N* [93]. In a static ARPES experiment, the chemical potential of the sample and that of the spectrometer are equal [20]. This is not the case after a femtosecond photoexcitation because electrons can be excited into different bands and it takes certain amount of time for them to relax and equilibrate with the reservoir again. Even when particle number is conserved in the system, the elevated electronic temperature after photoexcitation changes the chemical potential. This can be seen from the following equation that determines the particle number in a band:

$$N = \int_{-\infty}^{\infty} f_{FD}(E, T_e, \mu) DOS(E) dE \qquad \mathbf{5.2}$$

where *N* is the particle number; $f_{FD}(E, T_e, \mu)$ is the Fermi-Dirac distribution at temperature T_e, $DOS(E)$ is the density of states and *E* is binding energy. Since density of states is usually energy dependent, at a fixed $N = N_0$, when temperature changes the chemical potential has to change to conserve particle number. Using $DOS(E) \propto E$ for the surface states of a topological insulator and knowing T_e from our experiment, we can derive $\mu_N(t)$ at a fixed N_0. We note that, this large change of chemical potential is unique to the SS due to its linear dispersion. As for the CB band density of states, we use a square root function [93] which cuts off at the band minimum because of its parabolic dispersion. In the low doping regime where the CB band is not occupied before photo-excitation (E_D < 0.15 eV), $\mu_N(t)$ is fixed at E_F because $N_0 = 0$ [Figure 5.10(b) and (d) red dashed traces]. The actual particle number as a function of time can be straightforwardly calculated (up to a scaling factor) by substituting into Eq. 5.2 the temperature and chemical potential found from Fermi-Dirac distribution in Eq. 5.1.

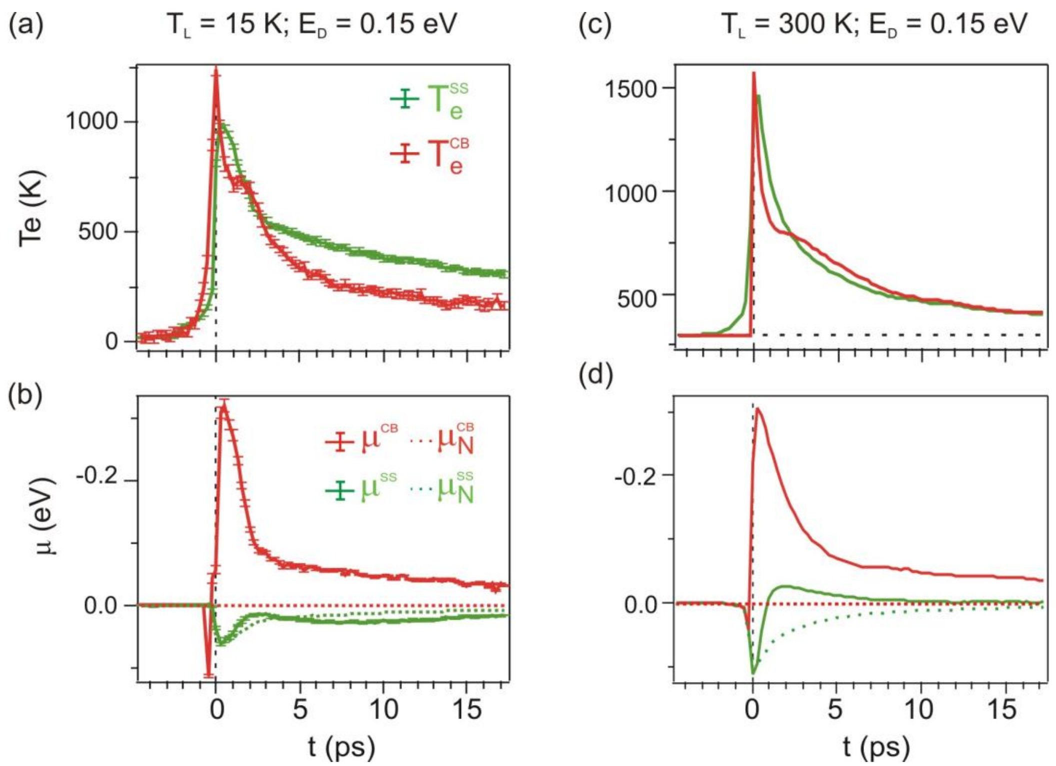

Figure 5.10 Electronic temperatures and chemical potentials of SS and CB as a function of t for a sample with ED = 0.15 eV at 15 K ((a), (b)) and 300 K ((c),(d)) lattice temperature. Green traces are for the surface state and red traces are for the conduction bulk band. Green and red dashed traces in (b) and (d) correspond to the chemical potential as a function of its electronic temperature when the particle number is fixed on the surface and conduction bulk band respectively (see text). Error bars of temperatures and chemical potentials from the fitting are shown in (a) and (b). Error bars for other data are similar or smaller.

Figure 5.10(b) and (d) show that for E_D = 0.15 eV sample μ^{SS} still overlaps with μ_N^{SS} at 15 K but is much higher at 300 K. Furthermore, Figure 5.10(a) and (c) show that SS and CB temperatures do not equilibrate at 15 K in the measured time window but do at 300 K. All these features are consistent with the observation of the main text on a high doping sample.

The SS and CB chemical potentials derived at fixed particle number N are plotted in Figure 5.8(b) along with the chemical potentials directly obtained by fitting our data to Eq. (1) (μ^{ss} and μ^{CB}). Remarkably, a good overlap between μ^{ss} and μ_N^{ss} as a function of t is observed at T_L = 15 K [Figure 5.8(b) green] indicating constant SS particle number N^{ss}. μ^{CB} is significantly higher than μ_N^{CB} [Figure 5.8(b) red], suggesting instantaneous N^{CB} increase upon photo-excitation. The increasing N^{CB} shows that photo-excitation from deeper valence bands primarily populates CB, consistent with a related study that shows bulk dominant direct optical transition [89]. This is shown in Figure 5.11. The fact that N^{ss} stays constant indicates that there is no net particle transfer from CB to SS.

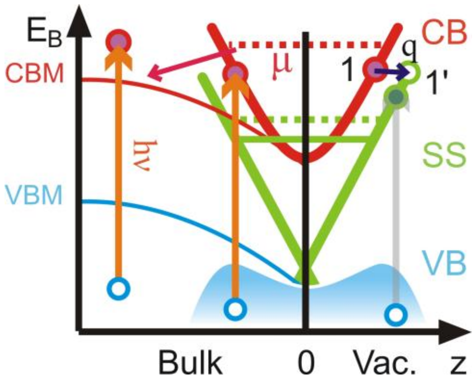

Figure 5.11 The photoexcitation process. The direct optical transitions are possible from the bulk states both at the surface and in the bulk with both the surface and bulk states as the final states. When the lattice temperature is high, bulk photo-carriers are scattered to the surface states by phonons. This mechanism reduces the chemical potential difference between surface and bulk states.

In order to understand whether the transfer of carriers between surface and bulk can happen at higher lattice temperature, we now investigate the chemical potentials and temperature dynamics at 300 K [Figure 5.8(c) and (d)]. The most striking feature is that μ^{ss} is much bigger than μ_N^{ss} [Figure 5.8(d)], indicating a strong increase of surface carrier density in contrast to 15 K [Figure 5.8(b)]. To find where the extra surface carriers come from, we notice μ^{CB} is lower at 300 K than at 15 K [Figure 5.8(b) and (d) solid red traces]. By calculating the change of particle numbers after photo-excitation of SS and CB (ΔN^{ss} and ΔN^{CB}), we see that the increase of ΔN^{ss} at 300 K has a slower rise time than ΔN^{CB} at 15 K [Figure 5.8(d) inset]. This shows that SS particle number increase is not due to direct optical transition. Rather it is a result of transfer from CB to SS through phonon scattering at elevated lattice temperature due to higher phonon-scattering rate above Debye temperature (θ_D = 182 K [94]) [95]. The evidence for such phonon-assisted CB-SS scattering can also be seen in the temperature dynamics [Figure 5.8(a) and (c)]. $\mathrm{T}_{\mathrm{e}}^{ss}$ and $\mathrm{T}_{\mathrm{e}}^{\mathrm{CB}}$ only equilibrate at 300 K within the probed time window, indicating that phonons scatter carriers, transferring energy and mediating the thermalization between SS and CB at 300 K.

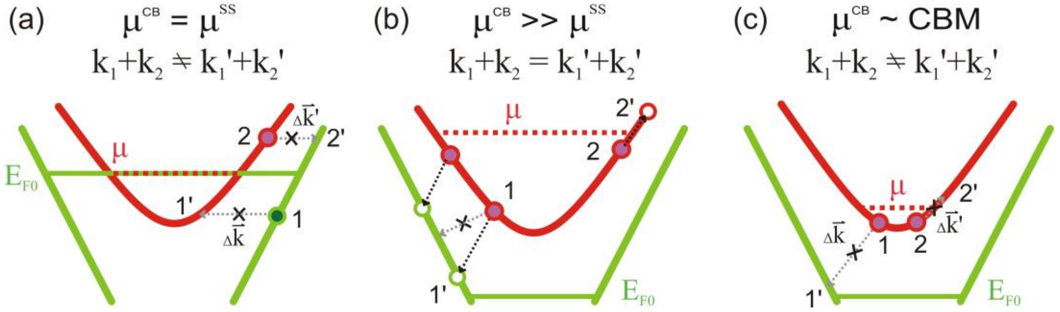

Figure 5.12 Interband inelastic electron-electron recombination rate depends on the chemical potential. (a) When surface and bulk have equal chemical potential, the kinematics constrains the thermalization between surface and bulk states. (b) When the bulk chemical potential is much higher, the Auger process thermalizes surface and bulk. (c) When bulk chemical potential is at the conduction bulk minimum, the Auger recombination is suppressed.

Since inelastic e-e scattering is mainly responsible for ultrafast thermalization [95] within a single band, the lack of thermalization between SS and CB at 15 K [Figure 5.8(a) and Figure 5.10(a)] suggests that inelastic e-e scattering time between SS and CB exceeds the measured time window. As shown in Figure 5.12, such suppression of interband inelastic e-e scattering is likely due to the kinematics constraints [96].

For high doping samples, even when bulk and surface chemical potentials are equal, the interband inelastic scattering is not likely to happen because the momentum conservation is difficult to be satisfied [Figure 5.12(a)]. This is because the distribution function of surface and bulk when their temperatures are different only allows the electrons above and below the chemical potential to scatter in the opposite direction. Because of the mismatch in the dispersion of the surface and bulk states, the momentum conservation cannot be satisfied. When the doping level is low [Figure 5.10(a)], the thermalization through interband inelastic e-e scattering is allowed to happened when the bulk chemical potential is very high owing to the large available phase space [Figure 5.12(b)]. This leads to a brief thermalization between the surface and bulk at 15 K at around *t* = 3 ps [Figure 5.10(a)]. However, the phase space diminished as the bulk chemical potential quickly approaches the conduction band minimum [Figure 5.12(c)] likely due to diffusion of carriers out of the surface layer [Figure 5.11]. The intraband inelastic e-e scattering is suppressed again and the surface and bulk electronic temperature decay independently [Figure 5.10(a)].

5.5 Doping dependence of the temperature dynamics

Having shown that interactions between SS and CB are suppressed at 15 K [Figure 5.8 (a) and (b)], we proceed to investigate their respective intraband cooling mechanisms. Because different mechanisms can be distinguished based on carrier density dependence, as demonstrated in other Dirac materials [97], we measure the intraband cooling dynamics of Bi_2Se_3 over a wide range of dopings. To vary the doping, we used samples from two different batches with high and low carrier concentrations along with surface doping effect [98-102]. We show the energy of the Dirac point for the sample after its surface is doped in Figure 5.13. The surface doping effect has been commonly observed in topological insulators such as Bi_2Se_3 [99, 101-102] and is attributed to either adsorption or moving of Se vacancies towards the surface [99-100].

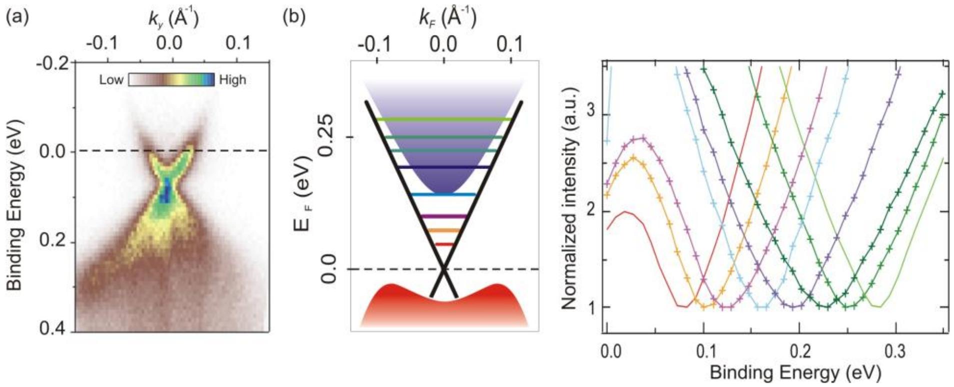

Figure 5.13 Surface doping effect. Bi_2Se_3 surface-doping effect tunes electron density and Fermi level. (a) Energy momentum slice through the $\mathbf{I}(\mathbf{E}, \mathbf{k_x}, \mathbf{k_y})$ spectra for low doping level sample with E_D = 0.07 eV above the Dirac point right after cleaving. (b) Momentum integrated spectra showing the shift of the Dirac point due to surface-doping over 24 hours. The Dirac point is lowered from 0.07 eV to 0.28 eV below the Fermi level (traces with markers). Red and green traces without markers correspond to the spectra of high and low doping samples right after cleaving. The intensities are normalized to the intensity at the Dirac point.

Figure 5.14(a) shows that the surface temperature has two decay components τ_1^{SS} and τ_2^{SS}. The fast-decaying component τ_1^{SS} is independent of E_D. This is consistent with optical phonon cooling, which is insensitive to doping as observed in graphene [103-104]. When the electronic temperature cools below ~ 600 K, the optical phonon cooling becomes less effective. Instead, the decay becomes dominated by a density dependent component τ_2^{SS} whose rate increases with electron doping [Figure 5.14 (a)]. In contrast, Figure 5.14(b) shows that bulk temperature dynamics is qualitatively different. The fast component $\tau_1^{CB} = 0.7 \pm 0.1$ps [Figure 5.14 (b)] matches with a previous ultrafast study, which has been attributed to an optical phonon mediated intraband cooling of CB [87]. The slow component τ_2^{CB} exhibits no discernable dependence on E_D [Figure 5.14 (b)].

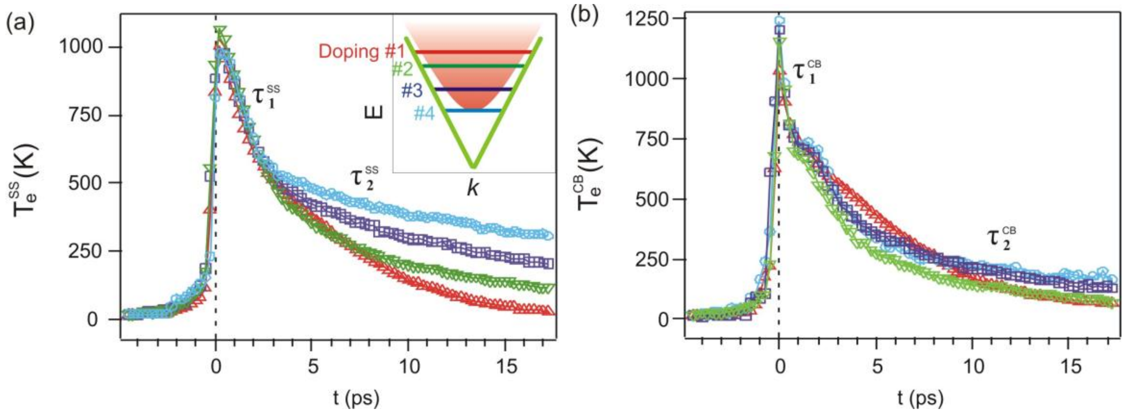

Figure 5.14 Surface and bulk electronic temperature dynamics at 15 K. Electron density dependent intraband cooling of surface Dirac fermions. (a) Electronic temperature as a function of t of surface electrons with different E_D at 15 K. Different colors corresponds to E_D in matching color in the inset. (b) T_{CB} at 15 K. Inset: Inverse cooling time of the slow component of T_e as a function of E_D at 15 K for SS (green triangles) and CB (red squares). $1/\tau_2^{SS} \sim {E_D}^3$ at 15 K.

We use the density dependence of the slow component to reveal its microscopic origin. We extract τ_2^{SS} through a biexponential fit of $\mathrm{T_e^{SS}}$ and plot it as a function of doping E_D in Figure 5.14(b) inset. Such exponential decay of the electronic temperature in a Dirac system has been previously predicted for graphene [97] and also observed in graphite [105] and recently Bi_2Se_3 [89]. The SS cooling rate scales as $\frac{1}{\tau_2^{SS}} \sim {E_D}^{3\pm0.5}$, which is in good agreement with the theoretical calculations of cooling of 2D Dirac fermions via acoustic phonons [97]. In stark contrast, $1/\tau_2^{CB}$ exhibits little dependence on doping, which agrees with theoretical predictions that acoustic phonon-mediated carrier cooling in 3D metals is density independent [52].

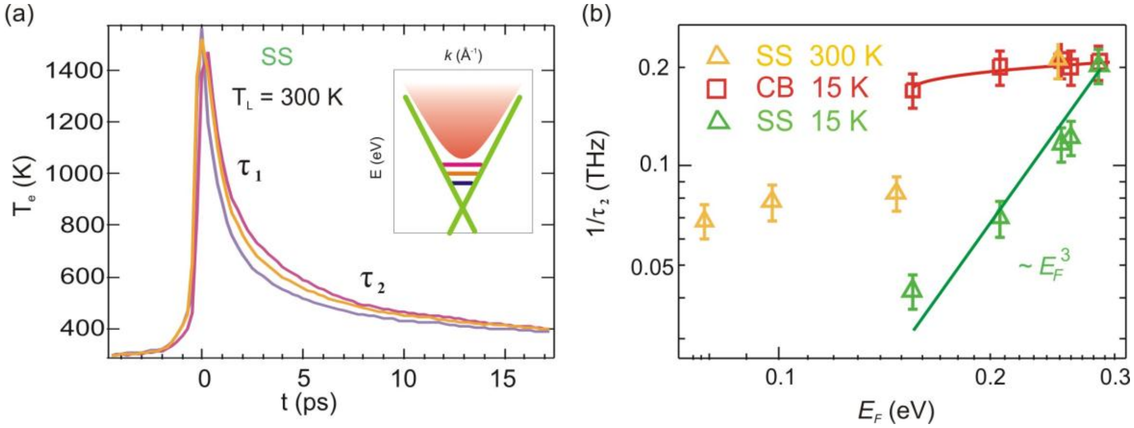

Figure 5.15 Slow component doping dependence. (a) Doping dependence of electronic temperature of SS at 300 K. The color of the trace matches the color of the Fermi level shown in the inset. Both the fast (τ_1) and slow (τ_2) components are slightly dependent on the doping. (b) $1/\tau_2$ obtained from biexponentially fit the electronic temperature.

To further see how coupling to the bulk will affect cooling of surface electrons, we compare the cooling dynamics at 300 K with various dopings [Figure 5.15]. Figure 5.15(a) shows that both the fast and slow component depends on the electron density. For the slow component, the dependence is not as dramatic as the effect at 15 K. This can be understood by considering mixing the density dependent $1/\tau_2^{SS}$ with the density independent $1/\tau_2^{CB}$ due to the phonon scattering at 300 K. This is quantitatively shown by the cooling rate $1/\tau_2$ at 300 K, which lies in between that of the SS and CB at 15 K [Figure 5.15(b)]. The fast component τ_1 is also density dependent [Figure 5.15(a)]. This is because different doping level scatters different portions of the bulk electrons with the surface states and the total relaxation rate $1/\tau_1$ is a weighted average of $1/\tau_1^{SS}$ and $1/\tau_1^{CB}$.

It is worth mentioning that in the low doping regime where $\mu \ll k_B T_e$, acoustic phonon cooling of Dirac fermions will be further suppressed and is predicted to have a different decay dynamics [97]. As a result, the doping dependence of the slow decay component may deviate from the power at low doping levels.

Chapter 6

Conclusions

This thesis describes a laser-based ARPES system with TOF electron spectrometer. The novel TOF spectrometer allows simultaneous acquisition of the energy-momentum spectra without rotating the sample. This capability allows direct analysis of the photoemission matrix element over the entire energy-momentum space. Using ultrafast laser as the light source for ARPES provides many benefits including better energy and momentum resolution and more bulk sensitivity than synchrotron light source. Furthermore, performing laser-pump ARPES-probe type experiments with ultrafast lasers extends ARPES to studying the dynamics of the electron system on a femtosecond time-scale.

By combining the TOF-ARPES technique with ultra-pure circular photon polarization, we observe circular-dichroism in the ARPES spectra of Bi_2Se_3 from the surface states and not from the bulk. Using a novel sample- rotation analysis, we resolve unusual modulations in the circular dichroism photoemission pattern as a function of both energy and momentum for the first time, which closely follow the predicted three-dimensional spin-texture. A direct connection between CD-ARPES and spin-orbit induced spin-textures is established through our microscopic theory of photoemission. Our results open the possibility to generate highly-polarized spin currents with circularly polarized light, which may be detected through transport or optical means [87]. The efficiency and high spin sensitivity of our technique suggest that CD-ARPES may be used as a vectorial spin mapping tool to detect small deviations from a π Berry's phase in magnetically doped topological surface states, or to study spin-orbit coupled materials in general.

Utilizing the capability of TrARPES to disentangle different degrees of freedom, we have directly visualized different scattering channels of surface and bulk electrons on a TI. At high temperature, phonons are largely responsible for scattering electrons between the surface states and the conduction bulk band. At low temperature, the coupling between surface and bulk is suppressed. We further reveal the surface cooling rate follows a power law dependence on the carrier density, which is a signature of acoustic phonon mediated cooling of 2D Dirac fermions. This suggests that by tuning to the charge neutrality point one can enter a regime where acoustic phonon scattering of Dirac fermions is completely eliminated and transport properties are determined solely by structural and chemical defects [77, 106-107]. An exciting possibility is the creation of long-lived hot photo-carriers that can be used for high-efficiency photothermoelectric applications [64, 108].

Bibliography

[1] *L. Perfetti, et al., "Ultrafast electron relaxation in superconducting Bi(2)Sr(2)CaCu(2)O(8+delta) by time-resolved photoelectron spectroscopy," Physical Review Letters, vol. 99, p. 197001, Nov 9 2007.*

[2] *F. Schmitt, et al., "Transient electronic structure and melting of a charge density wave in TbTe3," Science, vol. 321, pp. 1649-52, Sep 19 2008.*

[3] *M. Lisowski, et al., "Ultra-fast dynamics of electron thermalization, cooling and transport effects in Ru(001)," Applied Physics a-Materials Science & Processing, vol. 78, pp. 165-176, Jan 2004.*

[4] *L. Fu, "Hexagonal warping effects in the surface states of the topological insulator Bi2Te3," Physical Review Letters, vol. 103, p. 266801, Dec 31 2009.*

[5] *A. Damascelli, "Probing the electronic structure of complex systems by ARPES," Physica Scripta, vol. T109, pp. 61-74, 2004.*

[6] *S. Souma, et al., "Direct Measurement of the Out-of-Plane Spin Texture in the Dirac-Cone Surface State of a Topological Insulator," Physical Review Letters, vol. 106, May 25 2011.*

[7] *Y. L. Chen, et al., "Experimental realization of a three-dimensional topological insulator, Bi2Te3," Science, vol. 325, pp. 178-81, Jul 10 2009.*

[8] *D. J. Thouless, et al., "Quantized Hall Conductance in a Two-Dimensional Periodic Potential," Physical Review Letters, vol. 49, pp. 405-408, 1982.*

[9] *X. G. Wen, "Topological orders and edge excitations in fractional quantum Hall states," Advances in Physics, vol. 44, pp. 405-473, Sep-Oct 1995.*

[10] *K. Vonklitzing, et al., "New Method for High-Accuracy Determination of the Fine-Structure Constant Based on Quantized Hall Resistance," Physical Review Letters, vol. 45, pp. 494-497, 1980.*

[11] *M. V. Berry, "Quantal Phase-Factors Accompanying Adiabatic Changes," Proceedings of the Royal Society of London Series a-Mathematical Physical and Engineering Sciences, vol. 392, pp. 45-57, 1984.*

[12] *F. D. M. Haldane, "Model for a Quantum Hall-Effect without Landau-Levels - Condensed-Matter Realization of the Parity Anomaly," Physical Review Letters, vol. 61, pp. 2015-2018, Oct 31 1988.*

[13] *C. L. Kane and E. J. Mele, "Z(2) topological order and the quantum spin Hall effect," Physical Review Letters, vol. 95, Sep 30 2005.*

[14] *C. L. Kane and E. J. Mele, "Quantum spin Hall effect in graphene," Physical Review Letters, vol. 95, Nov 25 2005.*

[15] *L. Fu and C. L. Kane, "Topological insulators with inversion symmetry," Physical Review B, vol. 76, Jul 2007.*

[16] *L. Fu, et al., "Topological insulators in three dimensions," Physical Review Letters, vol. 98, Mar 9 2007.*

[17] *J. E. Moore and L. Balents, "Topological invariants of time-reversal-invariant band structures," Physical Review B, vol. 75, Mar 2007.*

[18] *B. A. Bernevig, et al., "Quantum spin Hall effect and topological phase transition in HgTe quantum wells," Science, vol. 314, pp. 1757-1761, Dec 15 2006.*

[19] *M. Konig, et al., "Quantum spin hall insulator state in HgTe quantum wells," Science, vol. 318, pp. 766-770, Nov 2 2007.*

[20] *S. Hufner, Photoelectron Spectroscopy. Berlin: Springer, 2003.*

[21] *D. Hsieh, et al., "A topological Dirac insulator in a quantum spin Hall phase," Nature, vol. 452, p. 5p, 2008.*

[22] *D. Hsieh, et al., "A tunable topological insulator in the spin helical Dirac transport regime," Nature, vol. 460, p. 5p, 2009.*

[23] *M. Z. Hasan and C. L. Kane, "Colloquium: Topological insulators," Reviews of Modern Physics, vol. 82, p. 23p, 2010.*

[24] *Y. L. Chen, et al., "Experimental Realization of a Three-Dimensional Topological Insulator, Bi2Te3," Science, vol. 325, pp. 178-181, Jul 10 2009.*

[25] *Y. Xia, et al., "Observation of a large-gap topological-insulator class with a single Dirac cone on the surface," Nature Physics, vol. 5, pp. 398-402, Jun 2009.*

[26] *D. Hsieh, et al., "Observation of Unconventional Quantum Spin Textures in Topological Insulators," Science, vol. 323, p. 4p, 2009.*

[27] *J. G. Fujimoto, et al., "Femtosecond Laser Interaction with Metallic Tungsten and Nonequilibrium Electron and Lattice Temperatures," Physical Review Letters, vol. 53, pp. 1837-1840, 1984.*

[28] *W. S. Fann, et al., "Electron Thermalization in Gold," Physical Review B, vol. 46, pp. 13592-13595, Nov 15 1992.*

[29] *W. S. Fann, et al., "Direct Measurement of Nonequilibrium Electron-Energy Distributions in Subpicosecond Laser-Heated Gold-Films," Physical Review Letters, vol. 68, pp. 2834-2837, May 4 1992.*

[30] *R. Haight, et al., "Novel System for Picosecond Photoemission Spectroscopy," Review of Scientific Instruments, vol. 59, pp. 1941-1946, Sep 1988.*

[31] *U. Hofer, et al., "Time-resolved coherent photoelectron spectroscopy of quantized electronic states on metal surfaces," Science, vol. 277, pp. 1480-1482, Sep 5 1997.*

[32] *H. Petek and S. Ogawa, "Femtosecond time-resolved two-photon photoemission studies of electron dynamics in metals," Progress in Surface Science, vol. 56, pp. 239-310, Dec 1997.*

[33] T. Fauster, et al., "Quasi-elastic scattering of electrons in image-potential states," Progress in Surface Science, vol. 82, pp. 224-243, 2007.

[34] J. D. Koralek, et al., "Experimental setup for low-energy laser-based angle resolved photoemission spectroscopy," Review of Scientific Instruments, vol. 78, May 2007.

[35] J. D. Koralek, et al., "Laser based angle-resolved photoemission, the sudden approximation, and quasiparticle-like spectral peaks in Bi2Sr2CaCu2O8+delta," Physical Review Letters, vol. 96, Jan 13 2006.

[36] F. Schmitt, et al., "Transient electronic structure and melting of a charge density wave in TbTe3," Science, vol. 321, pp. 1649-1652, Sep 19 2008.

[37] P. S. Kirchmann, et al., "A time-of-flight spectrometer for angle-resolved detection of low energy electrons in two dimensions," Applied Physics a-Materials Science & Processing, vol. 91, pp. 211-217, May 2008.

[38] L. Rettig, et al., "Ultrafast Momentum-Dependent Response of Electrons in Antiferromagnetic EuFe2As2 Driven by Optical Excitation," Physical Review Letters, vol. 108, Feb 27 2012.

[39] R. Cortes, et al., "Momentum-Resolved Ultrafast Electron Dynamics in Superconducting Bi2Sr2CaCu2O8+delta," Physical Review Letters, vol. 107, Aug 25 2011.

[40] M. Sultan, et al., "Electron- and phonon-mediated ultrafast magnetization dynamics of Gd(0001)," Physical Review B, vol. 85, May 8 2012.

[41] J. Graf, et al., "Nodal quasiparticle meltdown in ultrahigh-resolution pump-probe angle-resolved photoemission," Nature Physics, vol. 7, pp. 805-809, Oct 2011.

[42] C. L. Smallwood, et al., "Tracking Cooper Pairs in a Cuprate Superconductor by Ultrafast Angle-Resolved Photoemission," Science, vol. 336, pp. 1137-1139, Jun 1 2012.

[43] Y. Ishida, et al., "Non-thermal hot electrons ultrafastly generating hot optical phonons in graphite," Scientific Reports, vol. 1, Aug 19 2011.

[44] S. Xu, et al., "Energy dependence of electron lifetime in graphite observed with femtosecond photoemission spectroscopy," Physical Review Letters, vol. 76, pp. 483-486, Jan 15 1996.

[45] G. Moos, et al., "Anisotropy of quasiparticle lifetimes and the role of disorder in graphite from ultrafast time-resolved photoemission spectroscopy," Physical Review Letters, vol. 87, Dec 24 2001.

[46] R. Haight, "Electron Dynamics at Surfaces," Surface Science Reports, vol. 21, pp. 277-325, 1995.

[47] J. Gudde, et al., "Time-resolved investigation of coherently controlled electric currents at a metal surface," Science, vol. 318, pp. 1287-1291, Nov 23 2007.

[48] J. Stahler, et al., "Solvation dynamics of surface-trapped electrons at NH3 and D2O crystallites adsorbed on metals: from femtosecond to minute timescales," Chemical Science, vol. 2, pp. 907-916, 2011.

[49] J. Stahler, et al., "Dynamics of electron transfer at polar molecule-metal interfaces: the role of thermally activated tunnelling," New Journal of Physics, vol. 9, Oct 31 2007.

[50] J. Stahler, et al., "Impact of ice structure on ultrafast electron dynamics in D2O clusters on Cu(111)," Physical Review Letters, vol. 98, May 18 2007.

[51] S. Xu, et al., "Energy dependence of electron lifetime in graphite observed with femtosecond photoemission spectroscopy," Physical Review Letters, vol. 76, pp. 483-486, Jan 15 1996.

[52] P. B. Allen, "Theory of Thermal Relaxation of Electrons in Metals," Physical Review Letters, vol. 59, pp. 1460-1463, Sep 28 1987.

[53] L. Perfetti, et al., "Time evolution of the electronic structure of 1T-TaS2 through the insulator-metal transition," Physical Review Letters, vol. 97, Aug 11 2006.

[54] M. Forst, et al., "Driving magnetic order in a manganite by ultrafast lattice excitation," Physical Review B, vol. 84, Dec 2 2011.

[55] M. Forst, et al., "Nonlinear phononics as an ultrafast route to lattice control," Nature Physics, vol. 7, pp. 854-856, Nov 2011.

[56] A. Dienst, et al., "Bi-directional ultrafast electric-field gating of interlayer charge transport in a cuprate superconductor," Nature Photonics, vol. 5, pp. 485-488, Aug 2011.

[57] D. Fausti, et al., "Light-Induced Superconductivity in a Stripe-Ordered Cuprate," Science, vol. 331, pp. 189-191, Jan 14 2011.

[58] N. H. Lindner, et al., "Floquet topological insulator in semiconductor quantum wells," Nature Physics, vol. 7, pp. 490-495, Jun 2011.

[59] T. Kitagawa, et al., "Exploring topological phases with quantum walks," Physical Review A, vol. 82, Sep 24 2010.

[60] J. Inoue and A. Tanaka, "Photoinduced Transition between Conventional and Topological Insulators in Two-Dimensional Electronic Systems," Physical Review Letters, vol. 105, Jun 28 2010.

[61] S. Raghu, et al., "Collective Modes of a Helical Liquid," Physical Review Letters, vol. 104, Mar 19 2010.

[62] H. Z. Lu, et al., "Massive Dirac fermions and spin physics in an ultrathin film of topological insulator," Physical Review B, vol. 81, Mar 2010.

[63] P. Hosur, "Circular photogalvanic effect on topological insulator surfaces: Berry-curvature-dependent response," Physical Review B, vol. 83, Jan 18 2011.

[64] J. W. McIver, et al., "Control over topological insulator photocurrents with light polarization," Nat Nanotechnol, vol. 7, pp. 96-100, Feb 2012.

[65] Y. H. Wang, et al., "Observation of a warped helical spin texture in Bi2Se3 from circular dichroism angle-resolved photoemission spectroscopy," Physical Review Letters, vol. 107, p. 207602, Nov 11 2011.

[66] *S. R. Park, et al., "Chiral Orbital-Angular Momentum in the Surface States of Bi2Se3," Physical Review Letters, vol. 108, Jan 25 2012.*

[67] *S. R. Park, et al., "Orbital-Angular-Momentum Based Origin of Rashba-Type Surface Band Splitting," Physical Review Letters, vol. 107, Oct 6 2011.*

[68] *J. S.-B. M. R. Scholz, D. Marchenko, A. Varykhalov, A. Volykhov, L. V. Yashina, O. Rader, "High spin polarization and circular dichroism of topological surface states on Bi2Te3," 2011.*

[69] *Y. Ishida, et al., "Common Origin of the Circular-Dichroism Pattern in Angle-Resolved Photoemission Spectroscopy of SrTiO3 and CuxBi2Se3," Physical Review Letters, vol. 107, Aug 9 2011.*

[70] *P. D. C. K. M. S. Bahramy, A. de la Torre, J. Chang, M. Shi, L. Patthey, G. Balakrishnan, Ph. Hofmann, R. Arita, N. Nagaosa, F. Baumberger, "Emergent quantum confinement at topological insulator surfaces," 2012.*

[71] *G. Bian, et al., "Illuminating the Surface Spin Texture of the Giant-Rashba Quantum-Well System Bi/Ag(111) by Circularly Polarized Photoemission," Physical Review Letters, vol. 108, May 2 2012.*

[72] *H. Mirhosseini and J. Henk, "Spin texture and circular dichroism in photoelectron spectroscopy from the topological insulator bi_{2}te_{3}: first-principles photoemission calculations," Physical Review Letters, vol. 109, p. 036803, Jul 20 2012.*

[73] *J. Henk, et al., "Complex Spin Texture in the Pure and Mn-Doped Topological Insulator Bi2Te3," Physical Review Letters, vol. 108, May 14 2012.*

[74] *K. Kuroda, et al., "Hexagonally deformed Fermi surface of the 3D topological insulator Bi2Se3," Physical Review Letters, vol. 105, p. 076802, Aug 13 2010.*

[75] *X. L. Qi and S. C. Zhang, "The quantum spin Hall effect and topological insulators," Physics Today, vol. 63, pp. 33-38, Jan 2010.*

[76] *J. E. Moore, "The birth of topological insulators," Nature, vol. 464, pp. 194-198, Mar 11 2010.*

[77] *H. Steinberg, et al., "Surface State Transport and Ambipolar Electric Field Effect in Bi2Se3 Nanodevices," Nano Letters, vol. 10, pp. 5032-5036, Dec 2010.*

[78] *J. G. Checkelsky, et al., "Bulk Band Gap and Surface State Conduction Observed in Voltage-Tuned Crystals of the Topological Insulator Bi2Se3," Physical Review Letters, vol. 106, May 10 2011.*

[79] *D. S. Kong, et al., "Ambipolar field effect in the ternary topological insulator (BixSb1-x)(2)Te-3 by composition tuning," Nature Nanotechnology, vol. 6, pp. 705-709, Nov 2011.*

[80] *F. X. Xiu, et al., "Manipulating surface states in topological insulator nanoribbons," Nature Nanotechnology, vol. 6, pp. 216-221, Apr 2011.*

[81] *L. Fu and C. L. Kane, "Superconducting proximity effect and Majorana fermions at the surface of a topological insulator," Physical Review Letters, vol. 100, Mar 7 2008.*

[82] L. A. Jiang, et al., "Interface between Topological and Superconducting Qubits," Physical Review Letters, vol. 106, Mar 28 2011.

[83] A. H. C. Neto, Reviews of Modern Physics, vol. 81, 2009.

[84] F. Bonaccorso, et al., "Graphene photonics and optoelectronics," Nature Photonics, vol. 4, pp. 611-622, Sep 2010.

[85] J. N. Hancock, et al., "Surface State Charge Dynamics of a High-Mobility Three-Dimensional Topological Insulator (vol 107, 136803, 2011)," Physical Review Letters, vol. 107, Sep 30 2011.

[86] R. V. Aguilar, et al., "Terahertz Response and Colossal Kerr Rotation from the Surface States of the Topological Insulator Bi2Se3," Physical Review Letters, vol. 108, Feb 22 2012.

[87] D. Hsieh, et al., "Nonlinear optical probe of tunable surface electrons on a topological insulator," Physical Review Letters, vol. 106, p. 057401, Feb 4 2011.

[88] N. Kumar, et al., "Spatially resolved femtosecond pump-probe study of topological insulator Bi2Se3," Physical Review B, vol. 83, Jun 6 2011.

[89] J. A. Sobota, et al., "Ultrafast optical excitation of a persistent surface-state population in the topological insulator Bi2Se3," Physical Review Letters, vol. 108, p. 117403, Mar 16 2012.

[90] M. Hajlaoui, et al., "Ultrafast surface carrier dynamics in the topological insulator bi(2)te(3)," Nano Lett, vol. 12, pp. 3532-6, Jul 11 2012.

[91] K. Boger, et al., "Linewidths in energy-resolved two-photon photoemission spectroscopy," Physical Review B, vol. 65, Feb 15 2002.

[92] C. Reuss, et al., "Control of the dephasing of image-potential states by CO adsorption on Cu(100)," Physical Review Letters, vol. 82, pp. 153-156, Jan 4 1999.

[93] C. Kittel, Introduction to solid state physics, 7th ed. New York: Wiley, 1996.

[94] G. E. Shoemake, et al., "Specific Heat of N- and P-Type Bi2te3 from 1.4 to 90 Degrees K," Physical Review, vol. 185, pp. 1046-&, 1969.

[95] G. Grimvall, The electron-phonon interaction in metals. Amsterdam ; New York: North-Holland Pub. Co. : sole distributors for the U.S.A. and Canada, Elsevier North-Holland, 1981.

[96] P. T. Landsberg, Recombination in semiconductors. Cambridge ; New York: Cambridge University Press, 1991.

[97] R. Bistritzer and A. H. MacDonald, "Electronic cooling in graphene," Physical Review Letters, vol. 102, p. 206410, May 22 2009.

[98] P. D. C. King, et al., "Large Tunable Rashba Spin Splitting of a Two-Dimensional Electron Gas in Bi2Se3," Physical Review Letters, vol. 107, Aug 25 2011.

[99] S. R. Park, et al., "Quasiparticle scattering and the protected nature of the topological states in a parent topological insulator Bi2Se3," Physical Review B, vol. 81, Jan 2010.

[100] D. Hsieh, et al., "Observation of Time-Reversal-Protected Single-Dirac-Cone Topological-Insulator States in Bi2Te3 and Sb2Te3," Physical Review Letters, vol. 103, Oct 2 2009.

[101] Z. H. Zhu, et al., "Rashba Spin-Splitting Control at the Surface of the Topological Insulator Bi2Se3," Physical Review Letters, vol. 107, Oct 27 2011.

[102] M. Bianchi, et al., "Coexistence of the topological state and a two-dimensional electron gas on the surface of Bi2Se3," Nature Communications, vol. 1, Nov 2010.

[103] L. Huang, et al., "Ultrafast transient absorption microscopy studies of carrier dynamics in epitaxial graphene," Nano Lett, vol. 10, pp. 1308-13, Apr 14 2010.

[104] H. N. Wang, et al., "Ultrafast relaxation dynamics of hot optical phonons in graphene," Applied Physics Letters, vol. 96, Feb 22 2010.

[105] T. Kampfrath, et al., "Strongly coupled optical phonons in the ultrafast dynamics of the electronic energy and current relaxation in graphite," Physical Review Letters, vol. 95, Oct 28 2005.

[106] H. Beidenkopf, et al., "Spatial fluctuations of helical Dirac fermions on the surface of topological insulators," Nature Physics, vol. 7, pp. 939-943, Dec 2011.

[107] J. Seo, et al., "Transmission of topological surface states through surface barriers," Nature, vol. 466, pp. 343-346, Jul 15 2010.

[108] N. M. Gabor, et al., "Hot Carrier-Assisted Intrinsic Photoresponse in Graphene," Science, vol. 334, pp. 648-652, Nov 4 2011.